Fakultät für Medizin

Volumetric Optoacoustic & Ultrasound Tomography for Imaging of Multi-Scale Dynamics

Thomas Felix Fehm

Vollständiger Abdruck der von der Fakultät für Medizin der Technischen Universität München zur Erlangung des akademischen Grades eines Doktors der Naturwissenschaften (Dr. rer. nat.) genehmigten Dissertation

Vorsitzende: Prof. Dr. Gabriele Multhoff

Prüfer der Dissertation:

1. Prof. Dr. Daniel Razansky
2. Prof. Dr. Andreas Bausch
3. Prof. Dr. Eberhard Riedle

Die Dissertation wurde am 2. Juni 2016 bei der Technischen Universität München eingereicht und durch die Fakultät für Medizin am 17. Mai 2017 angenommen.

"If I have seen further, it is by standing on the shoulders of giants."

— Sir Isaac Newton (1643 – 1727), Physicist and Mathematician

Abstract

Optoacoustic (photoacoustic) imaging has been growingly utilized in biological research in the last decade and it is now being translated into the clinical routine with a large number of applications envisioned. Optoacoustics is characterized by its operational simplicity, its comparatively low hardware complexity and its ability to deliver volumetric real-time images of optical contrast at high spatio-temporal resolution. This unique combination of features poises optoacoustics to open new possibilities to study multi-scale processes in model organisms as well as to improve clinical diagnosis. Efforts have been directed towards improving the performance of optoacoustic imaging systems regarding sensitivity, specificity as well as spatial and temporal resolution. However, even though multiple imaging configurations were introduced previously, their applicability in real biological or medical imaging scenarios remain limited due to the lack of essential system features such as hand-held operationability or volumetric in-vivo imaging capacity. In the first part of this thesis, two novel volumetric imaging systems are developed that overcome these limitations and their imaging performance is characterized through multiple phantom and in-vivo experiments. First, a hybrid ultrasound and optoacoustic imaging platform with volumetric real-time imaging capacity that can be used as a hand-held probe is described. The proposed method is based on passive element optical excitation and therefore avoids the hardware complexity of active ultrasound generation. With the method proposed, complete hybrid datasets can be generated with a single laser pulse, thus allowing to simultaneously render ultrasound and optoacoustic images at a rate that is only limited by the pulse repetition frequency of the laser. In addition, a novel whole-body small animal optoacoustic scanner is introduced. The newly developed scanner utilizes a spherically focused matrix transducer array to deliver whole-body anatomical images of small-animals in-vivo of unparalleled quality with the additional capacity to deliver volumetric real-time data of specific regions. The imaging performance of the proposed approach is demonstrated through multiple tissue mimicking phantom and in-vivo experiments. The introduced system is perfectly suited for volumetric imaging across multiple spatial and temporal scales, thus enabling simultaneous anatomical, functional and molecular imaging at an unprecedented quality. In the second part of this thesis, the developed volumetric ultrasound and optoacoustic tomography systems are applied in various imaging scenarios. A first set of experiments is dedicated to validate the clinical applicability of the developed hybrid ultrasound and optoacoustic imaging system by characterizing a newly synthesized dual-modality contrast agent through phantom and in-vivo experiments. In a second set of experiments, the developed system is utilized to position a laser catheter and subsequently monitor lesion progression in an ex-vivo endovenous laser treatment study. Furthermore, the imaging configuration is applied to resolve and characterize hemodynamic changes in mouse brains induced through changes in breathing gas or epileptic stimulation respectively. Ultimately, the newly developed small animal scanner is utilized in multiple in-vivo studies including cardiac imaging, characterization of contrast agent kinetics as well as tumor and organ perfusion studies.

Contents

I Publication List

⋆ Equal contribution.

Deán-Ben, X.L.⋆, **Fehm, T.F.**⋆, Ford, S.J., Gottschalk, S. and Razansky, D., 2017. Spiral volumetric optoacoustic tomography visualizes multi-scale dynamics in mice. *Light: Science & Application*. Accepted.

Fehm, T.F., Deán-Ben, X.L., Ford, S.J., D., 2016. In vivo whole-body optoacoustic scanner with real-time volumetric imaging capacity. *Optica.*, 3(11), pp.1153-1159

Gottschalk, S.⋆, **Fehm, T.F.**⋆, Deán-Ben, X.L., Tsytsarev, V. and Razansky, D., 2017. Correlation between volumetric oxygenation responses and electrophysiology identifies deep thalamocortical activity during epileptic seizures. *Neurophotonics*, 4(1), pp.011007-011007.

Ford, S.J., **Fehm, T.F.**, Deán-Ben, X.L. and Razansky, D., 2016. Mouse cardiac function estimated on a beat-by-beat basis from time-resolved volumetric optoacoustic imaging. *Biomedical Optics Express. In Review.*

Deán-Ben, X.L., **Fehm, T.F.**, Gostic, M. and Razansky, D., 2015. Volumetric hand-held optoacoustic angiography as a tool for real-time screening of dense breast. *Journal of Biophotonics.*

Gottschalk, S., **Fehm, T.F.**, Deán-Ben, X.L. and Razansky, D., 2015. Noninvasive real-time visualization of multiple cerebral hemodynamic parameters in whole mouse brains using five-dimensional optoacoustic tomography. *Journal of Cerebral Blood Flow & Metabolism.*, 35(4), pp.531-535.

Kirscher, L., Deán-Ben, X.L., Scadeng, M., Zaremba, A., Zhang, Q., Kober, C., **Fehm, T.F.**, Razansky, D., Ntziachristos, V., Stritzker, J. and Szalay, A.A., 2015. Doxycycline inducible melanogenic vaccinia virus as theranostic anti-cancer agent. *Theranostics*, 5(10), p.1045.

Fehm, T.F., Deán-Ben, X.L., Schaur, P., Sroka, R. and Razansky, D., 2015. Volumetric optoacoustic imaging feedback during endovenous laser therapy-an ex vivo investigation. *Journal of Biophotonics.*

Deán-Ben, X., **Fehm, T.F.** and Razansky, D., 2014. Universal hand-held three-dimensional optoacoustic imaging probe for deep tissue human angiography and functional preclinical studies in real time. *JoVE (Journal of Visualized Experiments)*, (93), pp.e51864-e51864.

Fehm, T.F., Deán-Ben, X.L. and Razansky, D., 2014. Four dimensional hybrid ultrasound and optoacoustic imaging via passive element optical excitation in a hand-held probe. *Applied Physics Letters*, 105(17), p.173505.

Conference Abstracts

Fehm, T.F., Deán-Ben, X.L., Schaur, P., Sroka, R. and Razansky, D., 2016, March. Volumetric optoacoustic monitoring of endovenous laser treatments. In SPIE BiOS (pp. 97080F-97080F). International Society for Optics and Photonics.

Deán-Ben, X.L., **Fehm, T.F.**, Gottschalk, S., Bay, E. and Razansky, D., 2015. Light excitation methods for five dimensional optoacoustic imaging. In European Conferences on Biomedical Optics (pp. 95391A-95391A). International Society for Optics and Photonics.

Gottschalk, S., **Fehm, T.F.**, Dean-Ben, X.L. and Razansky, D., 2015, April. Five-dimensional optoacoustic tomography for real-time whole brain neuroimaging of stimulus-evoked responses. In Neural Engineering (NER), 7th International IEEE/EMBS Conference on (pp. 873-875). IEEE.

Deán-Ben, X.L., Gottschalk, S., **Fehm, T.F.** and Razansky, D., 2015, March. Optoacoustic imaging in five dimensions. In SPIE BiOS (pp. 93231M-93231M). International Society for Optics and Photonics.

Fehm, T.F., Deán-Ben, X.L. and Razansky, D., 2015, March. Hybrid optoacoustic and ultrasound imaging in three dimensions and real time by optical excitation of a passive element. In SPIE BiOS (pp. 93232X-93232X). International Society for Optics and Photonics.

II Introduction

This thesis is organized in five chapters. The first chapter summarizes all publications that the candidate (co-)authored during his doctoral studies. The second chapter commences with an introduction to the field of optoacoustic (OA)[1] imaging and its practical implementations. The chapter continues with a motivation of the conducted research followed by a description of the thesis objectives in Section II.2. Eventually, the essential mathematics for OA imaging will be presented, i.e. , a derivation of the OA equation, a discussion of common image reconstruction techniques and an introduction to the concept of linear unmixing will be given. Chapter III and Chapter IV are then both dedicated to a detailed presentation of the conducted research. The thesis will conclude in Chapter V with a summary of the presented work as well as an outlook towards its expected impact. It shall be noted that the presentation of the conducted research as well as the data and the results in Chapter III and Chapter IV are not original and were published or submitted to peer-reviewed journals prior to the submission of this thesis.

II.1 Introduction to Optoacoustic Imaging

II.1.1 Historical Development

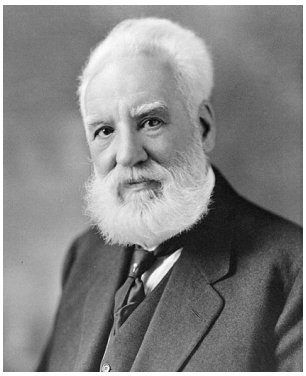

Figure II.1: Alexander Graham Bell (1847–1922).

The story of a great scientific discovery often begins with a random observation and so does the story of OA imaging when the Scottish-born scientist, Alexander Graham Bell (Figure II.1), investigated ways to refine his most prominently known invention: the telephone. In 1880, Bell experimented with Selenium to transmit electric signals wirelessly and over greater distances, having nothing else in mind but the first cell phone. By that time, it was already known that the conductivity of Selenium can be modulated by changing its light intensity exposure. Bell intended to utilize this effect to transmit electric signals wirelessly by variation of the sunlight exposure of transparent cylinders filled with Selenium and wired to a speaker - an invention that he termed *photophone*. However, when he tried to focus sunlight onto the Selenium cylinders using mirrors, Bell noticed that these mirrors themselves created an acoustic signal when the intensity of sunlight was modulated through a rotating slotted wheel. After he had further investigated this phenomenon, Bell realized that the acoustic

1 Optoacoustic and photoacoustic are being used synonymously in the literature.

signal depended on the type of material and he correctly concluded that the atoms in the mirrors had converted the absorbed light energy into heat which was then further converted to a local pressure field via thermoelastic expansion. The *optoacoustic effect*, that is the conversion of light into sound waves, was discovered [1].

The OA effect is the foundation of the rapidly evolving field of OA imaging. First applications of this effect were proposed early after its discovery in 1880. First Bell and later Tyndall and Röntgen demonstrated that solids, liquids and gases can be identified spectrally using ultraviolet and infrared light [2–4] and in 1938, Veingerov used the OA effect to determine carbon dioxide concentrations [5]. [6–9]. However, since the acoustic detection technology of that time was lagging sensitivity and scalability, the technique was abandoned until the second half of the 20^{th} century. The demand for sensitive and scalable acoustic transducers for submarine detection during the World War I and II as well as the idea to use ultrasound as a medical imaging modality in 1942 by Dussik, [10] pushed acoustic detection technology to new boundaries. With the invention of the laser by Theodore H. Maiman, a physicist at Hughes Research Laboratories in Malibu, California in 1960 [11], a focusable and modulatable light source was available and the OA effect finally received broad attention again with the application of OA spectroscopy in analytical chemistry in the 1970s [7]. Shortly after, Bowen suggested OA soft tissue imaging [12] in 1981 and the development of OA imaging further accelerated when Kruger et al. [13] presented the first OA image of a phantom (Figure II.2) followed by the first in-vivo image delivered by Oraevsky [14] in 1999. With the rapid development of fast-tunable lasers, OA finally had become a mature imaging modality and received broad attention with the first functional OA image presented by Wang et al. where multi-spectral light was exploited to resolve cerebral hemodynamic changes in cortical blood vessels [15]. For further reading on the historical development of OA imaging, the reader is referred to early reviews, books and conference proceedings [16–19].

II.1.2 The Principle of Optoacoustic Imaging

Usually, OA imaging utilizes short laser pulses in the visible or near-infrared to excite OA signals where pulse lengths are typically in the nanosecond region. However, it was shown that intensity modulated light sources may also be utilized to excite OA signals [20]. For biological applications, a wavelength between 650 and 1350 nm is usually chosen. This range is known as the near-infrared window where light has its maximal depth of penetration in tissue [21, 22]. A plot of the electromagnetic absorption coefficient of water is shown in Figure II.3a. The ultra-short electromagnetic energy pulse is absorbed locally by the specimen and results in a spatially localized temperature rise ΔT. The heated volume element now expands and converts the absorbed energy into a localized initial pressure rise p_0 via thermoelastic expansion [23]:

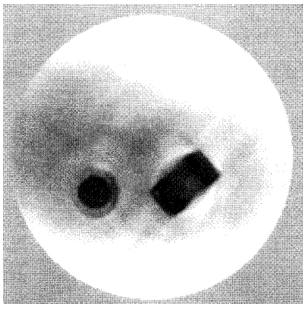

Figure II.2: First OA image of a phantom. Two highly-absorbing objects (black) were embedded in an agar cylinder [13].

$$p_0 = \frac{\beta}{\kappa}\Delta T \tag{1.1}$$

where κ is the isothermal compressibility and β is the thermal expansion coefficient. This effect was described earlier in Subsection II.1.1 and is known as the OA effect. Equation 1.1 states that the resulting spatially varying pressure map is proportional to the initial local energy absorption of the specimen. Typical values in water and soft tissue are $\kappa = 5 \cdot 10^{-10}\,\text{Pa}^{-1}$ and

$\beta = 4 \cdot 10^{-4}\,\mathrm{K}^{-1}$ so that a temperature change of about 1mK translates into a pressure rise of 800 Pa [23] which is well above the noise level of a modern ultrasonic transducer [23]. In practice, a sufficient signal-to-noise ratio can almost always be achieved without causing damage to living cells. Once OA signals had been excited, an image of the initial pressure distribution can be reconstructed by simultaneous detection of the emitted signals around the sample where the spatial resolution depends on the detected ultrasonic bandwidth of the transducers. For instance, to achieve a resolution of about 1 mm, the detected OA signals must have a bandwidth of about 1 MHz assuming the typical speed of sound in water of 1500 m/s [24]. The image contrast in OA imaging is defined by several factors which will be derived mathematically in Subsection II.3.1. As it shall be seen later, the initial pressure rise in equation 1.1 can be rewritten in terms of three factors [25]:

$$p_0 = \mu_a \, \Gamma \, \partial_t \Phi \tag{1.2}$$

where μ_a is the local absorption coefficient, Γ is the Grüneisen parameter, which in general is temperature dependent, and the local light fluence rate Φ. As a consequence, p_0 is not only affected by local variations with respect to the absorption coefficient but also with respect to the light fluence. Correcting for this effect is extremely challenging, even if a-priori knowledge about the absorption properties of the tissue exist (which almost never does in practice). A simple but effective strategy assumes a diffuse propagation regime of the excitation light inside the tissue. The photon density is then given by a decaying exponential [26]. The development of strategies to correct for this effect are indispensable for quantitative OA imaging and computationally feasible approaches are yet to be discovered. Until then, deep tissue quantitative OA imaging remains to be unachievable. Furthermore, the temperature dependence of Γ is usually neglected and it is argued that the imaging contrast in OA imaging is mainly optical.

A major advantage of optical imaging modalities lies in the possibility to exploit the characteristic absorption spectrum of different chromophores (Figure II.3b). By the use of multi-wavelengths optical excitation through fast-tuning optical parametric oscillator based lasers, Multispectral (MS) OA signals can be excited on a millisecond scale and can then be used to further extract functional and molecular information from the sample in real time [27, 28]. Additionally, the diffraction limit of optical and near-infrared light is small and in principle imaging can be performed at very high resolution. However, optical scattering in tissue is strong and spatial resolution degrades significantly in depth since the propagation regime of the photons effectively equals a random walk after a few hundreds of microns [29, 30]. Usually, optical imaging modalities are categorized by the propagation regime inside the imaged tissue [29]. When imaging depth is shallow, photons undergo only few scattering events and their propagation path therefore is ballistic [29] thus allowing for high spatial resolution imaging. Confocal light microscopy and 2-photon microscopy fall into this category. If imaging is to be performed deep inside the tissue, the propagation regime of incident photons becomes diffusive and spatial resolution severely deteriorates with depth [29]. Diffuse optical tomography is a prominent example for that category. Imaging is possible up to centimeters inside the tissue but at very limited spatial resolution [23, 29]. Depending on the tissue and wavelengths employed, the transition of the propagation regime occurs around 0.5 mm [29, 30]. OA imaging however can deliver optical contrast of up to multiple centimeters in depth at ultrasonic resolution [31]. The incident photons are converted into acoustic waves and acoustic scattering is at least two orders of magnitude weaker than optical scattering in biological tissue [32]. Even though the influence of acoustic scattering and attenuation on image quality is less critical in OA, it may become crucial when very high frequencies or deeply seated structures are imaged [33].

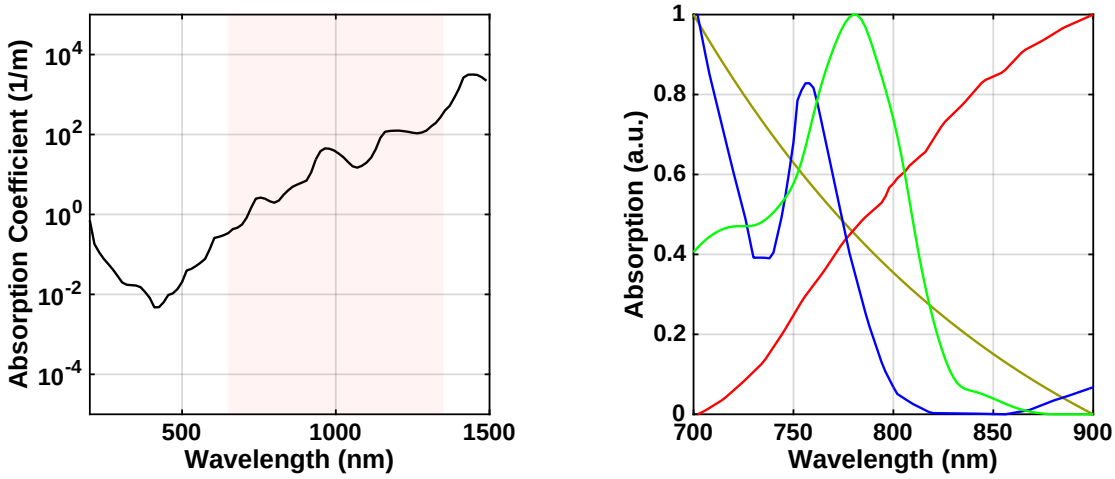

a Absorption spectrum of water.

b Absorption spectra of various substances.

Figure II.3: Absorption spectra of various substances. Figure II.3a shows the absorption spectrum of water. The range between 650 and 1350 nanometer is known as the near-infrared window. In Figure II.3b, the characteristic absorption spectrum of oxygenated (red) and deoxygenated (blue) hemoglobin, melanin (yellow) and Indocyanine green (ICG) (green) is plotted.

For further material on the physical fundamentals of OA imaging the reader is referred to reviews and books [23, 25, 27, 31, 34–38].

II.1.3 Optoacoustic Imaging: Implementation & Application

Over the past decade, many different imaging designs and concepts to perform OA imaging have been proposed. All together, these implementations cover a large imaging length scale ranging from hundreds of nanometers to tens of centimeters while keeping up excellent spatial and temporal resolution. This unique multiscale imaging capacity makes OA imaging applicable to a wide domain of biological structures ranging from cells in basic science to whole organs in clinical research and diagnosis [23, 38]. Based on the resolution achieved and the intended field of application, three basic imaging configurations may be discriminated [23]:

- Optoacoustic Microscopy (OM)
- Optoacoustic Endoscopy (OE)
- Optoacoustic Tomography (OT)

The following paragraphs are dedicated to give an overview about OM, OE and OT imaging. In particular, the basic implementation of each imaging configuration as well as some application highlights will be presented. The following presentation follows a review of Wang and Hu [23] and the reader is encourage to consult this publication for further information on the matter. However, it shall be noted that the distinction between the three categories is not sharp and the transition between them is smooth.

II.1.3.1 Optoacoustic Microscopy

OM and OE are OA imaging configurations that are often based on single transducer detection and they are usually utilized to image small structures, typically in the range of tens of microns

[23]. In OM, a high frequency transducer is aligned confocally with the illumination spot of a laser beam and for every laser pulse, a one-dimensional depth-resolved image is acquired [23]. By raster-scanning the focus of the transducer or the focus of the laser beam in two dimensions, a three-dimensional image can be reconstructed [23, 36, 39, 40]. Implementations using this imaging concept may be further categorized into optical-resolution or acoustic-resolution OM depending on whether the optical or the ultrasonic focus is finer [23]. Microscopes operating in the optical-resolution mode are typically used to image superficial tissue structures with high resolution whereas the acoustic-resolution mode is used to image deeper structures at the cost of spatial resolution [36, 41]. In optical-resolution OM, the laser beam is highly focused using a microscope objective and raster-scanned across the imaging plane while OA signals are detected through an unfocused transducer [23]. Using this technique, a lateral resolution as small as 5 μm with an axial resolution of 10 μm at a penetration depth of up to 0.2 mm was reported [42]. However, in acoustic-resolution microscopy a highly focused transducer is raster-scanned, while the sample is broadly illuminated with reported lateral and axial resolutions of about 45 μm and 15 μm respectively at a penetration depths of 3 mm [43]. OM has been intensively applied to a wide range of topics in biological and medical research such as vascular biology [44, 45], oncology [40, 46, 47], neurology [48–50] and cardiology [51–53]. For further reading on OM and its application, the reader is referred to recent reviews of the field [54–56].

II.1.3.2 Optoacoustic Endoscopy

OE recently emerged as a novel approach to deliver high resolution images of organs endoscopically [57–60]. The beam of a high-repetition laser source is guided into the imaged structure using a fiber bundle tube. Besides the light fibers, the tube also contains a needle detector and a rotateable acoustic and optical mirror at the outlet of the tube, essentially allowing for circumferential cross-sectional imaging [23]. The mirror distributes the light across the imaging cross-section and subsequently guides the excited acoustic waves to the needle transducer [59]. Compared to optical endoscopy, OE was proven to deliver an imaging depth of up to 7 mm which is far beyond the optical diffusion limit [58]. OE has been successfully used in pre-clinical applications such as imaging of macrophages in atherosclerotic plaques [57], imaging of the gastrointestinal tract and the esophagus of rodents [59] as well as monitoring melanoma tumor growth in rats in vivo [61]. Recent developments such as hybrid ultrasonic and OA endoscopic imaging [62], three-dimensional endoscopic OA imaging [63] as well as continued miniaturization of the technology, essentially allowing the OE probe to be inserted in a conventional endoscope [64], further accelerate the transition of OE into the clinic.

II.1.3.3 Optoacoustic Tomography

The third category of OA imaging configurations is referred to as Optoacoustic Tomography and it is most relevant for the scope of this thesis. In contrast to OM and OE imaging, in OT imaging OA signals are excited over a larger volume using an expanded laser beam and are subsequently detected tomographically at multiple positions around the imaged sample [23]. The characteristic length scale in OT imaging typically ranges from hundreds of microns to several centimeters. Throughout this thesis, it shall further be discriminated between OT imaging configurations that require the sample to be stationary fixed at a dedicated position while the scan is performed and systems that are compact in the sense that may be used as a hand-held probe. Early generations of OT systems used a single transducer, where either the detector or the sample was rotated and translated through motorized stages [13, 15, 65]. These systems

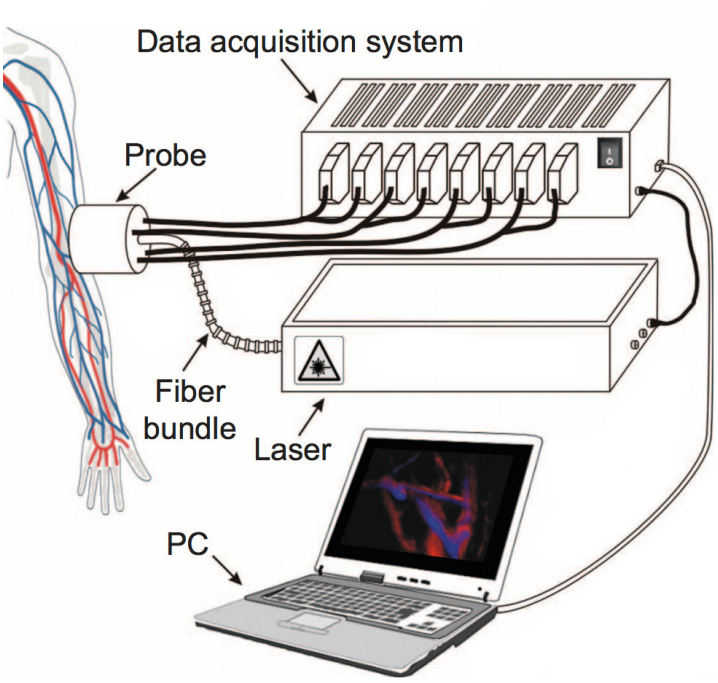

Figure II.4: Typical OT imaging setup. OA signals are excited multispectrally and are subsequently detected by the OA imaging probe. A data acquisition system records the data before GPU-based real-time image reconstruction is performed. Image from [28].

required the sample to be stationary fixed at a dedicated position and acquisition times were long. However, the massive development in acoustic detector technology and design now allows for compactly arranging hundreds of transducers on a one- or two dimensional geometrical shape such as a line [53, 66, 67], an arc length [27, 68, 69], a cylinder or a sphere [66, 70, 71]. These new generation OT systems use matrix arrays to acquire hundreds of signals simultaneously per position and the reduced acquisition time now allows for whole-body imaging of small animals such as mice and zebra fish at high resolution. Continuous miniaturization of the technology further allowed for probe designs with enough detectors so that the simultaneously detected OA signals from a single laser shot are sufficient to reconstruct an image, essentially allowing for real-time imaging. Combined with the rapid development of ultra-fast Graphical Processing Unit (GPU) and the availability of parallelizable reconstruction algorithms [72], it is even possible to visualize and interpret the acquired OA data in real time [73].

Over the past decade, numerous probe designs and implementations optimized for different applications were developed. Among them, two- and three dimensional multispectral real-time hand-held imaging probes [28, 38, 74–80], hybrid Ultrasound (US) and OA imaging probes [81–83], hybrid optical diffusion and OA imaging probes [84] as well as stationary imaging systems that employ transducer arrays to enable cross-sectional [27, 69, 85] and volumetric small animal whole-body imaging [86, 87]. Due to its superior imaging contrast, its high spatial and temporal resolution, its real-time capacity, its high portability and its spectral specificity, OT has received wide recognition in the science community and has been utilized to make substantial contributions in many fields of research such as cancer imaging [88–91], cardiovascular diseases [92, 93], functional neuroimaging [94–96], lymph node staging [97, 98] and imaging of arthritis and inflammation [99, 100].

In theory, the resolution of such devices only depends on the bandwidth of each transducer

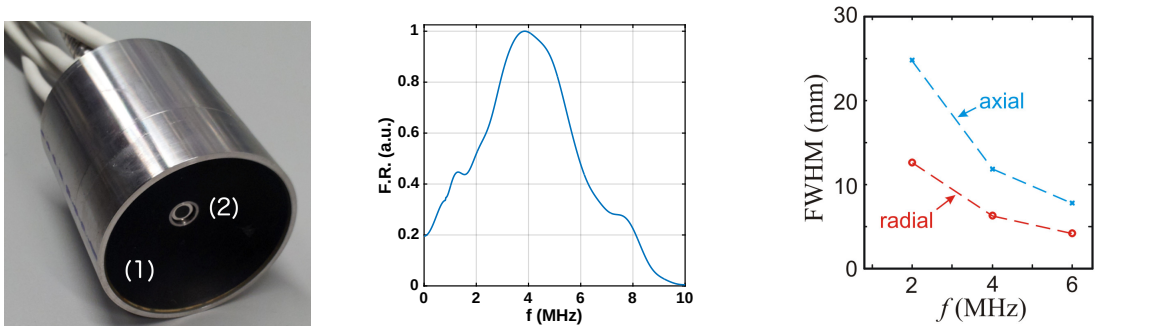

a Image of the SMTA.

b Frequency response of the SMTA.

c Imaging volume of the SMTA.

Figure II.5: Depiction and characterization of the SMTA. Figure II.5a. shows an image of the SMTA with the active surface formed by the transducers (1) and the outlet of the laser fiber (2). The radius of the array is 4 cm. The frequency response is plotted in Figure II.5b. Figure II.5c shows the effective size of the imaging region as a function of frequency.

built into the array, the number of detectors in the array and their geometrical arrangement. In practice, however, the resolution may be compromised by the detection surface of the individual transducer. Ideally, the transducer surface is point-like, but in order to maintain sufficient signal-to-noise ratio, a certain detection surface is unavoidable. The detection surface therefore must scale inversely with the central frequency of the transducer. This issue will be discussed in more detail in Subsection II.3.3. Recently, Dean-Ben et al. introduced a Spherical Matrix Transducer Array (SMTA) with 256 elements [70]. For a spherical arrangement of transducers, the influence of the detection surface is less critical. Compared to a linear probe, the field of view is smaller but the three dimensional alignment of the transducer elements allows for accurate three-dimensional imaging i.e. Volumetric Optoacoustic Tomography (VOT). However, the transducer has a central frequency of 4 MHz and $> 80\%$ detection bandwidth and every transducer has a surface of approximately $3 \times 3\,\mathrm{mm}^2$. The detection elements are distributed on a spherical surface with a radius of 4 cm and an angular coverage of 90°. It was further shown, that with the detection bandwidth of the probe, a nearly isotropic spatial resolution in the range of 200 μm can be achieved [70] (see Figure II.5). Figure II.5c shows a plot that characterizes the size of the imaging volume based on highest frequency that can be accurately reconstructed in this region. The SMTA perfectly show-cases the opportunities of modern OA imaging probes combined with multispectral fast-tuning lasers with Pulse Repetition Frequency (PRF) of up to 100 Hz and high-performance data acquisition hardware to deliver anatomical, functional and molecular volumetric images [28]. Its compact design of only 4 cm radius as well as its light weight make it applicable as stationary OT imaging system e.g. to image brain perfusion [28] but also as a hand-held imaging probe to examine human vasculature in real time [73].

II.1.4 Multispectral Optoacoustic Imaging

Throughout the following section, the concept of MS OA imaging will be introduced and it will be shown how functional parameters such the determination of blood oxygen saturation can be extracted from the recorded signals. In addition, a brief introduction to contrast agent based OA imaging with emphasis on medical applications such as cancer imaging will be given. Although, MS OA imaging may be employed in other contexts, the following discussion shall

focus on applications in biomedical imaging.

In MS OA imaging, the sample region of interest is serially excited with laser pulses of different wavelengths. As briefly explained earlier, the OA signal strength is determined by the magnitude of the absorption coefficient at the particular wavelengths used to excite the chromophores in the sample. Assuming that all chromophores of interest have a significantly different absorption spectrum (Figure II.3b), their local distribution can be resolved based on their relative contribution to the emitted signal at the different wavelengths employing suitable algorithms (a mathematical discussion of the topic may be found in Subsection II.3.4). For instance, a zero order approximation would just neglect any cross-talk between two measured OA signals at 700 nm and 900 nm and it could be argued that the corresponding reconstructed images indicate the distribution of oxygenated and deoxygenated hemoglobin respectively Figure II.3b.

Ultra-fast MS volumetric OA imaging is also referred to as five dimensional OA imaging (three spatial, one temporal and one spectral dimension) in the literature. To illustrate this concept, the absorption spectrum of different chromophores that are very common in OA imaging are plotted in Figure II.3b. The identical sample volume is illuminated with a set of wavelengths, whose magnitude must increase with the number of chromophores that are being considered and the excited OA signals are subsequently recorded. After the signals had been unmixed, an image that resembles the local distribution of each chromophore can be reconstructed. Figure II.6 shows an example of an image that was acquired through MS VOT using a SMTA system. Since hemoglobin is highly absorbing in the visible and near-infrared, the most dominant contrast in biomedical OA imaging is delivered by the local blood concentration, therefore making blood vessels the most characteristic visible structure in biomedical OA images. The quantitative difference in absorption coefficient of Oxygenized Hemoglobin (HbO) and Deoxygenized Hemoglobin (HbR) has been utilized to determine blood oxygen saturation. This parameter has been used to relate brain region specific neuronal responses to external stimulation [15, 94, 101] or to identify tumors based on tissue hypoxia [102]. Another important highly absorbing and naturally occurring chromophore in biomedical imaging is melanin and it has been shown that Multispectral Optoacoustic Tomography (MSOT) may be employed to monitor the progression of melanomas [103].

So far, only intrinsic chromophores i.e. substances that occur naturally were discussed. However, it has been shown in the past that a wide selection of other substances such as nanoparticles, dyes or even reporter gene products can be used as OA contrast agents in various imaging scenarios [23, 104]. For example, nanoparticles such as silica-coated gold nanorods are highly absorbing and create a very strong OA signal [105]. By injecting this agent into the blood stream, the signal-to-noise ratio from deeply seated tissue structures may be significantly enhanced and the use of this agent therefore allows for deep tissue imaging [105]. Conjugation of nanoparticles or organic dyes such as ICG to drugs or other substances of interest additionally allows to resolve the local accumulation of that substance or its clearing time, thus allowing for pharmacokinetic or drug delivery studies in organs or tumors [106–111]. Besides, OA was recently shown to resolve fluorescent proteins [27, 112, 113]. The spatio-temporal characterization of such reporter-molecules is key to understand morphological and signaling path-ways in cells. However, even though many of these agents show promising applications in a wide range of biomedical research, most of them have not been broadly studied in a clinical context due to the lack of approval by the Food and Drug Administration.

The biggest challenge in MS OA imaging, however, is to correct for the fluence dependency of different wavelengths. As it was discussed before (also see Figure II.3b), photons of different wavelengths i.e. different energy, interact differently with their surrounding matter when they

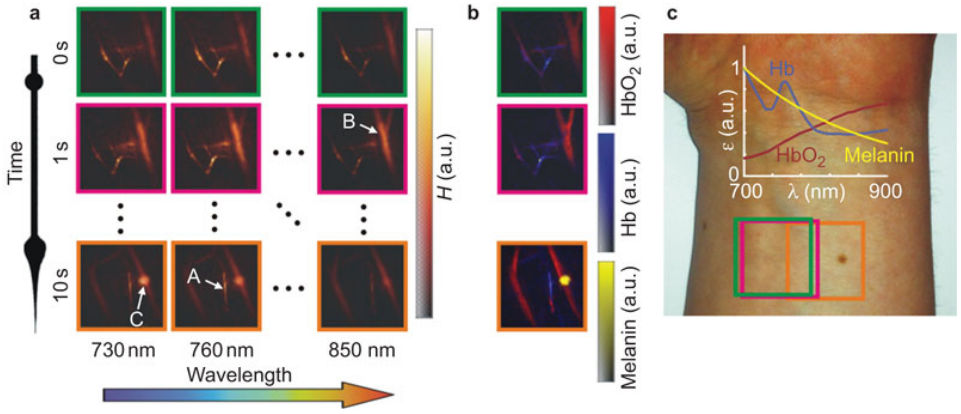

Figure II.6: The concept of MS OT imaging. **(a)** A fast-tuning laser is used to excited OA signals at different wavelengths while the probe is moved across the human wrist. **(b)** The OA signals are then unmixed to resolve the distribution of HbO and HbR as well as melanin. **(c)** Illustration of the imaging path of the probe across the human wrist. Image from [28].

propagate through the tissue [114]. Specifically, their respective absorption and scattering coefficient depends on their energy. As a result, the local photon density inside the tissue is different for every wavelength which may severely corrupt the accuracy and quantitativeness of the calculated spatial distribution of chromophores [115]. In order to model the propagation of light in tissue, the *Radiative Transfer Equation* has to be solved for heterogeneous media, a complex integro-differential equation of which analytical solutions for practical geometries are not available [114]. More practical strategies model tissue as homogeneous medium and further assume a diffusive propagation regime of the photons i.e. the photons perform a random walk inside the tissue. As discussed earlier, the propagation regime of photons is ballistic within the first microns of tissue and eventually becomes diffusive at about 0.5 mm [29]. Under these assumptions, the radiative transfer equation may be simplified to an ordinary diffusion equation with the diffusion constant given by [114]:

$$D = \frac{1}{3}\frac{1}{\mu_a + \mu_s\,(1-g)} \tag{1.3}$$

where μ_a is the absorption coefficient, μ_s is the scattering coefficient and g is the asymmetry factor, a measure of the preferred scattering direction. Analytic solutions for this equation have the form of a decaying exponential and can be utilized as a simplified model for the propagation of photons in tissue. Obviously, this does not correct for fluence variations due to absorbing chromophores. In order to really enable quantitative MS OA imaging, a more realistic model of photon propagation as well as a-priori knowledge about the location of absorbers in the tissue must be employed [116–118]. The actual clinical relevance of MS OA imaging therefore remains to be proven. For further material on MS OA imaging and contrast agents the reader is referred to recent reviews of the field [26, 31, 119].

II.2 The Conducted Research

Throughout the following section, the research that was conducted for this thesis will be motivated. Specifically, the thesis is concerned with the development of two novel multi-scale VOT imaging systems and their application. The section commences by describing current

trends in VOT before the discussion will continue by identifying the limitations that are associated with the state of the art technology. Eventually, the methods that were developed in this thesis will be motivated by explaining their expected contribution in advancing VOT as biomedical imaging modality. The research presented in this thesis was published in international peer-reviewed journals and a summary of all publications may be found in Chapter I.

II.2.1 Motivation

In Subsection II.1.3, different OA imaging implementations and system designs were introduced. In particular, the concept of OT was discussed and some of the recent developments and applications of the technology were reviewed. Among other advancements, it was argued that the introduction of matrix transducer arrays was on of the most important conceptual innovations in OA imaging. By combining hundreds of transducers in a compact probe design, it is possible to reconstruct an OA image using only one laser shot. A prominent example for such an approach is the SMTA that was introduced in [70] and it was described in detail in the last section. In general, the field of OT imaging may be separated into two major fields of application

First, there is an emerging trend of utilizing the superior imaging qualities of OT for diagnostic purposes in preclinical and clinical studies in humans as well as clinical model organisms such as mice. The increasing demand for fast, high-contrast and portable imaging modalities make OA an ideal candidate. In particular, the applicability of SMTA as hand-held imaging modality was demonstrated in preclinical studies such as real-time screening of the dense human breast [79] as well as deep human tissue angiography [80]. In Subsection II.1.2, it was established that the contrast in OA imaging is optical i.e. the reconstructed pressure map corresponds to the local absorption strength of the sample. However, substantial efforts are dedicated to combine OA with US tomography [120, 121] which is particularly interesting for multiple reasons. First, physicians usually feel very confident and are well trained in using US imaging for diagnostic purposes. A hybrid imaging approach therefore would accelerate the clinical transition of OA imaging by enriching the well established US modality through OA data. Recent studies suggest that this novel approach holds great promise in the fields of functional and bimolecular imaging [62, 122]. Second, OA signals are mediated through US waves and their propagation inside the tissue from their origin to the detector is affected by acoustic heterogeneities and attenuation. For OA image reconstruction, it is frequently assumed that the sample may be modeled as homogeneous medium and therefore OA images often suffer from image artifacts. Reconstruction algorithms accounting for these effects are available, but their application demands a-priori knowledge of parameters such as speed of sound and attenuation maps. These parameters, however, can be estimated from transmission and reflection US measurements. Finally, US contrast is based on acoustic mismatch and a hybrid approach would greatly increase the diagnostic power since the two modalities deliver different characteristics of the imaged sample.

Previous hybridization strategies were based on adding a laser fiber cable to a conventional US imaging probe that is capable of sending and receiving US waves [83, 123]. The system can be operated in US or OA imaging mode by either mechanical excitation through the probe or optical excitation through the laser cable. Even though promising results were achieved using this approach, the use of a conventional linear US array only allowed for two dimensional imaging. Moreover, the utilized arrays were not ideal for OA imaging and the achieved imaging quality therefore was poor. Recently, an alternative approach based on passive ultrasound emitters has been suggested. Instead of adding a laser source to a conventional US system, it

was shown that US waves can be created through optical excitation of a strongly absorbing element and therefore allow for a significant reduction in system complexity as no further hardware is required to excite US waves. The cost of an OA imaging system is barely increased by introducing passive ultrasound emitters. Thus, the proposed technology has the potential to become a low cost and portable medical imaging device, which can facilitate the development of hand-held diagnostics kits with potential applications in detection of oral cancer, breast cancer, cardiac ailments and other diseases. It was further shown that this approach enables to perform reflection ultrasound measurements, allowing to locate the distribution of acoustic scatterers [124], and transmission ultrasound measurements, allowing to extract speed of sound [125] and attenuation maps [126].

The second major field of application focuses on utilizing OT in fundamental research performed on small model organisms such as mice or zebrafish. During the past 30 years, there was a significant increase in the number of research publications that employed small-animals such as mice and rats as model organisms [127]. Today, small-animals are an essential part of biomedical research and they are inevitable to study diseases progression or evaluate novel treatment options. The development of new small animal imaging systems can provide improvements in basic biological and drug development research. For that reason, conventional imaging modalities that were used in diagnosing humans have been redesigned to specifically fit the demands for small-animal imaging throughout the past decades. Among them, magnetic resonance imaging (MRI) [128], X-Ray computed tomography [129] and positron emission tomography (PET) [130]. Recently, there is an increasing effort to employ OA for small-animal studies. As it was describes in detail in Subsection II.1.2, OA offers optical contrast from deeply situated tissue structures at high-resolution. Moreover, MS OA imaging allows to deliver endogenous and exogenous contrast and therefore is particularly interesting for small animal studies as it can provide anatomical, functional, and molecular imaging data of the whole body. Small animal whole-body OA imaging was first presented more than a decade ago [66] and since then has undergone a massive development. Throughout the past years, numerous different system designs were presented. Usually, an OA matrix transducer array is raster-scanned around the sample and the recorded from multiple positions are considered collectively in the reconstruction process. Previously introduced designs utilized linear arrays [68, 87], arc shaped arryas [69, 86, 106] or spherical arrays [131] to perform whole-body imaging.

II.2.2 Thesis Objectives

The objective of this thesis is the development of two novel imaging platforms that overcome current limitations and therefore enable to image dynamic processes at multiple scales and in three dimensions.

First, it is aimed to develop a hybrid US and OA imaging platform with volumetric real-time imaging capacity that can be used as a hand-held probe. Previous designs aiming to combine OA and US tomography are not suitable for practical real-time preclinical and clinical imaging applications. The existing solutions require signal averaging due to poor signal-to-noise performance and scanning of the US detectors or the imaging sample [124, 125, 132]. The proposed systems are therefore not suited for hand-held operation. In addition, all current systems are limited to two dimensional imaging. The proposed research intended to overcome these limitations by using passive elements in combination with SMTA to enable real-time three-dimensional hybrid US and OA hand-held imaging. In addition, the real-time multi-scale imaging capacity of the developed system is investigated through multiple realistic imaging scenarios such contrast-agent imaging as well as in-vivo imaging of mice and humans. Ultimately,

the system is utilized in a clinical scenario to monitor lesion formation in Endovenous Laser Therapy (ELT).

Furthermore, it is aimed to develop a novel MS OT imaging system that allows to investigate dynamical processes in small animals in real-time and in-vivo. All previous small animal imaging designs were either limited to ex-vivo samples or could not deliver volumetric real-time images and are therefore unable to investigate dynamic biological processes. The newly developed system utilizes a SMTA to deliver whole-body anatomical images of small-animals in-vivo with the additional capacity to deliver volumetric real-time data of specific regions. The potential of the proposed system to study spatio-temporal processes on multiple scales is demonstrated by imaging various dynamic phenomena in mice by perfusion studies, pharmacokinetic studies as well as longitudinal tumor studies. The real-time capacity of the SMTA that is used in the developed system is further exploited to investigate hemodynamic changes in mouse brains induced by oxygenation stress and epileptic seizures.

II.3 Theoretical Background

This section is concerned with the mathematical derivation of the OA equation and its solution as well as an introduction to unmixing strategies that are commonly employed in MS OA imaging applications.

II.3.1 The Optoacoustic Equation

This section is dedicated to motivate the OA equation which is key in deriving reconstruction algorithms in OA imaging. For a detailed derivation of the OA equation, the reader is referred to the standard literature on the matter [8, 25, 35, 133, 134]. In Subsection II.1.2, the OA effect i.e. the conversion of optical energy into mechanical vibrations via the thermoelastic effect, was introduced. The thermoelastic effect in turn is known as the phenomenon of converting mechanical deformation into heat and vice versa. In the following, a volume element V inside the imaged sample shall be considered. The sample further is optically excited with an expanded laser beam and the photon flux inside the sample is homogeneous. The incoming photons are absorbed by the sample volume V and if other relaxation path ways such as fluorescence can be neglected, the temperature rise is given by [8]:

$$\Delta T = \frac{A_e}{\rho\, C_V} \tag{3.1}$$

where A_e is the specific optical energy absorption per volume, C_V is the specific heat capacity at constant volume and ρ is the local density. In order to safely neglect heat diffusion into neighbouring volume, the acoustic confinement time d_s/c must be much smaller than the thermal confinement time $d_c^2/4\alpha_{th}$. This constraint however sets an upper limit on the laser pulse duration [25]:

$$t_L < \frac{d_s}{c} < \frac{d_c^2}{4\,\alpha_{th}} \tag{3.2}$$

where t_L is the laser pulse duration, d_s is the characteristic length scale of the absorber volume V, c is the acoustic speed of sound and α_{th} is the thermal heat conductivity. The previous equation may be utilized to estimate the required pulse duration time. Assuming that the resolution to be achieved is $100\,\mu m$ and the speed of sound in water is $c = 1500\,\mathrm{m/s}$, then

the pulse duration must be around 66 ns. However, the fractional volume expansion of V is goverend by [8]:

$$\frac{dV}{V} = \beta\,\Delta T - \kappa\,p_0 \tag{3.3}$$

where β is the thermal coefficient of volume expansion and κ is the isothermal compressibility. ΔT is the local temperature rise and p_0 is the resulting pressure increase. If the confinement inequality, equation 3.2, holds true, the pulse durations are short and the fractional volume expansion can be neglected. The pressure may then be directly related to the temperature increase [8]:

$$p_0 = \frac{\beta}{\kappa}\,\Delta T = \Gamma\,A_e \tag{3.4}$$

where the Grüneisen parameter $\Gamma = \beta/\kappa\,\rho\,C_V$ was defined. The spatio-temporal propagation of the initial pressure distribution is governed by the inhomogeneous scalar wave equation with the second derivative of the local temperature increase as source function [8]:

$$\left(\partial_t^2 - c^2\,\boldsymbol{\nabla}^2\right)\,p = \frac{\beta}{\kappa}\,\partial_t^2\,\Delta T \tag{3.5}$$

Assuming that equation 3.2 is fulfilled, the source function may be rewritten in terms of a heating function defined as the thermal energy converted per unit volume and per unit time:

$$H = \Phi\,\mu_a = \rho\,C_V\,\partial_t\,\Delta T \tag{3.6}$$

which is related to the local light fluence rate Φ and the absorption coefficient μ_a. The OA equation then reads:

$$\boxed{\left(\partial_t^2 - c^2\,\boldsymbol{\nabla}^2\right)\,p = \Gamma\,\partial_t\,H} \tag{3.7}$$

It is important to note that constant heating does not excite OA signals due to the first time derivative of H in the source term. Only a time dependent heating protocol results in an initial pressure distribution.

II.3.2 Solving the Optoacoustic Equation

While the last section dealt with the mathematical derivation of the OA equation, focus will be given to find its solution in the following. The OA equation is given by:

$$\left(\partial_t^2 - c^2\,\boldsymbol{\nabla}^2\right)\,p(\mathbf{r},\,t) = \Gamma\,\partial_t H(\mathbf{r},\,t) \tag{3.8}$$

Applying the following transformation:

$$t = t_0\,\tau \tag{3.9}$$

$$\mathbf{r} = r_0\,\boldsymbol{\rho} \tag{3.10}$$

and setting $t_0 = \Gamma$ and $r_0 = c\,\Gamma$ yields the dimensionless form of the OA equation:

$$\left(\partial_\tau^2 - \boldsymbol{\nabla}^2\right)\,p\,(\boldsymbol{\rho},\,\tau) = \partial_\tau H(\boldsymbol{\rho},\,\tau) \tag{3.11}$$

where the Laplacian now acts on $\boldsymbol{\rho}$. Transforming equation 3.11 into Fourier space yields:

$$\left(\omega^2 + \nabla\right) \tilde{p}\left(\boldsymbol{\rho}, \omega\right) = -i\,\omega\,\tilde{H}(\boldsymbol{\rho}, \omega) \tag{3.12}$$

where the following Fourier convention was used:

$$\tilde{p}(\boldsymbol{\rho}, \omega) = \int d\tau\, e^{i\,\omega\,\tau} p(\boldsymbol{\rho}, \tau) \tag{3.13}$$

$$p(\boldsymbol{\rho}, \tau) = \frac{1}{2\pi} \int d\omega\, e^{-i\,\omega\,\tau} \tilde{p}(\boldsymbol{\rho}, \omega) \tag{3.14}$$

This equation is commonly known as the inhomogeneous *Helmholtz equation* and it may be solved easily using Green's theory [135]:

$$\tilde{p}\left(\boldsymbol{\rho}, \omega\right) = -i\,\omega \int d\rho'^3\, G\left(|\boldsymbol{\rho} - \boldsymbol{\rho}'|, \omega\right)\; H(\boldsymbol{\rho}', \tau) \tag{3.15}$$

where $(\omega^2 + \nabla^2) G(|\boldsymbol{\rho} - \boldsymbol{\rho}'|, \omega) = \delta(\boldsymbol{\rho} - \boldsymbol{\rho}')$. It shall be noted that the homogeneous solution is zero in this case. The *retarded* Green's function for the Helmholtz operator must have the form of an outgoing wave and therefore is given by [135]:

$$G\left(|\boldsymbol{\rho} - \boldsymbol{\rho}'|, \omega\right) = \frac{1}{4\pi} \frac{e^{i\,\omega\,|\rho - \rho'|}}{|\boldsymbol{\rho} - \boldsymbol{\rho}'|} \tag{3.16}$$

Equation 3.15 may now be back transformed into time domain by performing the inverse Fourier transform:

$$p\left(\boldsymbol{\rho}, \tau\right) = \frac{1}{4\,\pi} \int d\rho'^3 \left(\frac{1}{2\,\pi} \int d\omega\, (-i\,\omega)\, \frac{\tilde{H}\left(\boldsymbol{\rho}', \omega\right) e^{-i\,\omega\,(\tau - |\rho - \rho'|)}}{|\boldsymbol{\rho} - \boldsymbol{\rho}'|} \right) \tag{3.17}$$

The $i\,\omega$ factor translates into a derivative in time domain and the dimensionless solution to the OA equation is given by:

$$\boxed{p\left(\boldsymbol{\rho}, \tau\right) = \frac{1}{4\,\pi} \int d\rho'^3\, \frac{\partial_\tau H\left(\boldsymbol{\rho}', \tau - |\boldsymbol{\rho} - \boldsymbol{\rho}'|\right)}{|\boldsymbol{\rho} - \boldsymbol{\rho}'|}} \tag{3.18}$$

Before proceeding further, an important simplification shall be introduced. It is commonly assumed that the heating function H can be decomposed into

$$H\left(\boldsymbol{\rho}, \tau\right) = f(\boldsymbol{\rho})\, I(\tau) \tag{3.19}$$

and if the laser pulse duration is short, i.e. equation 3.2 is fulfilled, it is further assumed that $I(\tau) = \delta(\tau)$ can be approximated by a delta distribution. With these assumptions, the OA equation essentially describes a *Spherical Radon Transformation* where the value of $p(\boldsymbol{\rho}, \tau)$ is given by the integral of $f(\boldsymbol{\rho}')$ over the spherical integration surface defined by $\tau = |\boldsymbol{\rho} - \boldsymbol{\rho}'|$.

II.3.3 Image Reconstruction Strategies

This section is dedicated to a brief introduction to OA reconstruction strategies. However, before commencing the discussion, it shall be noted that the literature on OA image reconstruction is rich and a systematic review of it is far beyond the scope of this thesis. The following paragraph is used to give a brief introduction to the two basic reconstruction concepts and the idea behind

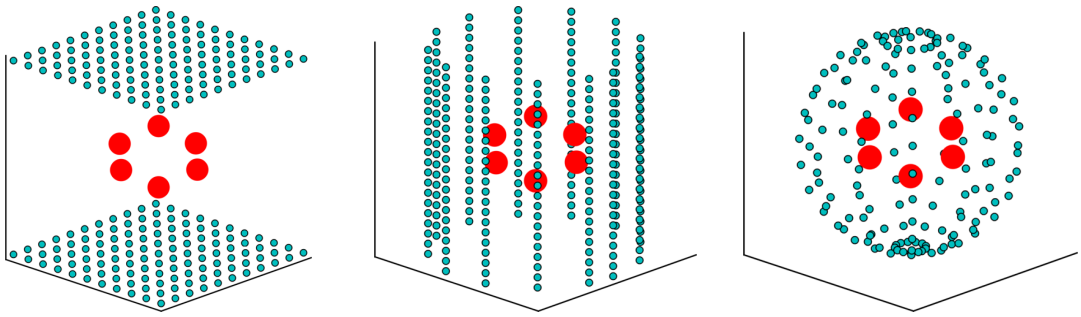

a Planar detection surface. **b** Cylindrical detection surface. **c** Spherical detection surface.

Figure II.7: Basic geometries with detectors distributed on a planar (Figure II.7a), cylindrical (Figure II.7b) and spherical (Figure II.7c) surface enclosing the OA source distribution (red).

them. For a more detailed introduction, the reader is referred to articles and books [30, 35, 136].

In general, OA inversion is concerned with question how the initial pressure distribution $f(\boldsymbol{\rho})$ in equation 3.18 can be recovered from a finite number of time-resolved pressure measurements around the sample. It was shown that inversion can be performed on any surface shape as long as it fully encloses the sample [137] but analytical solutions are known only to planar (Figure II.7a), cylindrical (Figure II.7b) and spherical (Figure II.7c) geometries [72]. Besides the research on finding computationally efficient and implementable algorithms, there are other important factors that have to be taken in consideration for accurate image reconstruction.

Transducers usually only have a limited frequency sensitivity bandwidth that limits their resolution to a certain length scale. For instance, the SMTA that was introduced earlier is only sensitive between approximately 2 and 4 MHz (see Figure II.5b) [70]. The effect of the finite bandwidth is usually quantified by measuring the response of every transducer to a δ-distribution like pressure signal. The frequency spectrum of a delta distribution is a real constant and the measured spectrum therefore characterizes the frequency bandwidth of the transducer. The influence of the impulse response function on the resolution has been investigated by many authors [24, 138, 139] and one way to account for its influence is simply through deconvolving the measured signals with that function.

Another factor that causes artifacts in reconstructed OA images is the finite detector aperture. An ideal OA detector is point-like and recovers the actual pressure value at the measurement position. In practice, however, the surface of the transducers must be finite to guarantee sufficient signal-to-noise ratio. The aperture must be chosen based on the frequency bandwidth of the transducer and ideally is much smaller than the wavelengths of the frequency of interest. If this criterion is not fulfilled, the transducer essentially acts as a low-pass filter and the higher frequency are not represented accurately in the reconstructed image. Literature on how to account for this effect in the reconstruction procedure may be found in [139–142].

Finally, in most practical situations it is not possible to carry out signal measurements on a closed surface and pressure observations are limited to a subset of the full detection geometry. For instance, the reconstructed OA images of hand-held probes such as the SMTA from [70] which only has an angular coverage of 90° are suffering from limited view effects. Obviously, it is not possible to correct for this effect since the required data is not available and the ongoing research mainly tries to identify means to limit the impact of this effect on the reconstructed image [143–145].

II.3.3.1 The Back-Projection Formula

Probably the most influential paper on OA image reconstruction was published by Xu et al. in 2005. In their paper, Xu et al. derived an universal reconstruction formula that is valid in all three common inversion geometries i.e. planar, cylindrical and spherical [72]. As compared to previous publications, this formula is not based on an approximation but it is an actual analytical inversion of equation 3.18. Assuming that $f(\boldsymbol{\rho})$ vanishes outside the detection surface Ω, the initial pressure distribution is given by [72]:

$$f(\boldsymbol{\rho}) = \frac{1}{\Omega_0} \int\limits_{\Omega} d\Omega' \, b\left(\boldsymbol{\rho}', \tau = |\boldsymbol{\rho} - \boldsymbol{\rho}'|\right) \frac{(\boldsymbol{\rho} - \boldsymbol{\rho}')}{|\boldsymbol{\rho} - \boldsymbol{\rho}'|^3} \, d\boldsymbol{S} \tag{3.20}$$

where $b(\boldsymbol{\rho}, \tau) = 2(1 - \tau \, \partial_\tau) p(\boldsymbol{\rho}, \tau)$ with $p(\boldsymbol{\rho}, \tau)$ being the measured pressure at detector position $\boldsymbol{\rho}$ and time τ and Ω_0 is $2\,\pi$ for the planar and $4\,\pi$ for the cylindrical and spherical geometry. This highly elegant formula offers many advantages and revolutionized OA image reconstruction. Since it is a linear equation, its computational implementation is simple and feasible even at large detector numbers. In addition, its linearity makes it highly parallelizable and therefore allows for real-time image reconstruction at frame rates up to 50 Hz [73] – a feature that is unique to this particular approach. Finally, the back-projection approach yields stable results even if only very few detection positions are considered in the reconstruction procedure. Even though back-projection essentially performs analytical inversion, its results may be not ideal in practice. The formula is based on the assumption that detection is carried out on the full geometry, i.e. the whole sphere in case of a spherical geometry, which is often not feasible in practice. As a result, the reconstructed images are typically affected by characteristic arc artifacts that result from projecting only signals from a subset of the full detection geometry e.g. a hemisphere [136].

II.3.3.2 The Model-Based Approach

Another important approach in OA image reconstruction is based on inverting a discretized version of the OA equation in either time or frequency space. The integral in equation 3.18 or any bijective linear transformation of it is discretized and rewritten in terms of a matrix equation where every point in space and time is represented by a vector entry:

$$p\left(\boldsymbol{\rho}, \tau\right) \quad \rightarrow \quad p_{i=(d-1)\,n+\tau} \tag{3.21}$$

$$f\left(\boldsymbol{\rho}\right) \quad \rightarrow \quad f_j \tag{3.22}$$

where n is the total number of recorded time points per detector and $d = 1, 2, ...$ indexes the dectors. The resulting system of equations may be written in matrix form:

$$\boldsymbol{p} = \boldsymbol{M} \, \boldsymbol{f} \tag{3.23}$$

where the model matrix $\boldsymbol{M}$ is a distretized version of the integral in equation 3.18. This system of equation is highly underdetermined and regularization therefore is inevitable in practice. Solutions are found by minimizing a certain metric Ψ together with multiple regularization terms:

$$f_0 = \min_{\boldsymbol{f}} \; \Psi(\boldsymbol{p} - \boldsymbol{M} \, \boldsymbol{f}) + \sum_i \mathrm{Reg}(\boldsymbol{f}) \tag{3.24}$$

Although $\boldsymbol{M}$ is usually sparse, the number of equations (number of rows) still equals the number of pixels in the reconstructed image. The choice of available inversion algorithms therefore is very limited for volumetric reconstructions where pixels are in the order of millions and the computational implementation is challenging. On approach assumes a L_2 metric and a Tikhonov regularization term to find solutions using the LSQR algorithm [146]. Others employed a L_1 metric or used the total variation to regularize solutions [147, 148]. Model-based inversion schemes were also implemented in the Fourier domain [149]. Even though model-based approaches are much slower than back-projection based inversion schemes, they offer many interesting advantages. For instance, it is possible to model the effect of the finite detector size [141] by modeling the experimentally measured signal as the integral over the detector surface:

$$p\left(\boldsymbol{r},\,\tau\right)_{exp} = \int\limits_{S} dS'\, p(\boldsymbol{\rho}',\,\tau) \tag{3.25}$$

which essentially transforms the model matrix $\boldsymbol{M}$ into a sum of model matrices with every detection position $\boldsymbol{d}$ slightly shifted from the original position $\boldsymbol{d} \rightarrow \boldsymbol{\rho} + \boldsymbol{\delta}_i$:

$$\boldsymbol{M} \rightarrow \sum_i \boldsymbol{M}_i \tag{3.26}$$

Another advantage is that solutions can be constrained to fulfill a physical criterion e.g. all pixel values in the reconstructed image must be positive [150]. Other authors used an model-based approach to incorporate a model for light fluence into the inversion process [151–153].

In conclusion, the model-based approach offers many unique advantages that often outweigh its computational complexity.

II.3.4 Spectral Unmixing

In Subsection II.1.4, the concept of MS OA imaging was established and throughout the following subsection it will be elaborated on how the recorded MS signals can be unmixed assuming a linear model. Assuming that the OA excitation $H(\boldsymbol{\rho}, \tau; \lambda_i)$ for a specific wavelength at time τ and position $\boldsymbol{\rho}$ is generated by N substances yields:

$$H(\boldsymbol{\rho}, \tau; \lambda_i) = \sum_{j=1}^{N} \Phi(\boldsymbol{\rho}, \tau; \lambda_i)\, \epsilon_j(\lambda_i)\, c_j(\boldsymbol{\rho}) \tag{3.27}$$

where $\Phi(\boldsymbol{\rho}, \tau; \lambda_i)$ models the light fluence, $\epsilon_j(\lambda_i)$ represents the specific molar extinction coefficient for the j^{th} absorber and $c_j(\boldsymbol{\rho})$ is the local concentration of the j^{th} substance. Assuming further that the laser pulse durations is short yields:

$$\Phi(\boldsymbol{\rho},\, \tau;\, \lambda_i) \rightarrow U(\boldsymbol{\rho};\, \lambda_i)\, \delta(\tau) \tag{3.28}$$

where $U(\boldsymbol{\rho};\, \lambda_i)$ describes the local photon fluence for every wavelengths. Using equation 3.27 together with equation 3.18 then yields the following system of equations:

$$p(\boldsymbol{\rho},\, \tau;\, \lambda_i) = \sum_{j=1}^{N} \epsilon_j(\lambda_i)\, \frac{1}{4\,\pi}\, \partial_\tau \frac{1}{\tau} \int d\rho'^3\, \delta\left(\tau - |\boldsymbol{\rho} - \boldsymbol{\rho}'|\right)\, U(\boldsymbol{\rho};\, \lambda_i)\, c_j(\boldsymbol{\rho}) \tag{3.29}$$

$$= \sum_{j=1}^{N} \epsilon_j(\lambda_i)\, p_j(\boldsymbol{\rho},\, \tau;\, \lambda_i) \tag{3.30}$$

If it is now assumed that the fluence is independent of the wavelength, the previous equation may be treated as linear model and the local distribution of every contributing substance may be reconstructed independently after solving for its corresponding pressure contribution. Assuming signals were acquired at $M \geq N$ different wavelengths yields:

$$\begin{pmatrix} p(\boldsymbol{\rho}, \tau; \lambda_1) \\ p(\boldsymbol{\rho}, \tau; \lambda_2) \\ \vdots \\ p(\boldsymbol{\rho}, \tau; \lambda_M) \end{pmatrix} = \begin{pmatrix} \epsilon_1(\lambda_1) & \epsilon_2(\lambda_1) & \dots & \epsilon_N(\lambda_1) \\ \epsilon_1(\lambda_2) & \epsilon_2(\lambda_2) & \dots & \epsilon_N(\lambda_2) \\ \vdots & \vdots & \vdots & \vdots \\ \epsilon_1(\lambda_M) & \epsilon_2(\lambda_M) & \dots & \epsilon_N(\lambda_M) \end{pmatrix} \begin{pmatrix} p_1(\boldsymbol{\rho}, \tau) \\ p_2(\boldsymbol{\rho}, \tau) \\ \vdots \\ p_N(\boldsymbol{\rho}, \tau) \end{pmatrix} \tag{3.31}$$

and the actual pressure distribution of every substance may be recovered by applying the pseudo-inverse. It shall be noted that this presented procedure can also be applied to the reconstructed images, since a linear operation is required to invert the OA equation. In that case, the entries in the vectors on both sides of the linear Equation 3.31 are replaced with the corresponding pixel value for each of the wavelengths. So, instead of unmixing for every time instances and detector position, one can equally unmix for every voxel. This approach is commonly referred to as linear unmixing in OA imaging. Even though it does not account for the fluence dependence of different wavelengths, it yields stable results if imaging is performed superficially [116]. Recently, blind source unmixing strategies that do not require a-priori knowledge about chromophores have also been proposed [154, 155]. However, all these algorithms do not account for the wavelength dependence of light fluence and finding suitable unmixing procedure is still subject to ongoing investigation. As of now, it is not even clear how to choose the number of wavelengths and how to distribute them across the spectrum in order to achieve best unmixing results.

III Development of Multi-Scale Ultrasound & Optoacoustic Imaging Methods

This chapter is dedicated to the development of novel multi-scale hybrid US and OA imaging systems. Specifically, two newly developed imaging configuration will be presented. In Section III.1, a hand-held hybrid US and OA system with real-time imaging capacity based on passive element optical excitation will be introduced. The section will commence with a brief introduction, followed by a discussion of the proposed system design. The methodology and the theoretical background of passive US image reconstruction will be introduced before the imaging performance of the system will be will characterized. In Section III.2, a novel multi-scale OA imaging system with real-time capacity will then be introduced. The presentation will include a brief introduction, a discussion of the system lay-out as well as the implemented signal-processing pipeline. Eventually, the system performance will be demonstrated through phantom experiments.

To refute any allegations concerning self-plagiarism, it shall be noted that the following chapter does not provide an original presentation of the conducted research. In fact, it merely summarizes the content of the candidate's original publications i.e. [156] and [157]. However, explicit reference to the original sources will be given throughout the chapter.

III.1 Ultrasound & Optoacoustic Imaging via Passive Element Optical Excitation

III.1.1 Introduction

A similar version of the following introduction (Subsection III.1.1) was originally published in [156]. US is arguably the most dominant imaging modality employed in the clinical routine today with applications ranging from obstetrics and gynecology to cancer monitoring, intravascular and cardiac diagnostics [158–160]. The success of US is based on the remarkable combination of advantages, such as real-time operation, portability and affordability, which makes it unique among the medical imaging modalities. However, the contrast in US imaging is based on acoustic mismatch and it therefore mainly visualizes structural information. Specificity and diagnostic value are therefore generally limited [161]. One strategy to overcome this limitation lies in the hybridization of US with OA imaging. The combined approach is expected to significantly enhance the potential range of applications by delivering the optical imaging contrast advantages of the OA modality, such as spectral specificity [23, 28] and functional

imaging [95]. So far, various two-dimensional (cross-sectional) concepts have been proposed for combining OA with US imaging. One of the most common approach employs conventional linear US arrays and adds a fiber-guided light source on one or both sides of the array [83]. Pulse-echo US and OA pressure signals are then recorded in an alternate manner. Recently, a novel strategy, termed laser-induced US was proposed. The object is interrogated with a conventional cross-sectional OA scanner by introducing strong absorbers, called Passive Element (PE), positioned outside the object in the path of the excitation light [162]. It was shown that the generated US waves are strong enough to perform US transmission [125] and reflection tomography [81], thus allowing to extract transmission parameters such as speed of sound and attenuation maps as well as the usual pulse-echo contrast, along with the OA absorption maps. However, in contrast to the relatively narrowband back-reflected US waves, OA signals usually possess an ultrawide bandwidth and manifold higher tissue contrast. Performing acoustic focusing and conventional US beamforming or synthetic aperture approaches for OA image rendering is then generally challenging and reconstruction approaches that are based on these techniques lead to poor imaging performance [163]. However, to achieve superior imaging performance in OA tomography it is necessary to acquire the excited OA signals by means of unfocused detectors from as many locations around the object as possible. To meet this demand, a SMTA with 256 transducer elements was recently introduced [74]. As it was discussed earlier, this design enables real-time acquisition and rendering of volumetric OA images in contrast to two-dimensional imaging approaches. Moreover, it was shown that real-time acquisition and unmixing of volumetric MS OA images can be performed by means of fast laser wavelength tuning [28]. In this thesis, a novel concept for combined three-dimensional US and OA imaging based on the optical excitation of a passive element will be introduced. The optoacoustically excited signals from the imaged tissue are simultaneously acquired with the later arriving back-scattered US waves using a SMTA. In this way, it is possible to acquire volumetric OA and US images in real time. The presentation commences with a description of the experimental design and the employed reconstruction algorithms and concludes by showcasing the performance of the proposed system using phantom experiments.

III.1.2 Materials & Methods

A similar version of the following paragraph (Subsection III.1.2) including all sub-paragraphs was originally published in [156].

III.1.2.1 Experimental Setup

Figure III.1a shows a sketch of the proposed hand-held implementation for hybrid US and OA imaging. US waves are excited from a highly absorbing carbon microsphere, i.e. the PE, with an approximate diameter of 400 μm (SPI-Supplies, USA) through light absorption. The PE is positioned between the sample and the SMTA, which performs the detection of the back-scattered US and excited OA signals and is described in detail in [70]. In short, the individual detection elements have a size of $3 \times 3\text{mm}^2$, a central frequency of 4 MHz and a -6 dB bandwidth of 100%. A central cavity in the middle of the array enables coaxial optical excitation. The PE was embedded in agar and arranged along the central axis of the array approximately 1.5 cm above the focal point in order to guarantee efficient illumination. Optical excitation was provided through nanosecond-duration light pulses generated by a tunable optical parametric oscillator (wavelength range 690-900 nm) laser source (Innolas Laser GmbH, Germany) at a PRF of 10 Hz. The beam is guided through a custom-made fiber bundle (CeramOptec GmbH,

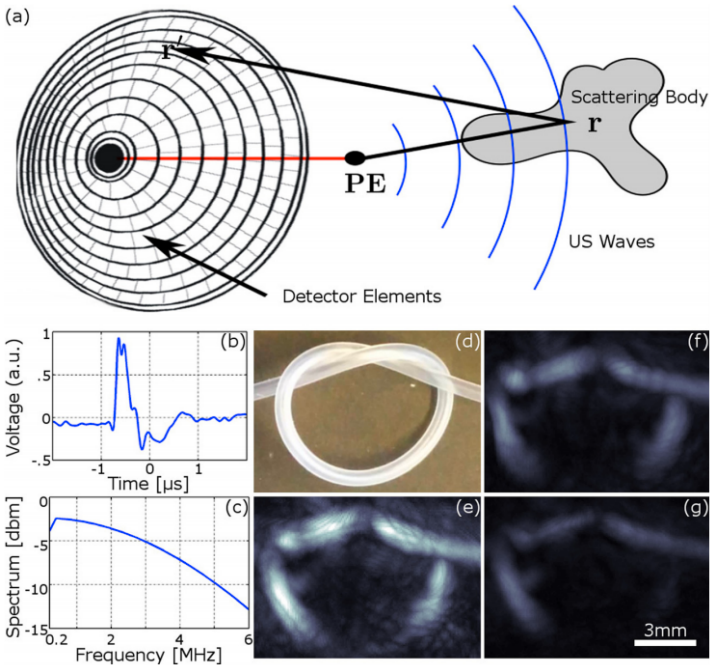

Figure III.1: **(a)** Depiction of the experimental setup. A 400 μm diameter carbon microsphere is coaxially placed with respect to the OA excitation beam between the object and the SMTA. Optoacoustically-excited US waves emitted from the PE are subsequently scattered inside the object at positions r before reaching the detector elements at positions $r\prime$. **(b)** and **(c)** Temporal profile and power spectrum density of the pressure waves emitted by the PE. **(d)** Image of the tubing phantom. **(e)**, **(f)** and **(g)** show the relative US scattering contrast achieved from air, microbubble solution, and liquid ink, respectively. The color bar corresponds to US signal strength on an arbitrary scale. From [156].

Germany) that provides a Gaussian illumination profile at the tissue surface with a Full-Width at Half Maximum (FWHM) of approximately 10 mm. Both the US and OA pressure signals are simultaneously time-resolved and digitized by a custom-made high-speed Data Acquisition System (DAQ) (Falkenstein Mikrosysteme GmbH, Germany) that is triggered with the Q-switch output of the laser. The position of the carbon microsphere allows separating the OA waves generated within the tissue and the echoes from the PE US beam by simple time-windowing of the recorded pressure signals.

III.1.2.2 Signal Processing & Image Reconstruction

Volumetric OA image reconstruction was performed using a back-projection algorithm [72] that was implemented on a GPU. The OA amplitude in arbitrary units at a given pixel $H(r'_j)$ is given by:

$$H(r'_j) \approx \sum_i p_f(r_i\, t_{ij}) - t_{ij}\, \partial_t\, p_f(r_i,\, t_{ij}) \tag{1.1}$$

where r_i is the position of the i^{th} transducer element and $t_{ij} = |r'_j - r_i|/c$ is the time-of-flight between r'_j and r_i assuming a constant speed of sound c in the medium. $p_f(r_i,\, t_ij)$ are the detected temporal pressure signals, obtained from acoustic measurements at the 256 transducer positions. Before image reconstruction was performed, the recorded signals were deconvolved

with the impulse response function of the detector elements and band-pass filtered with cut-off frequencies of 0.75 and 7 MHz to account for white noise and the impact of the limited detector band-width.

In principle, a similar back-projection strategy can be employed for reconstructing the distribution of acoustic scatterers within the imaged tissue [164]. However, as it was described in the original publication [156], several factors must be considered. First, the recorded frequency spectrum of the signal emitted from the PE depends on its size, density, the longitudinal and transversal speed of sound [165]. The temporal profile of the OA signal, emitted by the PE used in this study, was characterized using a calibrated broadband hydrophone (Precision Acoustics Ltd., Dorset, UK) and is depicted in Figure III.1b along with its Fourier spectrum in Figure III.1c. The signal of the PE was low-pass filtered at 6 MHz to remove high frequency noise. The emitted spectrum clearly is broader than the effective detection bandwidth of the transducer elements of the SMTA used in this study. Second, the directivity and frequency spectrum of the back-scattered acoustic waves is further affected by the nature of scattering event. Rayleigh scattering, for example, would yield an isotropic far-field pattern and a frequency dependence of the scattering cross-section given by $1/\lambda^4$, where λ is the acoustic wavelength [166]. Under the common assumption of single scattering events in soft biological tissues (weak scattering), the spatial distribution of scatterers can be subsequently reconstructed by means of a back-projection approach, similar to the OA case. Specifically, the US image at a certain voxel $U(r'_j)$ is estimated as [156]:

$$U(r'_j) = \sum_i s(r_i,\, t_{hij}) \tag{1.2}$$

where $t_{hij} = |r_h - r'_j|/c + |r'_j - r_i|/c$ is the total time of flight from the location of the PE, r_h, to the location of the acoustic scatterer, r_j, and from there to the location of the detector, r_i. In fact, Equation 1.2 closely resembles traditional delay-and-sum US beamforming [167] but with the function $s(r_i,\, t_{hij})$ back-projected along ellipses whose foci are the PE and the location of each transducer. Note that, $s(r_i,\, t_{hij})$ may instead account for the exact forward model of broadband sound propagation and directional scattering in heterogeneous tissues. However, a theoretical derivation is highly challenging in this case since a realistic model would have to include intricate boundary conditions between regions of different acoustic properties. Nevertheless, in deriving an efficient implementation of reflection-mode US imaging using PE optical excitation, $s(r_i, t_{hij})$ in Equation 1.2 was taken as the filtered pressure $p_f(r_i,\, t_{ij})$, whereas a band-pass filter was applied (cut-off frequencies set between 2 MHz and 4 MHz) in order to optimize resolution and contrast of the images. In this way, the lower frequency boundary of the detected spectrum is responsible for establishing the diffraction-limited spatial resolution in the US imaging mode. Similarly to the conventional pulse-echo US [168], it is assumed here that the size of acoustic scatterers in the imaged tissue is much smaller than the wavelength of the detected waves.

Reconstruction in both OA and US modes is based on a CUDA implementation of the suggested algorithms and is executed on a GeForce GTX 780, which enables on-the-fly image rendering at a higher speed than the inter-pulse duration (1/PRF) of the laser. It was found that with this approach, frame rates of 100 volumes per second of a three-dimensional grid consisting of $128 \times 128 \times 96$ voxels can be achieved.

III.1.2.3 Phantom Experiments

Multiple phantom experiments were performed in order to validate the proposed hybrid approach. First, a set of experiments was carried out to characterize the lateral resolution and size of the field of view for the back-scattering US mode. For that, a glass microsphere with an approximate diameter of 500 μm (Cospheric, Santa Barbara, USA) was positioned in the vertical plane corresponding to the center of the SMTA. The reflected US signals were then recorded for different lateral positions of the sphere and US images were reconstructed using Equation 1.2.

In a second set of experiments, a polyethylene tube with an inner diameter of 0.6 mm was tangled to form a knot as displayed in Figure III.1d. The knot was positioned in the focal region of the SMTA to ensure maximal sensitivity of all transducer elements. The wavelength of the laser was set to 750 nm and signal acquisition was performed at 10 Hz. Injection of different scattering and absorbing substances such as air, a microbubble contrast agent (SonoVue®, Bracco Group, Italy) and Black India ink solution (Higgins Ink, Sanford, USA), into the tubing was performed by means of an automatic injection pump (Harvard Apparatus, Holliston, USA) using a volume rate of 0.028 ml/s ($\approx$ 1 cm/s). For validation of the real-time visualization capacity of the system, two injection experiments were performed. In the first experiment, the tubing initially contained air, which was slowly replaced by the ink solution having an effective optical absorption coefficient of $\mu_a = 2.3\,\mathrm{cm}^{-1}$. The injection rate was maintained constant until the phantom was entirely filled with the ink solution. In the second experiment, the tube was initially filled with the ink solution while the microbubble contrast agent (SonoVue®, Bracco Group, Italy) was subsequently injected for contrast enhancement.

III.1.3 Results

A similar version of the following paragraph (Subsection III.1.3) including all sub-paragraphs was originally published in [156].

III.1.3.1 Spatial Resolution Characterization

Maximum Intensity Projection (MIP) images of the volumetric reconstructions as a function of the position of the glass microsphere are shown in a movie file available in the online supplementary of the original publication (Movie 3) [156]. The size of the reconstructed microsphere for each individual position was defined as the FWHM of the maximal pixel value. The field of view was defined in an analogous manner by considering the FWHM of the maximal pixel value as a function of the lateral position of the microsphere. Figure III.2 shows a plot of the calculated values as a function of the lateral distance. The lateral size of the field of view is about 10 mm and the size of the reconstructed sphere was approximately 500 μm for all lateral positions, indicating that the spatial resolution in the pulse-echo US mode is better than 500 μm. Clearly, the size of the reconstructed sphere is affected by the diameters of both the light absorber and the acoustic scatterer. Therefore, a better estimate of the resolution can be derived when smaller microspheres are used, which, however, was not accomplished in this study due to rapid deterioration of the contrast to noise ratio for smaller scatterers. Nevertheless, it was shown before that the resolution achieved by the SMTA used in this study, was in the range 200 mm in the focal region [70], so that a similar resolution would also be expected for the ultrasound mode if a smaller PE is used.

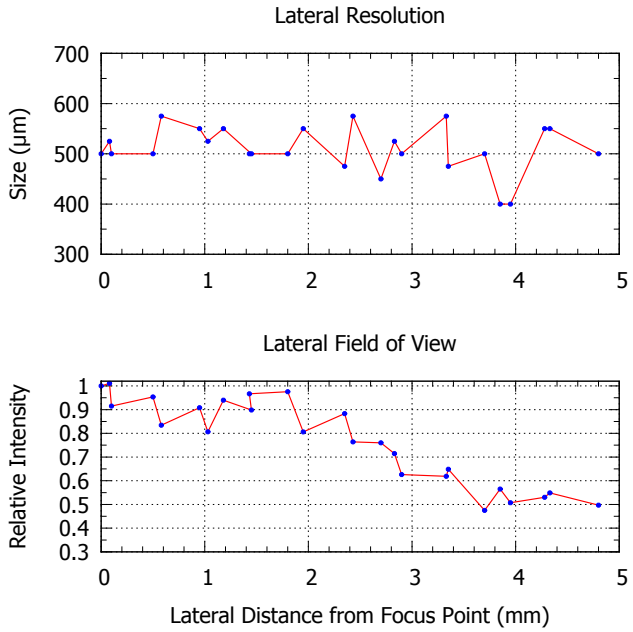

Figure III.2: Plots of the determined FWHM values for the lateral resolution and field at increasing lateral distances from the focus point. Image and caption from [156].

III.1.3.2 Verification of Contrast & Real-Time Capacity

To validate the sensitivity of the proposed approach, the knotted tubing was filled with three different substances of increasing acoustic contrast. Figure III.1e-g show the relative back-scattering US contrast provided by the phantom when filled with air, a microbubble contrast agent (SonoVue®, Bracco Group, Italy) or a Black India ink solution (Higgins Ink, Sanford, USA), respectively. The shape of the knot can be clearly identified in all three images even if the phantom is filled with low-scattering ink solution demonstrating the high sensitivity of the proposed system.

The results of the second set of imaging experiments are presented in Figure III.3. Clearly, the spatial and temporal distribution dynamics of both light absorption and acoustic scattering can be simultaneously imaged in real time. Three representative time instants are shown in Figure III.3 for the two imaging experiments. However, the entire frame series is available in the on-line version of the journal (Movie 1 and Movie 2) in which the research was originally published [156]. While air and ink only provide strong contrast in either US or OA images, the SonoVue® microbubble solution generates significant contrast for both modalities. It was found that the common US contrast agent also provides sufficient contrast for OA imaging at clinically applied concentration. However, the shape of the knot can be clearly identified in all reconstructions and the interface between the substances inside the tubing can be further tracked in real time, as shown e.g. in Figure III.3a for $t = 0.7\,\mathrm{s}$. An additional example of well-registered OA and US images can be seen in Figure III.3a for $t = 0\,\mathrm{s}$, where an ink droplet leftover from a previous experiment can be clearly identified inside the phantom. On the other hand, the onset of the US signal in Figure III.3b is delayed and reaches its full strength when the tubing is completely filled with the US contrast agent. The maximum value of the US image in Figure III.3b at $t = 1.5\,\mathrm{s}$ was determined to be approximately two thirds of the air filled phantom in Figure III.3a at $t = 0\,\mathrm{s}$.

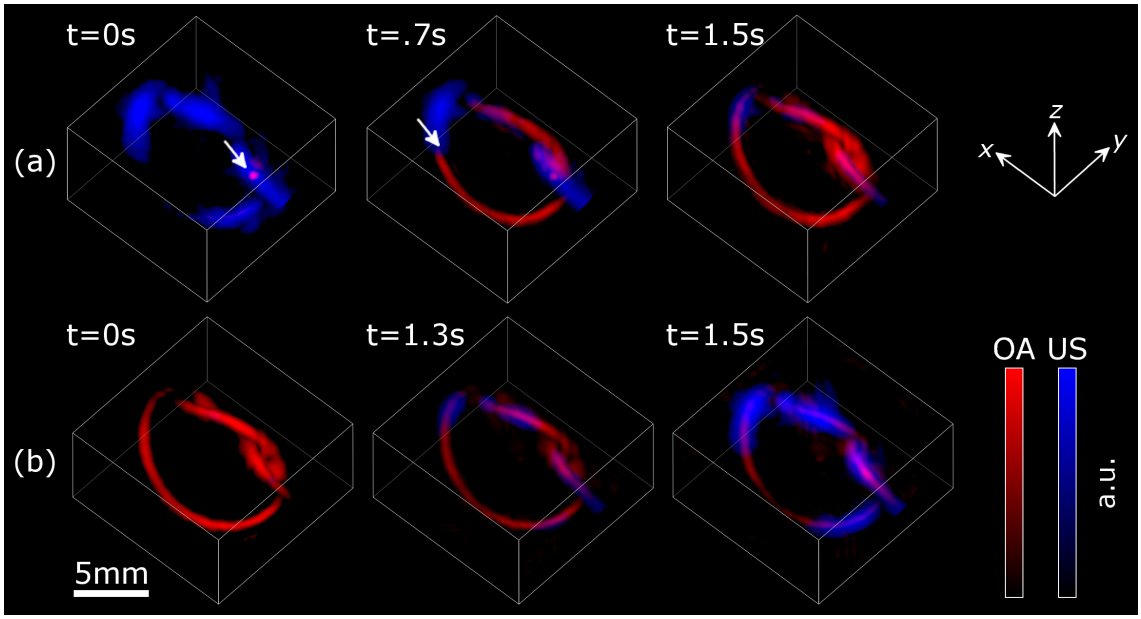

Figure III.3: Volumetric hybrid visualization of fast contrast variations. **(a)** The series of reconstructed OA (red color) and US (blue color) images represent the tubing phantom filled with air before an ink solution ($\mu_a = 2.3\,\mathrm{cm}^{-1}$) is injected at $t = 0\,\mathrm{s}$. Details like an ink droplet leftover from a previous experiment and the boundary between air and the ink solution when the tubing is partially filled are indicated by white arrows. **(b)** Image series from the second experiment where the phantom is initially filled with the ink solution before the microbubble contrast agent is injected. The maximal US signal strength provided by the microbubbles is achieved at $t = 1.5\,\mathrm{s}$. From [156].

III.1.4 Discussion

A similar version of the following discussion (Subsection III.1.4) was originally published in [156]. Throughout this section, simultaneous OA and US image acquisition at an unprecedented volumetric frame rate of 10 Hz was demonstrated at the first time. Hereby, it is important to notice that the conventional three-dimensional US, performed in the active send-receive mode, is severely limited in terms of its temporal resolution due to the large number of A-lines to be scanned. The temporal resolution of the proposed method, in contrast, is mainly limited by the PRF of the employed laser source and significantly better frame rates therefore can be achieved by using lasers with a higher PRF. However, several limitations of the proposed imaging design require further attention. The SMTA used in this study is optimized for OA tomographic imaging [70]. Its relatively low number of transducers, their orientation as well as the large pitch are not ideal for the delay-and-sum beamforming approach used in conventional pulse-echo US imaging, which can result in significant grating lobe artifacts as well as loss of spatial resolution and contrast [166]. A finer design of the detection array may therefore substantially contribute to improve the resolution in both OA and US modes. Finally, an improved hardware design, particularly pertaining the size, shape and position of the PEs is yet another crucial aspect to achieve the optimum amplitude and frequency content of the US beam.

III.2 In-Vivo Whole-Body Optoacoustic Scanner with Real-Time Capacity

III.2.1 Introduction

A similar version of the following introduction (Subsection III.2.1) was originally published in [157]. Small animal OT imaging was first suggested more than a ten years ago [66, 68]. Since then, various acquisition geometries are continuously being suggested to optimize the performance in specific imaging applications [69, 86, 87]. Generally, high-resolution volumetric imaging demands acquisition of signals generated by absorbers with various sizes and orientations, which requires a large angular coverage and a significant number of measuring locations. A promising approach to overcome this limitation consists in dimensionality reduction of the acquisition geometry by using focused arrays. For example, OA signals can be acquired with cylindrically focused detector arrays [125, 169], which can be engineered with sufficient angular coverage for accurate reconstruction of a cross-section of the imaged object with single-shot excitation and in real-time [170, 171]. However, even though the imaging volumes rendered with dimensionally reduced systems can be enhanced with more sophisticated reconstruction approaches such as synthetic aperture [172], image deconvolution [173] or model-based inversion [146], the ultimate performance remains limited by the low solid angular coverage.

Here, a novel small animal tomographic imaging approach based on scanning a SMTA is proposed. The array is rotated around the animal and further translated along the elevational direction, which guarantees sufficient angular coverage to render high-quality images on length-scales ranging from a single organ to the whole-body. By using a SMTA, real-time imaging capacity in a small area is enabled, where coregistration to the whole body image allows for improved interpretation of the real-time sequence. The resolution of the system is characterized herein and a procedure to remove motion artifacts is further suggested.

III.2.2 Materials & Methods

A similar version of the following paragraph (Subsection III.2.2) including all sub-paragraphs was originally published in [157].

III.2.2.1 Experimental Setup

Figure III.4a shows a lay-out of the proposed OT imaging system. Specifically, a SMTA was rotated around the imaged sample and perpendicularly translated along its elevational direction. The azimuthal and elevational position of the detector array can be independently controlled through two motorized stages (IAI Inc., Japan) with 15 cm and 360° range respectively. Moreover, a custom-made polyethylene holder attached to the rotation stage further enables to manually define the radial location of the array with respect to the rotation axis. For optimal US signal transmission, the imaged samples were immersed in a water tank while a computer-controlled heating stick kept the water temperature constant during each experiment. OA excitation was performed with a short-pulsed (≈ 10 ns) optical parametric oscillator based laser source (Innolas Laser GmbH, Germany) that was guided onto the sample using a custom-made fiber bundle (CeramOptec GmbH, Germany). The wavelength of the laser source can be tuned in the range of $700 - 900$ nm with a PRF of up to 100 Hz, so that an arbitrary wavelength can be set for each pulse. The outlet of the light bundle was inserted and fixed inside a cylindrical cavity in the center of the SMTA, providing a Gaussian illumination profile at the tissue surface with a FWHM of approximately 10 mm and an energy per pulse ranging between $10 - 20$ mJ

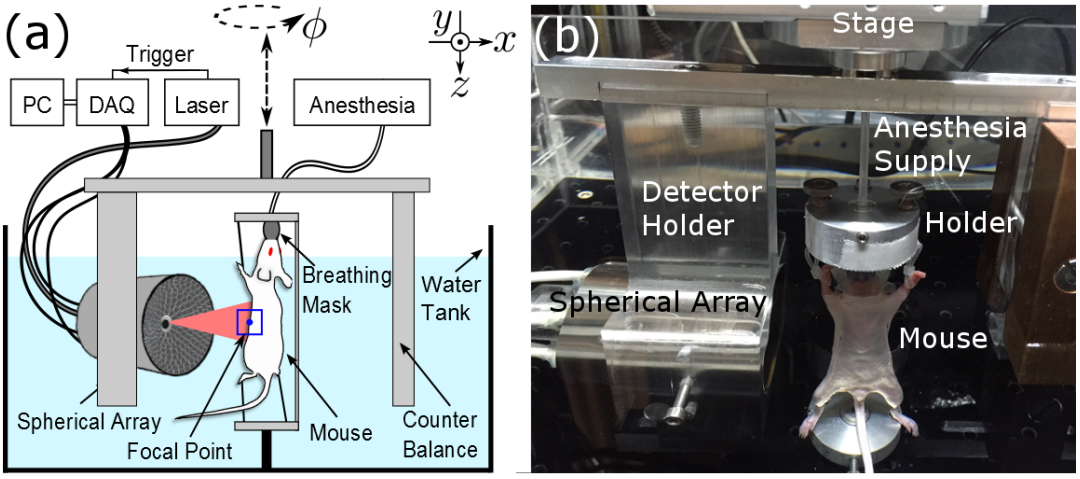

Figure III.4: Lay-out of the experimental setup. **(a)** A Cartesian coordinate system is defined. The mouse is vertically immersed in a heat-controlled water tank and subsequently raster scanned in-vivo by translating and rotating (z and ϕ, dashed arrow lines) a SMTA. During data acquisition, the mouse is anaesthetised using an isoflurane-air-mixture. OA signals are excited using nanosecond-laser pulses. The excited signals are then time-resolved by the DAQ and subsequently saved on the computer. **(b)** Photo of the experimental setup. From [157].

at the surface of the imaged sample and depending on the wavelength employed. The SMTA used in this study was described in detail previously [70]. In short, the array consists of 256 spherically-distributed piezocomposite elements where each detection element has a size of about $3 \times 3\,\mathrm{mm}^2$, a central frequency of 4 MHz and a 100% bandwidth at -6 dB. The acoustic signals were time-resolved and digitized at 40 mega samples per second using a custom-made high-speed DAQ (Falkenstein Mikrosysteme GmbH, Germany) that was triggered with the Q-switch output of the laser. For each position of the detector, multiple acquisitions from all 256 detectors were performed and subsequently saved on the computer for further post-processing. All data acquisition as well as the motor positioning was computer-controlled using MATLAB$^{\mathrm{TM}}$ (R2013a).

III.2.2.2 Phantom Experiments

In order to reconstruct high-resolution images it is important to accurately calibrate the relative position and orientation of the SMTA with respect to the rotation axis. For that, a gauge phantom consisting of a single 100 μm polyethylene microsphere (Cospheric, Santa Barbara, USA) was embedded in agar and scanned before each experiment. By considering 35 angular projections of the gauge phantom covering 360° for the same translational position, it is possible to determine the radial position, the lateral shift as well as the axial rotation of the SMTA. Hereby, the signals were averaged 150 times for every projection to increase the singal-to-noise ratio. Clearly, the axial rotation angle of the SMTA is determined when the position of the gauge sphere is confined in one plane for every projection. The radial position as well as the lateral shift can be calculated by stitching the individual frames after applying a FWHM-threshold and subsequent variation of the two parameters until the total number of voxels in the resulting reconstructed volume is minimal. Once the system was calibrated, two phantoms were imaged to characterize its resolution. The first phantom consisted of 100 μm polyethylene microspheres (Cospheric, Santa Barbara, USA) randomly scattered over a cross section of an agar cylinder

with an approximate diameter of 25 mm. The phantom was scanned along 50 projections covering 360° and 5 translational positions along the z-axis corresponding to a total distance of 2 mm. The acquired signals were averaged 100 times for each scanning position. The resolution in the radial (r) and azimuthal (ϕ) directions is expected to improve for every image position due to the increased angular coverage provided by rotating the SMTA [170, 171]. However, since translational scanning is performed along the z-direction, the resolution along this axis is expected not to increase substantially with respect to the case where only a single projection is being used for reconstruction. In order to evaluate the dependency of the spatial resolution on the radial position of the array, two different scans were performed with the focus of the spherical array positioned at distances $f_1 = 5.5$mm and $f_2 = 8.7$mm from the rotation axis. The second phantom consisted of two black surgical suture pieces with a diameter of 125 μm (Ethicon, USA) arranged to form a cross along the translational scanning axis. The focus of the detector was adjusted at $f_1 = 8.7$mm and the cross was scanned for 360° with 50 projections over a translation range of 2 cm with 2 mm step size. The acquired signals were again averaged 100 times for each position. Both phantoms were prepared by solving agar powder (1.3 g/100ml) in deionized water. Intralipid-20% (1 ml/100ml) was added to the agar solution for a better distribution of the light beam on the volume containing the absorbers. All phantom experiments were performed at 800 nm.

III.2.2.3 Mouse Experiments

The in-vivo imaging capacity of the proposed system was validated with two female athymicnude-Foxn1nu mice (Harlan Laboratories LTD, Switzerland), 6 and 7 months old respectively. Animals were imaged in full compliance with the institutional guidelines of the Helmholtz Center Munich and with approval from the Government District of Upper Bavaria under animal protocol reference number $55.2 - 1 - 54 - 2532 - 88 - 2014$. The eyes of the mice were covered with vet ointment (Bepanthen®, Bayer AG, Germany) to ensure protection from the laser light as well as preventing eye dehydration during the scanning. The focal distance was adjusted to match $f_2 = 8.7$ mm, essentially causing the SMTA to be focused approximately 5 mm underneath the skin of the mouse. During imaging, the position of the mice was fixed with a self-developed stainless steel mouse holder placed in the center of the rotational axis (Figure III.4b). The holder consists of two circular plates separated by a thin rod. The mice were held in place through four cords that were gently tied to the legs and paws to ensure proper blood circulation in the extremities. The mouth of the imaged mouse was inserted in a custom-made breathing mask connected to the top plate, ensuring that the mouse head was positioned above the water level at all time. Isoflurane anesthesia ($2 - 3$ % (by volume) with 0.9 l/min gas flow) was provided through the breathing mask during the experiment. The water temperature in the tank was set to 34° to stabilize the body temperature of the mouse during data acquisition. In a first experiment, the back region of a mouse was imaged. The scan was initiated at the neck region and covered a translational range of 5 cm with 2 mm step size. At every z position, the SMTA was rotated between $-110°$ and $+110°$ degrees with 35 equally-spaced steps, where the SMTA was focused on the spine of the mouse for 0°. For every position of the detector, a series of 50 frames was acquired. Using the same scanning parameters and starting position, the experiment was repeated by scanning the front region of the second mouse with the detector focusing on the sternum of the mouse for 0°. The total acquisition time for each of the two scans was about eight minutes.

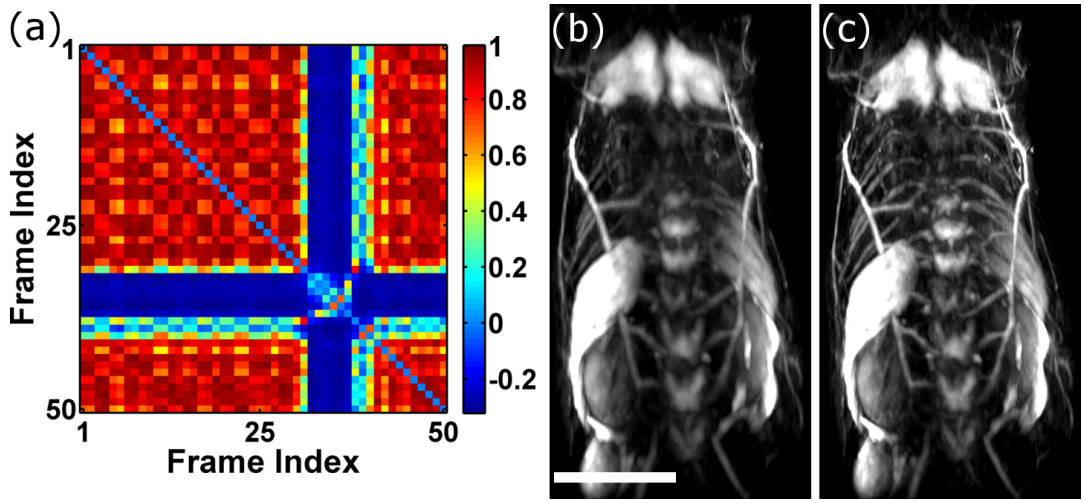

Figure III.5: (a) Plot of the correlation matrix of 50 consecutive frames acquired at a PRF of 100 Hz. Frames that are affected by respiratory motion can be identified by a small value of the correlation coefficient. In contrast, frames with no respiratory motion show high correlation. **(b)** MIP along the y-axis of a reconstructed volume of an in-vivo scan of the backside of a living mouse where all frames at a single position were averaged before stitching. **(c)** The same dataset as before but this time only non-respiratory frames were used for reconstruction. Scale bar corresponds to 1 cm. From [157].

III.2.2.4 Signal Processing & Image Reconstruction

The image reconstruction process was organized in two steps. First, volumetric images were reconstructed individually for each scanning position using a back-projection algorithm [72]. In a second processing step, all reconstructed images were stitched into the full image volume by using the position data of the SMTA and the relative position to the rotational axis as obtained with the calibration procedure. With this approach, full flexibility in terms of the reconstruction technique is being maintained. Additionally, real-time data can be projected onto an anatomical background image by using the same reconstruction procedure.

Since the proposed system is capable of delivering in-vivo data, reconstructed volumes may be affected by cardiac and respiratory motion. It was shown that the mouse body can move up to relative distances of several millimeters when under anesthesia [174]. The influence of respiration is particularly crucial and typically causes artifacts like blurring and a loss of contrast. To account for this effect, a clustering approach was employed to enhance the imaging performance of the system. The normal respiration frequency of mice is about $1-2$ Hz [174]. Hence, for a particular position, the series of 50 frames typically corresponds to less than two full breathing events and therefore not more than a total of $10-13$ frames should be affected when using a PRF of 100 Hz. It was found that these frames show low frame-to-frame correlation (Figure III.5) as compared to non-respiratory frames and by using a k-means sorting algorithm applied to the thresholded correlation matrix of the series, these frames can be identified and subsequently removed from the stack before averaging. First, all values in the correlation matrix that were higher than the threshold were set to 1 while all lower values were set to 0. The k-means algorithm was then initiated with a threshold of 0.95 and iteratively lowered until the number of non-respiratory frames per position was equal or greater than 15. An exemplary frame series acquired from a mouse heart (Movie 1) that was subsequently sorted into two bins (Movie 2 and Movie 3) can be found in the on-line version of the original publication [157].

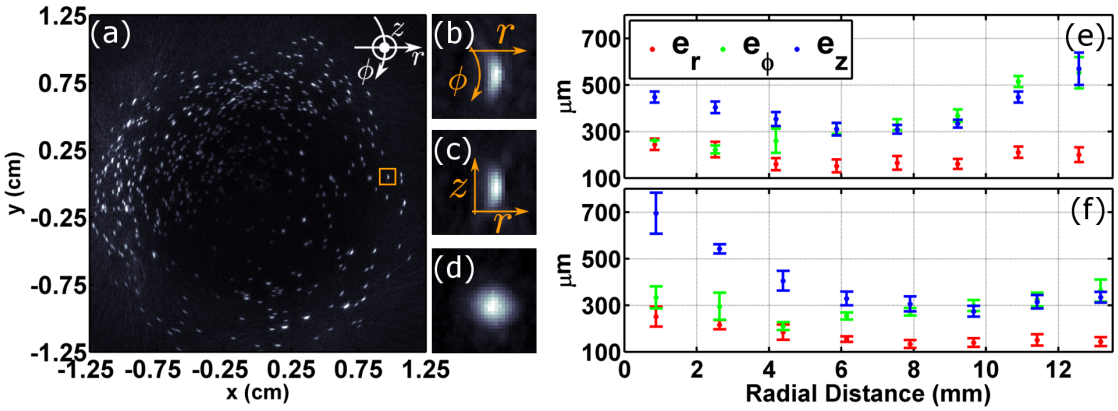

Figure III.6: Determination of the resolution within the field of view. **(a)** MIP of the reconstructed volume along the z-axis of the first phantom. The focal distance was set to $f_2 = 8.7\,\text{mm}$. A cylindrical coordinate system is specified for every sphere individually. An exemplary region of interest is defined by the orange box. **(b)-(d)** show MIPs of the volume of interest along different. The volume size was 1 mm in every dimension. **(b)** MIP along z-axis of the ROI. **(c)** MIP along y-axis. **(d)** MIP along the x-axis. (e) Radial (e_r), azimuthal (e_ϕ) and cylindrical (e_z) resolution at increasing distances r from the rotational axis. The focal distance was $f_2 = 8.7\,\text{mm}$. **(f)** Same as in **(e)** but with focal distance $f_1 = 5.5\,\text{mm}$. From [157].

In detail, the processing pipeline for reconstructing an OA image commenced by deconvolving the acquired signals with the impulse response function of the detector elements and continued by band-pass filtering such between 300 kHz and 6 MHz using a second-order Butterworth filter. For every position, the full series of volumetric pressure maps was then reconstructed on an anisotropic Cartesian grid of points centered in the focal point of the SMTA using a GPU implementation of a three-dimensional back-projection algorithm [72] and the proposed frame-sorting algorithm was applied to the stack to remove respiratory frames before the average of the series was positioned in the final reconstructed volume. After all individual frames were stitched into the final volume negative values were disregarded. For all phantom experiments, the reconstruction grid consisted of 300 voxels per centimeter while a resolution of 100 voxels per centimeter was used for all in-vivo experiments. Reconstructed data was displayed using MIP images while the dynamic range was chosen to minimize background noise. All data processing was carried out on an Intel Core$^{\text{TM}}$ i7 machine (8-core, 2.8 GHz) with 64GB memory using MATLAB$^{\text{TM}}$ (R2013a). The proposed frame sorting approach via k-means was implemented using the available MATLAB$^{\text{TM}}$(R2013a) routine whereas the back-projection code was implemented in OpenCL$^{\text{TM}}$ on an AMD Raedon$^{\text{TM}}$ HD 7900 graphics card.

III.2.3 Results

A similar version of the following paragraph (Subsection III.2.3) including all sub-paragraphs was originally published in [157].

III.2.3.1 Spatial Resolution Characterization

The results of the first phantom experiment for the two considered focal distances $f_1 = 5.5\,\text{mm}$ and $f_2 = 8.7\,\text{mm}$ are summarized in Figure III.6. Figure III.6a shows an exemplary MIP along the z-axis of the reconstructed volume where the focus of the SMTA was located at focal distance $f_2 = 8.7\,\text{mm}$ from the rotation axis. For both focal distances f_1 and f_2, the

microspheres could be reconstructed over the entire volume with lower intensity values in the central region of the phantom, which can be attributed to inhomogeneities in light fluence. Multiple spheres at different radial distances from the rotational axis were chosen and local cylindrical coordinate systems were then defined at each particle position (Figure III.6b-d) to determine the radial e_r, azimuthal e_ϕ and elevational e_z resolution of the system. For this, a FWHM threshold was applied to every reconstructed sphere individually to determine the number of pixels above this threshold in all three dimensions. The values for e_r, e_ϕ and e_z were then defined as the root square difference of the measured FWHM and the diameter of the particles to correct for the finite size of the spheres [69]. The calculated values for each resolution as a function of the radial position of the spheres for distances f_1 and f_2 are shown in Figure III.6e-f. Clearly, the radial resolution remains constant throughout the imaged volume with a value of approximately 200 μm to 300 μm independently of the two focal distances. The azimuthal resolution, e_ϕ, is also confined to these values for f_2, while it deteriorates in the periphery of the phantom for f_1. In the reconstruction for focal distance f_1, the perpendicular resolution drops from a value of about 500 μm in the center to a minimal value of 300 μm at a distance of 7 mm before it reaches a value of 550 μm at the periphery of the image volume. For the scan with focal distance f_2, e_z is determined to be around 700 μm in the center before it drops to a constant value of 300 μm at 6 mm radial distance until the end of the range. These differences are attributed to the different radial position of the transducer, which must be properly selected depending on the size of the imaged sample.

The results of the second phantom experiment are depicted in Figure III.7. In Figure III.7a, a MIP along the y-axis of the imaging volume is shown where the reconstructed volume was cropped to fit the dimensions of the cross. The shape of the suture is clear and sharp and no imaging artifacts due to the reconstruction procedure based on stitching individual volumes could be noticed. The image further allows to alternatively determine the resolution based on the ability to separate two objects. In this way, three cross sections along the z-axis of the reconstructed volume (Figure III.7b-d) were investigated in more detail. Specifically, a FWHM threshold was applied to every cross section of the two sutures individually and the total number of pixels was determined. For the cross sections displayed in Figure III.7b and d, the suture diameter determined with the FWHM criterion was approximately $266 - 333\,\mu$m, which is in agreement with the measured values for the resolution obtained with the first phantom experiment. The resolution was then alternatively measured by choosing the closest slice to the intersection where the sutures could still be identified as different objects. With this approach, the distance between the two intensity maxima, corresponding to the two sutures is associated to what is commonly known as the Sparrow resolution criterion and it was determined to be 230 μm. A 3D video of the phantom can be found in the on-line version of the original publication (Movie 4) [157].

III.2.3.2 In-Vivo Imaging of Mice

The benefits of the described frame rejection criterion are illustrated in Figure III.5. Figure III.5b shows a MIP of the reconstructed volume where all acquired 50 frames were averaged before reconstruction. The image displayed shows the back side view of the mouse with the left side of the mouse being on the left side of the image. Figure III.5c shows the same image displayed with the same orientation with the frame rejection criterion applied. It was found that the image contrast increases significantly when respiratory frames are rejected before averaging. As a result, smaller vessels with lower amplitude can still be clearly identified over the background noise. Figure III.8a-c displays the identical reconstructed volume from different angles (left

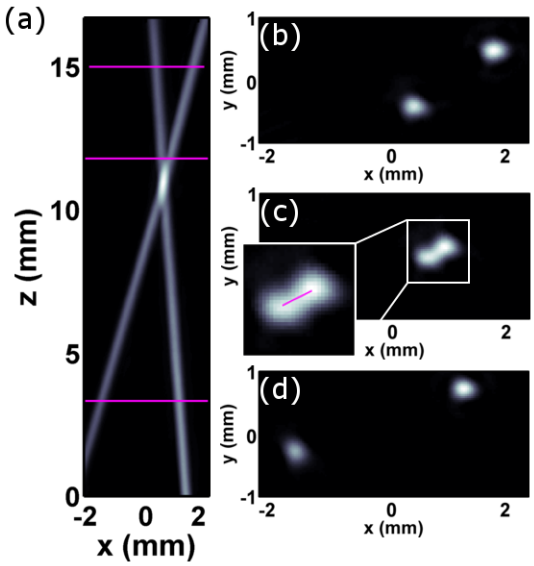

Figure III.7: Volumetric reconstruction of the suture phantom. **(a)** MIP of the reconstructed volume along the y-axis. The focal distance was set to $f_2 = 8.7\,\text{mm}$. Pink lines indicate the positions of the cross-sectional images. **(b)** Cross-sectional image corresponding to the top line in **(a)**. **(c)** Cross-sectional image corresponding to the middle line in **(a)**. Inset: magnification of white box ($1 \times 1\,\text{mm}$). Line indicates distance between the two maxima that is used to determine the Sparrow resolution. **(c)** Cross-sectional image corresponding to the bottom line in **(a)**. From [157].

backside, backside and right backside respectively) with anatomical structures indicated. Main organs like the kidney or the spleen as well as the spine and the surrounding vascular system can be clearly identified. MIPs of the reconstructed image corresponding to the second mouse are also shown in Figure III.8d-e for different angular views (front view and left side view respectively). Much like in the other mouse, organs and structures can be clearly identified. For example, the heart, liver and some thoracic vessels are clear visible. Fine vascular structures on top of some organs can also be visualized. Movies showing rotating views of the reconstructed data are available in the on-line version of the journal (Movie 5 and Movie 6) in which the research was originally published [157].

III.2.4 Discussion

A similar version of the following discussion (Subsection III.2.4) was originally published in [157]. An OT imaging approach enabling new dynamic imaging features has been described. The suggested system is based on the rotation of a SMTA around a small animal and further translation of such along the elevational direction. For each laser pulse and position of the array, a three-dimensional image covering an approximate volume of $10 \times 10 \times 10\,\text{mm}^3$ can be rendered. Then, by considering all scanning positions, the individual tomographic reconstructions can be superimposed to yield a whole-body image of the mouse, which in turn can serve as an excellent anatomical reference to corregister a real-time sequence of images acquired at a given position of the array. The performance of the suggested scanning approach for whole-body imaging is determined by the angular coverage provided by the number of measuring locations around the sample. In this regard, a spherical acquisition geometry represents arguably the most promising approach for finite-size transducers having directional sensitivity patterns [71].

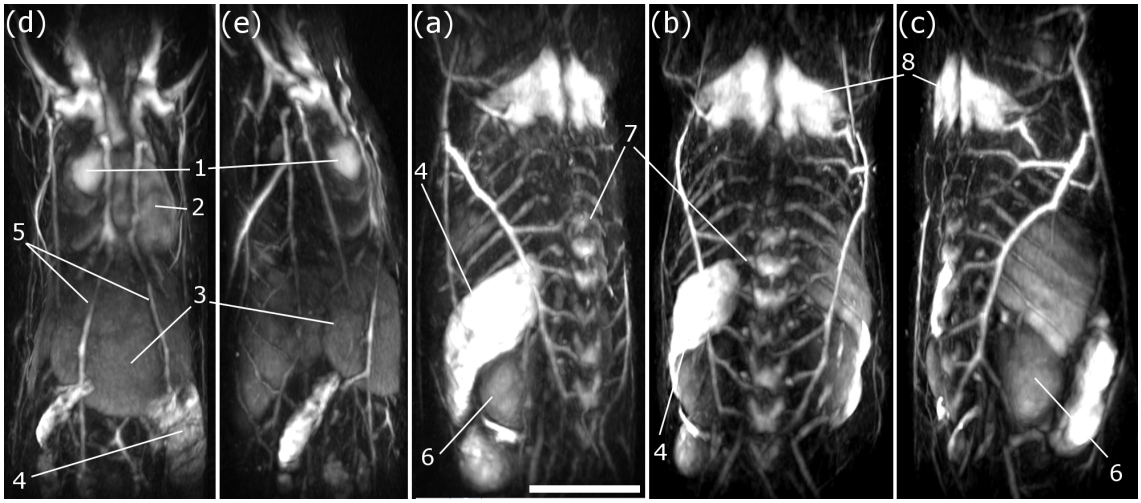

Figure III.8: MIPs of reconstructions of in-vivo body scans of mice. **(a)** front view, **(b)** left side view, **(c)** left back view, **(d)** back view, **(f)** right back view. (Legend): 1: Left Atrium, 2: Cardiac ventricles, 3: Liver, 4: Spleen, 5: Thoracic vessels, 6: Kidney, 7: Spine, 8: Shoulder muscles. Scale bar corresponds to 1 cm. From [157].

It was shown herein that blood vessels as well as other anatomical structures with different sizes and orientations could be accurately reconstructed.

The obtained results further suggest that the focal distance of the detector can be adapted to optimize the resolution and imaging performance in a given region of interest, although the larger angular coverage generally leads to an enhanced resolution with respect to that achieved for a single position of the transducer [70]. It was shown here that a frame rate of 100 Hz limited by the PRF of the laser could be achieved, which comes however at the expense of a reduced field of view determined by the number and size of the ultrasound detection elements. A small field of view can hamper the identification of anatomical structures in a real-time sequence of images. However, this can be facilitated by registering the sequence of images in the whole-body tomographic reconstruction, thus allowing a better interpretation of the results. It was further shown that the real-time imaging capability can be exploited to correct for motion-associated artifacts in in-vivo experiments images. The importance of the suggested acquisition geometry is manifested in the fact that a simple reconstruction method based on stitching individual images obtained from a back-projection formula is sufficient to yield high-quality images. Other reconstruction procedures accounting for speed of sound variations [162], acoustic scattering [175] or the effect of the size of the US detection elements [142] may further improve the image reconstruction. Model-based OA reconstruction in three dimensions with a large number of detector points is however challenging due to large memory requirements and long reconstruction times and better implementations of such algorithms must be developed for the proposed scanning system. Further hardware developments can also enhance the performance of the presented imaging approach. For example, acquisition of signals without stopping the detector for signal acquisition can lead to a reduction in acquisition time that is required for whole body imaging [69]. Alternative scanning protocols may lead to a larger field of view for whole-body imaging [87]. Additionally, the field of view for a given position can also be enlarged with a better design of the spherical array. Finally, the resolution in OT scales with the frequency bandwidth of the US transducers employed and therefore can be increased with higher frequency arrays.

IV Imaging of Multi-Scale Dynamics

This chapter is dedicated to multi-scale OA and US imaging and its application using the newly developed imaging systems that were introduced in Chapter III.

To refute any allegations concerning self-plagiarism, it shall be noted that the following chapter does not provide an original presentation of the conducted research. In fact, it merely summarizes the content of the candidate's original publications i.e. [156, 176] and [157, 177]. However, explicit reference to the original sources will be given throughout the chapter.

IV.1 Hybrid Ultrasound and Optoacoustic Imaging

In the following studies, the newly developed hybrid US and OA imaging configuration introduced in Section III.1 was utilized in typical clinical imaging scenarios. Specifically, the system was used to investigate a newly developed US and OA dual-modality contrast agent through multiple sets of phantom as well as in-vivo mouse measurements. Moreover, the proposed configuration was used to image the finger of a healthy human volunteer.

IV.1.1 Imaging of Dual-Modality Microbubbles

In Subsection II.1.4, the concept of contrast agent based OA imaging was already introduced and the significance for biomedical imaging was discussed. Highly absorbing dyes or nanoparticles targeted to molecules or cells can be utilized for cancer cell detection or drug delivery studies [119]. The concept of agent-based imaging is becoming more and more important and there is an increasing effort dedicated to the development of novel agents specifically designed for non-optical imaging modalities such as X-Ray Tomography (CT) [178] or Magnetic Resonance Imaging (MRI) [179]. In medical US, microbubble contrast agents have significantly enhanced imaging capabilities, thus allowing for better diagnosis as well as drug and gene delivery studies, therefore becoming an integral part of US examinations [180]. Besides the development of novel contrast agents, there is an emerging trend of combining existing contrast agents to form dual- or even triple modality agents [181, 182]. In this study, a newly developed US and OA dual-modality contrast agent, based on conjugating a dye to microbubbles, was investigated.

IV.1.1.1 Materials & Methods

First, the fluorescent labelled microbubble solutions were synthesized. The fluorescent dye was attached to the surface of the lipid based microbubbles through the primary amines of the lipid and the carboxy group of the dye, following to the formation of a stable conjugate through an

amide bond. Specifically, a lipid stock solution containing DPPC (1,2-Dipalmitoyl-sn-Glycero-3-Phosphocholine) and DSPE-PEG2000-amine [1,2-distearoyl-sn-glycero-3-phosphoethanolamine-N-[amino(polyethylene glycol)-2000] (ammonium salt)] (Avanti Polar Lipids, USA) in a 95:5 molar ratio was prepared employing the thin film hydration method and subsequently resuspended in 0.1M sodium borate puffer at pH 8.5 at a total lipid concentration of 10 mg/mL. The lipid stock was sonicated with a Sonorex Digitec (Bandelin Electronics, Germany) at a frequency of 35 kHz to obtain a clear stock solution. For fluorescent labelling of the lipids, AT700 (peak absorption at 700 nm, Atto-Tec GmbH, Germany) was dissolved in DMSO before it was added to the lipid solution. The sample was then kept at 4° overnight. The molar ratio of the dye to amine was 2.1 : 1. After the conjugation, the fluorescent labelled lipids were dialysed in water using a Dialysis cassette (Slide-A-Lyzer Dialysis Cassettes, Thermo Fisher Scientific, USA). For the preparation of fluorescent labelled microbubbles, a 1 mg labelled lipid stock solution was used in a 2 mL clear glass vial (SUPELCO, USA) and the volume was adjusted to 1 mL with 0.9% NaCl:glycerol:propylene glycol at volume ratios of 8:1:1. The headspace of the vial was filled with perfluoropropane gas (Linde AG, Germany), and the vial was agitated using a CapMixTM capsule mixing device (3M ESPE AG, Germany) at 4650 rpm for 60 seconds. The procedure was repeated to synthesize another solution of fluorescent labelled microbubbles using Alexa Fluor 750 (AF750) (peak absorption at 750 nm, Thermo Fisher Scientific, USA).

The microbubble solutions were then investigated by performing multiple phantom experiments as well as an in-vivo study in a mouse. In the first phantom experiment, a polyethylene tube filled with air was arrangement to form a cross and placed in the focal region of the SMTA. Acoustic coupling was enabled by placing the whole setup inside a water tank where the temperature was kept constant at 23° using a computer-controlled heating stick. A solution of the 730 nm-microbubbles was injected into the tube until one half of the cross was completely filled while the other still contained air. The laser was set to 700 nm and a series of frames were acquired at a PRF of 50 Hz. The experiment was then repeated using the 750 nm-microbubbles. Both tubes were completely filled and the an excitation wavelengths of 750 nm was chosen. In the third experiment, the tube was filled with 700 nm-microbubbles and a sonication device (Sonitron 2000D, Rich Mar Inc., USA).) emitting shock-waves was placed on the intersection of the two tubes for 30 seconds to destroy the microbubbles. By this approach, it was assured that the concentration of the dye remains constant and the impact of the structure of the microbubbles on the OA signal strength can be investigated. Finally, a 100 μl solution of the 700 nm-microbubbles was injected into the tail of a 6 months old female athymic nude-Foxn1nu mouse (Harlan Laboratories LTD, Switzerland). The mouse was imaged in full compliance with the institutional guidelines of the Helmholtz Center Munich and with approval from the Government District of Upper Bavaria. The eyes were covered with vet ointment (Bepanthen®, Bayer AG, Germany) to ensure protection from the laser light as well as to prevent eye dehydration during the scanning. The body temperature of the mouse was kept constant during the experiment using a heating pad (PhysioSuite, Kent Scientific, USA). Isoflurane anesthesia ($2-3$ % (by volume)) with 0.9 l/min gas flow was provided through a custom-made breathing mask. The focus of the SMTA was positioned on the heart of the mouse using real-time image reconstruction guidance before the microbubble solution was injected and acquisition was initiated at 50 Hz while the excitation wavelengths was set to match the peak absorbance of the microbubbles. Image processing and reconstruction was carried out as it was described in Section III.1 and signals were averaged 50 times for every frame to increase the signal-to-noise ratio.

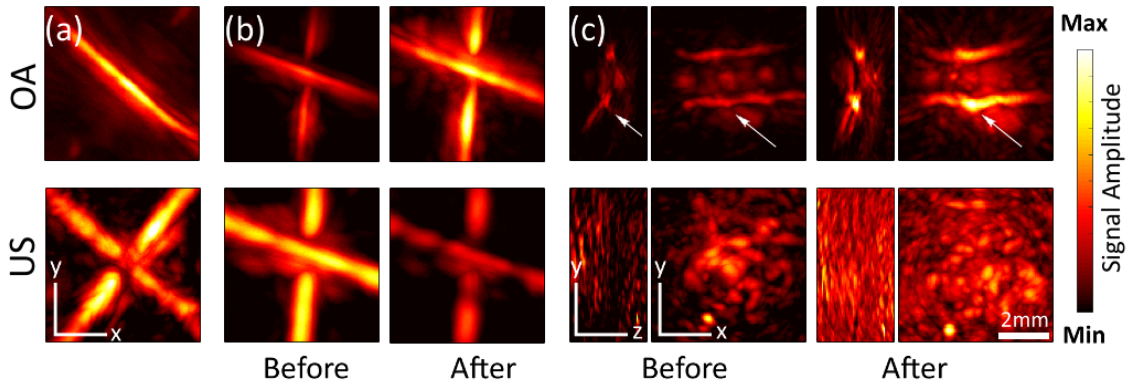

Figure IV.1: Contrast validation of the dual-modality microbubbles in phantom and in-vivo experiments. **(a)** MIPs along the depth-direction of the reconstructed US and OA image. In the OA image, only the tube filled with the contrast agent is visible while both tubes are clearly visible in the US image. Image values were normalized to the corresponding maximum value. **(b)** MIPs along the depth-direction of the US and OA volumes before and after sonication. For comparison, each image was normalized to the global maximum of the corresponding channel. The contrast of the US channel deteriorates as the microbubbles were destroyed while the contrast of the OA channel increases. **(c)** MIPs along the lateral and the axial direction of the US and OA volumes. In both channels, the dual-microbubbles clearly increase the contrast. Arrow: thoracic vessel of the mouse heart.

IV.1.1.2 Results & Discussion

Figure IV.1a shows MIP images of the reconstructed volumes along the depth direction for the recorded US and OA signals of the first experiment. In both images, the amplitude values were normalized to the corresponding maximum. Both tubes are clearly visible in the US while only the tube filled with microbubbles is visible in the OA image. The signal strength in the tube filled with microbubbles almost reaches the signal strength of the tube filled with air, indicating the excellent amplification property of this contrast agent. The results of the second experiment are displayed in Figure IV.1b. MIPs of the reconstructed volumes along the z-direction before and after sonication are shown. In order to better visualize the effect of the microbubbles on the OA and US contrast, the image values for both modalities were normalized to the corresponding global maximum of the two images. As expected, the signal contrast drops in the US channel as the bubbles get destroyed and the remaining contrast stems from acoustic mismatch between the tube wall and the water. However, the signal-to-noise ratio clearly improves in the OA image after sonication indicating that intact microbubbles decrease the OA signal amplitude. The impact of microbubbles on the OA contrast was studied before. It was found that microbubbles coated with gold nanoparticles can enhance the OA signal [181] while microbubbles in a solution of methylene blue were found to decrease OA contrast [183]. Even though the dye was attached to the microbubble through conjugation for the agent used in this study, no signal increase could be measured, thus suggesting that the mechanism of amplification is complex and probably stems from the nature between the binding of microbubbles and the OA contrast agent. Figure IV.1c shows MIP images along the lateral and axial direction of the reconstructed US and OA volumes (axial direction is perpendicular to the sternum of the mouse). The two characteristic thoracic vessels can be clearly identified on top of the heart (white arrow in Figure IV.1c). The US image mainly reveals larger structures with strong acoustic mismatch, such as the skin on top of the thoracic vessels as well as the

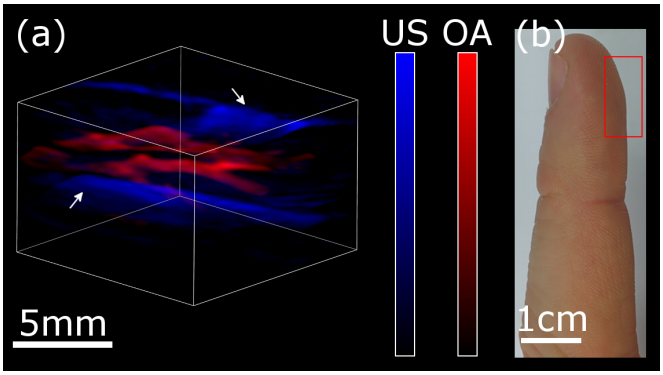

Figure IV.2: Hybrid imaging of finger in a healthy volunteer. **(a)** Three dimensional views of the OA and US reconstructions are displayed in red and blue respectively. The US image allows visualizing the location of the skin and the bone surface (labelled by white arrows) while OA signals mainly convey contrast of the blood vessels. The imaged region in the finger is shown in **(b)**. Image and caption from [156].

heart chambers underneath. For both modalities, the signal contrast clearly increases after the injection, thus validating the contrast amplification property of the microbubbles in the mouse model.

IV.1.2 Human Finger Imaging

The following study (Subsection IV.1.2) was originally published in [156]. In this study, the ability of the hybrid imaging configuration to image human tissue was validated by imaging the tip of a finger of a healthy volunteer. A three dimensional representation of the reconstructed volume of the hybrid contrast is shown in Figure IV.2. Since US contrast is predominantly based on acoustic mismatch, the features in the image mainly relate to the acoustic back-scattering at the surface of the skin and the bone (blue color in Figure IV.2a). The OA data, in contrast, is based on optical absorption and therefore mainly shows blood vessels located between the skin and the bone (red color). The increase in structural contrast provided by superimposing the OA image on top of the US image clearly improves the diagnostic value and assists in localizing and interpreting the blood contrast. Moreover, the position of acoustically hard structures, such as the skin or bones can be utilized as a-priori information to correct for speed-of-sound variations or acoustic scattering, thus helping to improve the OA reconstruction [125, 164].

IV.2 Ultrasound & Optoacoustic Imaging Feedback in Endovenous Laser Therapy

In this study, the developed hybrid US and OA imaging configuration introduced in Section III.1 was utilized to monitor lesion progression during Endovenous Laser Therapy (ELT) in real-time using the OA channel while US was used to determine the position of the tip of the laser catheter. Parts of the research were originally published in [176].

IV.2.1 Introduction

A similar version of the following introduction (Subsection IV.2.1) was originally published in [176]. ELT is a comparatively new approach to treat incompetent veins with first clinical results published about 15 years ago by Boné [184] and Navarro [185]. In ELT, a flexible laser catheter is inserted into the lumen of the incompetent truncal vein via a sheath system before laser light is continuously delivered to the vessel wall. The light energy is absorbed by the vessel and transformed into heat, which causes cell destruction and collagen shrinkage and ultimately occlusion of the treated vein segment. Typical wavelengths used in the clinical settings are all in the near infra-red (e.g. 810 nm, 940 nm, 980 nm, 1064 nm, 1320 nm or 1470 nm) [186, 187]. The laser fibers are often shaped at the outlet to achieve radial energy delivery, which is important to enable uniform coagulation across the entire cross-section of the vein [187, 188].

In a typical clinical scenario, the diameter of the incompetent vein, e.g. the vena saphena magna, will be approximately determined using conventional US to yield an estimate for the appropriate laser energy density applied during ELT. In the next step, the vein is punctured in the proximity of the distal insufficiency and the sheath is inserted before the laser fiber is positioned at the sapheno–femoral junction under US guidance. Alternatively, a pilot laser beam can be exploited to determine the location of the fiber tip by tracking the diffuse light pattern at the skin surface. Before the actual ablation is initiated, perivenous tumescence anesthesia is performed, i.e. large volumes of a dilute anesthetic solution are delivered to the vein segment, which protects the perivenous tissue from thermal damage and reduces the lumen of the truncal vein by compression and spasm. After the vein was anesthetized, laser energy is continuously delivered into the vessel until the proteins in the vessel wall are completely denaturized and blood no longer can pass through the occluded vein. For the duration of the treatment, and especially during catheter pullback, US imaging is performed to validate proper catheter positioning and to monitor lesion progression.

Treatment success crucially depends on appropriate energy deposition during ELT. Clinical data suggest that failures of ELT in the form of non-occlusion or recanalization are less frequent when sufficiently high energy levels are used [189–192]. On the other hand, inappropriately high energy densities can also lead to side effects, such as transmural ablation, perforations and alteration of perivenous tissue [193, 194]. Therefore, attempts have been made to relate the induced tissue damage to the optical energy applied using suitable parameters that characterize the specific treatment protocol employed. By using such parameters, it is possible to relate clinical results with definitive types of ablation protocols and therefore predict and compare clinical cases. One frequently used parameter, is the Linear Endovenous Energy Density (LEED) and it represents the energy delivered over a given length of the treated vein segment (in Joule/cm) [195]. Obviously, this does not consider the irradiated inner vein diameter. Therefore, the laser energy applied to the entire treated surface, i.e. the Endovenous Fluence Equivalent (EFE) (measured in Joule/cm^2) is often considered instead of the LEED [195]. Specifically, the EFE models the vein segment as a cylinder where the inner surface area is given

by $F = 2\,r\,\pi\,l$, where r and l are the inner radius and the length of the treated vein segment. Additional parameters that are documented for every treatment are the laser wavelength λ and power P in Watts, irradiation time t and the pull-back speed v of the laser catheter.

However, clinical outcomes among different ELT patients [196] are often still not satisfactory and the development of novel monitoring procedures, capable of delivering reliable information on lesion progression and the temperature profiles across the entire treated region are required. Currently, the most frequently employed online treatment monitoring technology is conventional or duplex US [192, 197]. Even though US does not provide temperature sensitive contrast, it can reveal crucial information such as the position of the fiber tip, the position and the size of the vessel. In some cases it can even provide indirect indications of heat-related effects in the treated tissue, e.g. via bubble formation and shrinkage of the lumen of the vessels.

However, an ideal imaging technology for reliable monitoring of ELT procedures should be able to provide non-invasive high resolution images with an intrinsic contrast for thermally-induced tissue changes. OA imaging ideally matches these demanding requirements as it has demonstrated high spatial resolution imaging in deep scattering tissue at frame rates of up to 50 volumes per second [28, 174]. Furthermore, it was shown that the amplitude of the OA signal has a strong temperature dependence because of the Grüneisen parameter [198, 199], thus principally showing promise for non-invasive thermometry applications. In this study, the feasibility of volumetric OA monitoring of lesion progression during ELT of subcutaneous veins in an ex vivo ox foot model is investigated.

IV.2.2 Materials & Methods

A similar version of the following paragraph (Subsection IV.2.2) including all sub-paragraphs was originally published in [176].

IV.2.2.1 Experimental Setup

A sketch of the experimental setup is shown in Figure IV.3. Ox foots are a well-established ex vivo model for ELT experiments [194, 200]. The model consists of an ox foot obtained from freshly slaughtered animals (18-24 months of age, weight $550 - 650$ kg, right hind leg). In particular, the subcutaneous veins (V. saphena lateralis and V. digitalis dorsalis communis III, $20 - 25$ cm in length, $5 - 8$ mm in diameter) are ideally suited for ex vivo experiments due to their large vessel diameter, thus allowing insertion of the endoluminal application system. First, the vein is surgically prepared before a 360° radial fiber (Biolitec GmbH, Germany) (Figure IV.3) was inserted via an introduction sheath. Treatment was then performed by means of endoluminal laser irradiation with light guided from the central end (joint) to the peripheral end (hoof). Due to the shape of the tip of the fiber, the light was delivered radially towards the vessel walls, as shown in the zoom-in window in Figure IV.3. Laser ablation was performed using a diode laser (CERALAS D15, CeramOptec GmbH, Germany) emitting light at a wavelength of $\lambda = 1470\,\text{nm}$, which is guided via a $600\,\mu\text{m}$ laser fibre. The output power of the ablation laser can be adjusted in the range of $3 - 15$ W with the corresponding LEED varying between $30 - 150$ J/cm. The sheath and catheter systems used in this study permitted perfusion of fluids (e.g. blood, saline) and the vein was irrigated during the experiment using heparinised blood to simulate blood flow. The pullback velocity was manually adjusted to about $3 - 5$ mm/s. For online monitoring of the ELT procedure, the hybrid system introduced in Section III.1 was placed on top of the ox foot above the target area (Figure IV.3). A pulsed laser source (≈ 8 nanosecond), whose wavelength can be tuned in range of $690 - 950$ nm with peak pulse energy

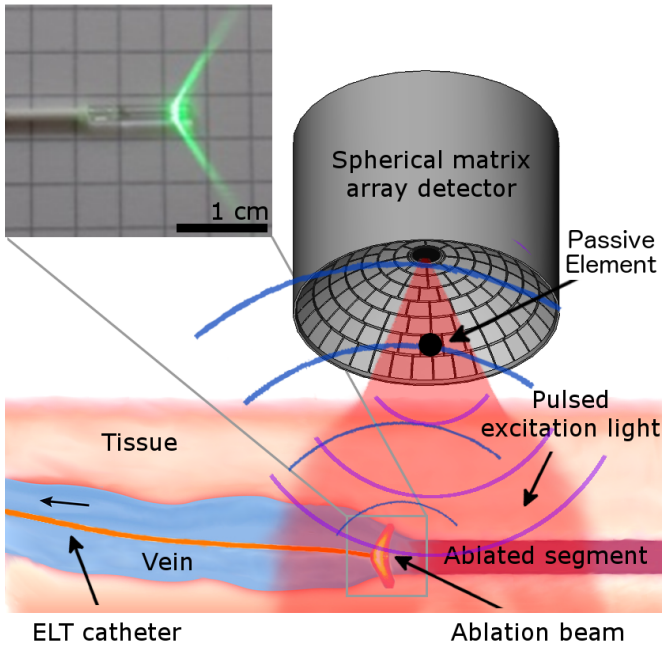

Figure IV.3: Sketch of the experimental design. An ELT catheter is inserted into a subcutaneous vein of an ox leg. Laser ablation is initiated while slowly pulling back the catheter. The procedure is monitored in real-time by exciting OA pressure signals (blue waves) with a nanosecond-pulsed near-infrared laser from the treated region. Additionally, a passive element placed coaxially between the detector and the laser beam emits US waves (purple waves). The induced OA and back-scattered US responses are subsequently recorded using a SMTA that is placed above the ablation area. Inlay: snapshot of the ELT catheter used in this study. From [176].

of 30 mJ and a PRF of up to 100 Hz was used for the excitation of the OA and US signals.

IV.2.2.2 Online Monitoring Experiments

For this study, four experiments were performed in order to investigate the applicability of hybrid US and OA imaging for monitoring of ELT. First, the ELT catheter was inserted in the vein and subsequently positioned in the focal area of the SMTA under US guidance. As mentioned in Subsection IV.2.1, identification and accurate positioning of the fiber tip is key for treatment success and so far, conventional US is utilized in the clinical practice [192, 197]. After the ELT catheter was positioned, the laser light was delivered into the vein for 20 seconds at a power of 6 W, while the excited pressure signals were continuously recorded using an illumination wavelength of $\lambda = 700\,\text{nm}$ and a PRF of 5 Hz. During the experiment, blood was flushed manually through the vein using a syringe to simulate a realistic clinical environment. The temperature was measured at the tissue surface using a digital thermocouple probe (Physiotemp, USA) placed in the proximity of the ablation region. After the laser ablation procedure was finished, the catheter was removed and blood was injected into the treated vein under OA monitoring to verify vessel sealing. Eventually, the ex vivo ELT monitoring experiment was repeated but this time, the fiber was pulled back slowly at a speed of about $3-5$ mm/s, which is typical for clinical treatment scenarios. During pull-back, blood was flushed manually through the vein using a syringe and OA images of the treated area were continuously acquired with the imaging probe remaining stationary on top of the ox foot.

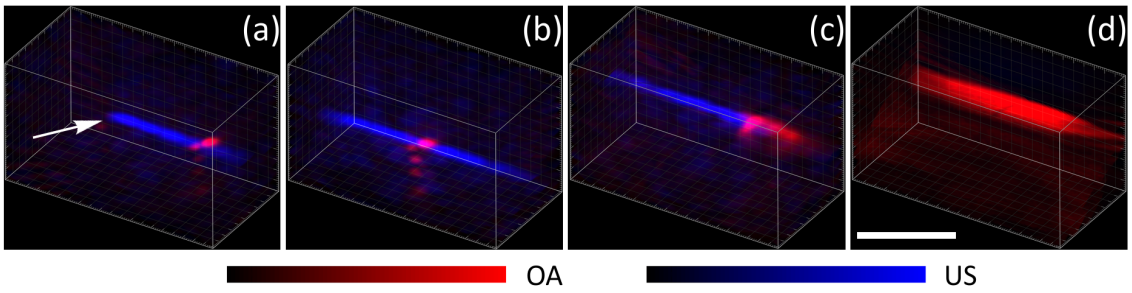

Figure IV.4: Real-time positioning of the laser tip under US guidance. A superimposed MIP image series of the reconstructed US (blue) and OA (red) data at different time instances is shown **(a-d)** while the catheter was pushed through the vein from right to left. In **(a)**, the catheter tip is clearly visible (white arrow) in the US channel while it remains invisible in the OA channel. However, a highly absorbing dot on the catheter surface is visible. **(c)** The top part of the fiber tip is still visible while the flexible fiber tube appears in the field of view (red). **(d)** The fiber tip is out of view and only the fiber tube is visible in the OA channel. Scale bar: 5 millimeter.

IV.2.3 Results

A similar version of the following paragraph (Subsection IV.2.3) including all sub-paragraphs was originally published in [176]

IV.2.3.1 Catheter Positioning

Figure IV.4 shows a series of MIP images of the reconstructed US signals while pushing the catheter through the ox vein from right to left. The GPU implementation of the US reconstruction algorithm enables to reconstruct image volumes on the fly, thus further allowing for proper positioning of the laser tip before the treatment - a powerful capability during clinical procedures. The image series clearly demonstrates the advantage of the proposed hybrid imaging approach. The tip of the laser catheter is transparent (Figure IV.3) and thus invisible in the OA channel. However, the acoustic mismatch of the catheter with respect to the surrounding tissue is strong and its position can be clearly tracked in the reconstructed US volumes.

IV.2.3.2 Stationary ELT Monitoring Experiments

In Figure IV.5A, a time series of OA MIP images that were taken during the stationary ELT procedure are displayed. The top row shows MIP images along the axial direction, while the bottom row shows the same dataset along the lateral direction. The morphology of the vein can be clearly identified before laser treatment is initiated (Figure IV.5A, $t_0 = 4$ s). The depth contrast, is limited due to strong light absorption by the blood inside in the vessel. All components used in this experiment, including the ELT catheter, the imaging probe, and the thermal probe remained stationary during the experiment. After laser ablation treatment commenced, the vessel was progressively destroyed and all vessel structures around the coagulation area completely diminished, approximately 50 seconds after the procedure was initiated. The entire image sequence of the experiment is available in the online version of the journal, where the data was originally published (Video 1) [176].

To investigate the changes in OA contrast during the ablation procedure, the time trace of the average voxel intensity inside the two colored boxes (blue and pink) was plotted. The pink box (Figure IV.5A) is localized right on top of the ablation spot and changes in its average

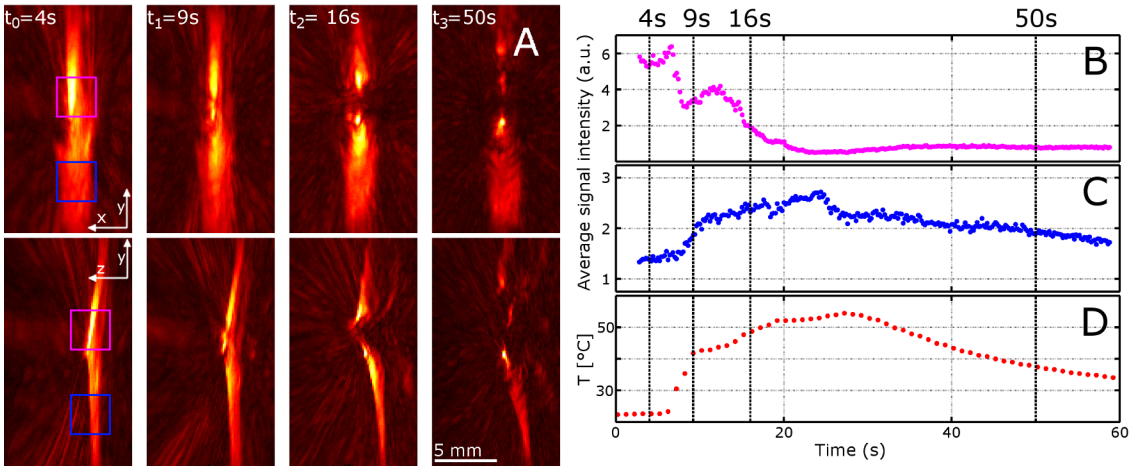

Figure IV.5: Real-time OA monitoring of stationary vein ablation. **(A)** Axial (top) and lateral (bottom) MIP images of reconstructed OA volumes at different time instances during the procedure. The catheter was inserted from the top and was positioned in the focal region of the SMTA. **(B)** and **(C)**: Time traces of the average pixel intensity value inside the pink and blue boxes, as labeled in **(A)**; **(D)** Temperature profile measured by the thermal probe that was placed in the vicinity of the treated area. From [176].

signal intensity therefore correspond to structural alterations as well as changes in the chemical composition of the vein (Figure IV.5B) due to changes in the optical absorption coefficient. During the ablation procedure, the vein and blood are removed. Consequently, the OA signal intensity in that region drops by approximately 50% only a few seconds after ablation onset. As coagulation proceeds, the signal intensity reduces to below 10% from the baseline intensity within the next 20 seconds. The blue box, contains a a part of the vein, which is outside the ablated region. This vessel segment therefore does not undergo any structural changes during the laser procedure. Thus, any alterations in the average signal intensity can be attributed to changes in the local temperature. The corresponding time trace is plotted in Figure IV.5C. The curve shows over two-fold increase in the average OA signal intensity within the first 20 seconds of heating and it correlates well with the actual temperature trace measured by the thermal probe (Figure IV.5D). The latter result greatly confirms the previously measured (almost) linear dependence of the OA signal amplitude on temperature [198].

After conclusion of the laser ablation treatment, successful vessel sealing was verified by slowly injecting blood under OA monitoring. Figure IV.6a-c show lateral OA MIP images as well as two cross-sectional OA images of the treated vein before blood is injected. Figure IV.6d-f show the same vessel while blood was inject into the vein by gently pressing the syringe. Although the shape of the vessel in the cross-sectional OA images is not circular, which can be attributed to the limited tomographic view [201] of the SMTA [70], further clinically relevant details, such as diameter of the vessel wall (Figure IV.6e) can still be derived from these images.

IV.2.3.3 Monitoring During Pullback

In this experiment, OA monitoring was performed under realistic clinical ELT conditions. During laser ablation, the catheter was slowly pulled back at a speed of about $3-5$ mm/s. Figure IV.7 shows MIP images along the axial and lateral directions of the reconstructed 3D volumes at different time instances. The position of the ablation can be clearly tracked during pull-back by observing morphological changes of the surrounding vein in real time (see

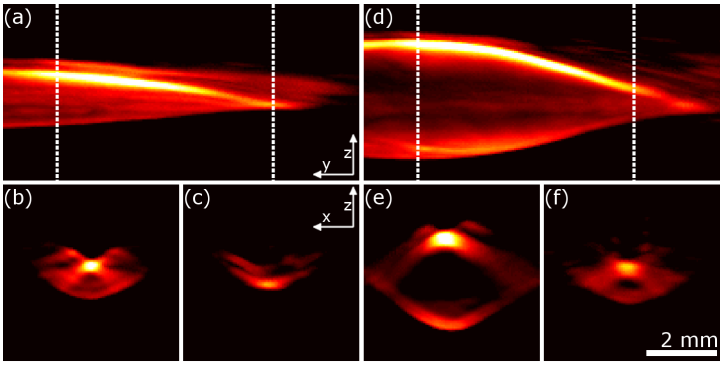

Figure IV.6: Validation of vessel sealing. **(a)** Lateral OA MIP image of the treated vein before blood injection. The cross-sectional images of the untreated **(b)** and treated **(c)** vessel segment show only minor morphological differences. **(d)-(f)** The corresponding images of the identical vein while blood is being injected. Clearly, the vessel extension is reduced in the treated segment, indicating successful vessel sealing. From [176].

arrows in Figure IV.7). As the laser catheter is pulled back, the freed space inside the vessel is continuously fills up with blood, which makes the deeper part of the vein invisible due to strong light absorption of the blood. A video of the presented image series is available in the online version of the journal in which the results were originally published (Video 2) [176].

IV.2.4 Discussion

A similar version of the following discussion (Subsection IV.2.4) was originally published in [176]. In this study, the applicability of three-dimensional hybrid US and OA tomography for real-time catheter positioning and lesion progression monitoring during ELT procedures was investigated. The performed laser ablation experiments of subcutaneous veins using an ex vivo ox foot model, showed great promise for a potential clinical application by delivering three-dimensional images of the treated vein segment in real-time and at a spatial resolution of about 200 μm. Furthermore, the suggested hybrid approach allowed for accurate positioning the tip of the laser catheter using the US channel. By using the OA modality, it was possible to recover volumetric images of the lesion progression as well as characteristics of the vessel wall at high spatio-temporal resolution. Furthermore, it was shown that the temporal dynamic of the OA signal intensity well resembles the actual temperature elevation as it was measured in an intact vein segment in close proximity to the ablation spot using a thermal probe. The promising results achieved with the proposed approach suggest that OA imaging may significantly contribute in regulating the applied thermal energy during the ablation procedure, thus allowing for consistent clinical outcomes due to a more sustainable occlusion of the treated vein segment. Moreover, the findings hold promise for non-invasive real-time temperature monitoring of the tissue surrounding the incompetent vein, which would greatly contribute in reducing the frequency of common side effects, such as overheating of the perivascular tissue and collateral damage. It is further anticipated that additional parameters which are not yet determined during ELT procedures in the clinical practice, such as vessel shrinkage due to thickening, loss of flexibility and change in color [202] could be potentially characterized using three-dimensional OA tomography, which can further reduce the probability of side effects. However, further effort has to be directed towards evaluating the actual clinical value of the proposed approach in terms of the probability increase for long-term treatment success as compared to conventional techniques. Also, the

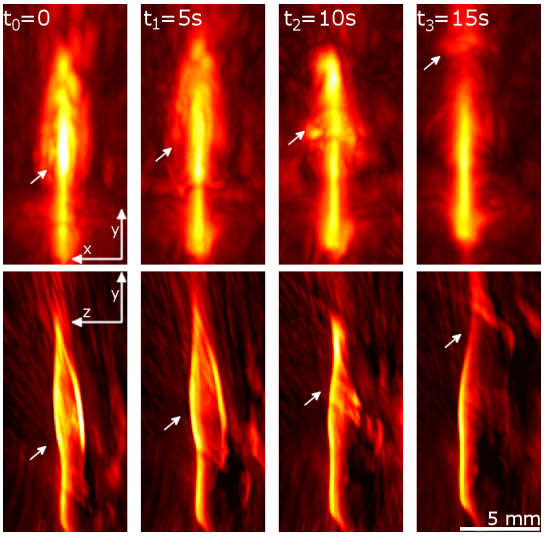

Figure IV.7: Real-time OA monitoring during laser ablation with pullback. Axial (top) and lateral (bottom) MIP images of reconstructed OA signals at different time instances during the ablation process. The catheter was inserted from the top and was subsequently positioned in the focal region of the SMTA before the ablation was initiated. The position of the tip of the ELT catheter can be clearly tracked during pull-back by inspecting alterations in the vessel morphology along the lateral direction (white arrows). From [176].

current system is not ideally suited for the clinical practice and future designs must integrate all system components in a compact hand-held design. It is expected that further improvements in hardware components and software processing will lead to additional performance gains in terms of image quality and quantification abilities. For instance, the illumination beam for OA imaging may be delivered directly by the fiber guiding the ablation beam, so that OA signals can be excited deep inside the tissue. In this case, the imaging depth is only limited by acoustic attenuation, which is much lower than optical attenuation in biological tissues in the near-infrared [33].

IV.3 Optoacoustic Imaging of Hemodynamics in the Mouse Brain

In this study, the real-time capacity of the SMTA, which was also exploited in the whole-body imaging system was utilized to non-invasively resolve fast hemodynamic changes in the mouse brain. In a first set of experiments, mice were subjected to changes in oxygenation stress and it is demonstrated that multiple hemodynamic parameters, such as Blood Oxygenation (SO_2), Total Hemoglobin (HbT), Cerebral Blood Volume (CBV), Oxygenized Hemoglobin (HbO) and Deoxygenized Hemoglobin (HbR) can be extracted in real time. In a second set of experiments, the developed framework was utilized for whole-brain mapping of the spatio-temporal dynamic of epileptic seizures. The presented research was originally published in [94] and [101].

IV.3.1 Real-Time Visualization of Cerebral Hemodynamic Parameters

A similar version of the following introduction (Subsection IV.3.1) was originally published in [101]. It is generally assumed that spatio-temporal changes of cerebral hemodynamic parameters closely resembles neuronal activity by neurovascular coupling [203] and neuroimaging techniques, such as MRI, which are capable of determining the concentration of HbO, HbR, CBV or Cerebral Blood Flow (CBF) have contributed greatly to a better understanding of the underlying mechanisms of this interaction [204, 205]. However, current neuroimaging methods are either not capable of simultaneously determine the aforementioned parameters or the achieved spatio-temporal resolution is not sufficient for a detailed investigation [205, 206]. The current gold standard in functional neuroimaging, Blood-Oxygen-Level Dependent (BOLD) functional MRI, is capable of measuring the brain's anatomy and its functional behavior. However, the spatial and temporal resolution achieved, when measuring cerebral micro-vasculature, is still insufficient for detailed investigations of neurovascular responses [203, 207], while further limitations arise from the underlying contrast mechanism that solely stems from changes in HbR. Other available clinical imaging techniques, such as Positron Emission Tomography (PET) or CT, require the application of exogenous contrast agents and exposure to ionizing radiation is unavoidable. Recently, functional neuroimaging of stimulus-evoked brain activation in the somatosensory cortex of a rat with high spatio-temporal resolution was demonstrated using US imaging [122]. However, the achieved sensitivity was limited to CBV and CBF and the proposed approach demands the opening of a cranial window in the skull of the rat. On the other hand, the unique advantages of optical imaging techniques, such as their capability to separately resolve HbO and HbR, are increasingly exploited in functional brain imaging studies. However, most of the available modalities, such as near-infrared spectroscopy, diffuse optical tomography or microscopy suffer from poor spatial resolution, are highly limited in depth due to light scattering or demand invasive procedures. OA imaging, in contrast, has recently demonstrated exceptional performance in functional neuro-imaging in rodents [207]. Nevertheless, the previously proposed approaches suffer from major limitations such as, invasiveness [207], superficial penetration depth [95] and lack of volumetric resolution in real time [131]. In this study, MS volumetric OA tomography is exploited to non-invasively resolve hemodynamic changes in the mouse brain in real-time.

IV.3.1.1 Materials & Methods

A similar version of the following paragraph (subsubsection IV.3.1.1) was originally published in [101]. Eight-week-old Female athymic nude-Foxn1nu mice (Harlan Laboratories LTD, Switzerland) were used for imaging, in full compliance with the institutional guidelines of

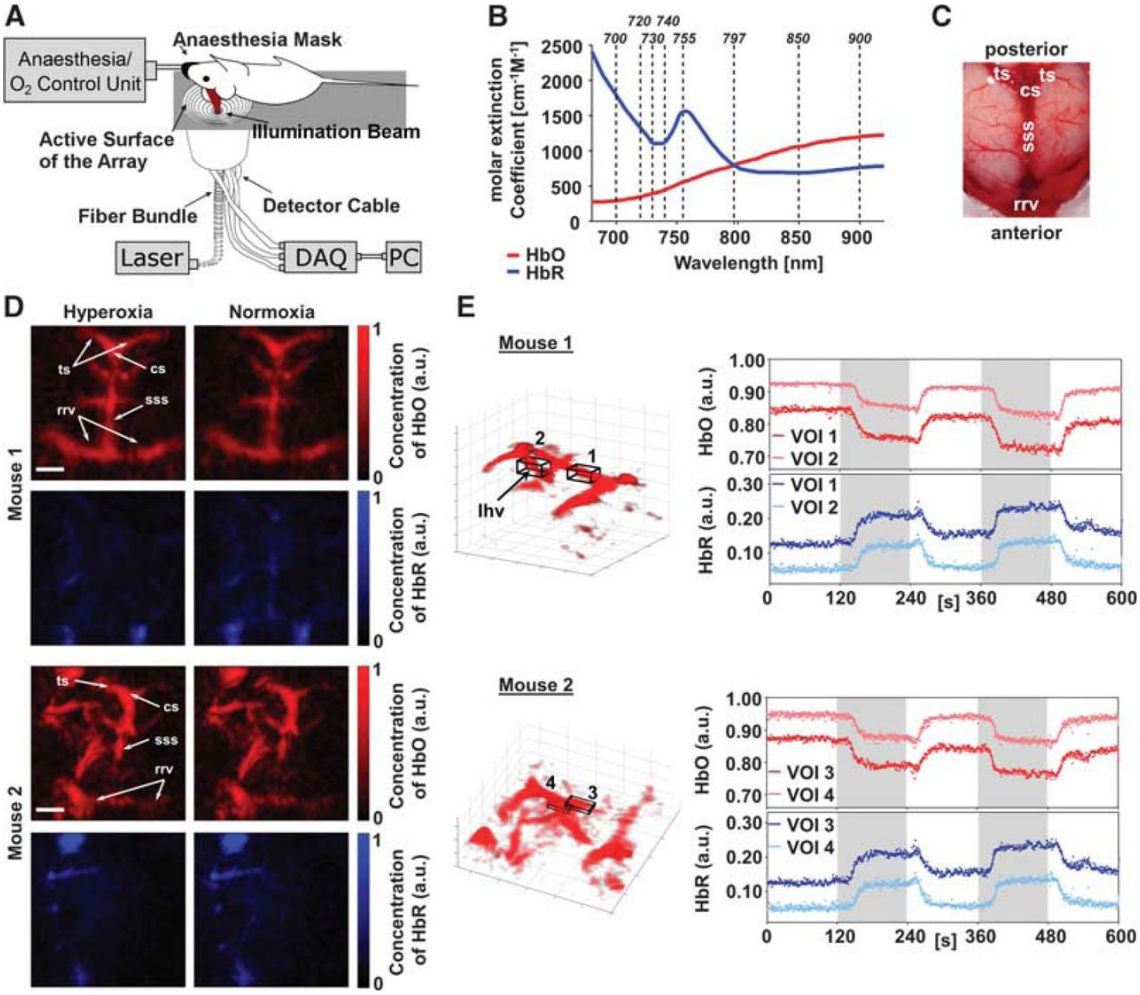

Figure IV.8: MS OA imaging of oxygenation levels of the mouse brain under hyperoxia and normoxia. **(A)** Experimental design. The mouse is placed in a supine position on top of the SMTA while its head is kept stationary using a stereotactical frame to minimize motion artifacts. **(B)** Extinction spectra of HbO and HbR in the near-infrared. Indicated are the eight wavelengths (dotted lines) used to acquire the MS data. **(C)** Postmortem image of a mouse brain with labels indicating the Rostral Rhinal Vein (RRV), the Superior Sagittal Sinus (SSS), the Confluence of Sinuses (CS) and the Transverse Sinus (TS). **(D)** MIP images (along the depth direction) showing the spatial distribution of HbO and HbR in the mouse brain under hyperoxia and normoxia. The head of the second mouse was angled in relation to the surface of the SMTA, revealing more lateral vasculature of the brain. Scale bars are 2 mm. **(E)** MIP visualizations of HbO under hyperoxia. Voxel of Interest (VOI)s were placed at the anterior part of the SSS and Longitudinal Hippocampal Vein (LHV). Time traces of the average signal intensity of HbO and HbR inside the VOIs are shown normalized to their respective HbT (dots) along with the moving average over 5 frames (lines). The time signals corresponding to concentrations of HbO and HbR clearly follow the changes between hyperoxia (white background) and normoxia (gray background). From [94].

the Institute for Biological and Medical Imaging and with approval from the Government District of Upper Bavaria under animal protocol reference number $55.2.1.54 - 2532 - 95 - 12$. Animals were anesthetized with isoflurane (1.5% to 2.5% v/v) in 100% O_2. During each experiment, physiological parameters of the mice, including blood oxygenation, heart rate, and body temperature were continuously monitored. To further avoid hypothermia, the body temperature of the mouse was kept constant using a heating pad (Kent Scientific, USA) that was controlled by a rectal thermometer. The mice were positioned parallel to the surface of the SMTA (Figure IV.8A) and their skull was fixed using a stereotactic mouse head holder (Narishige International Limited, UK) to minimize animal motion. OA signal acquisition was initiated under hyperoxic conditions (100% O_2) and the breathing gas was alternated every 2 minute between hyperoxia and normoxia (medical air, 20% O_2) for a total duration of 10 minutes. The gas mixture was manually controlled using a multi-gas flowmeter (UNO, Netherlands) keeping the isoflurane level constant in the inhaled gas. The SMTA used for real-time acquisition of the multi-spectrally excited OA signals was described earlier in Section III.1. For every experiment, the PRF of the laser was 10 Hz and OA excitation was performed using a total of eight different wavelengths (Figure IV.8B). Therefore, a MS dataset can be acquired within 0.8 second. Image reconstruction and spectral unmixing followed the processing pipeline described in Section III.1 and Subsection II.1.4. In addition, a simple model to correct for light fluence attenuation was implemented. As described in Subsection II.1.2, an exponential decay function along the depth direction was applied to all reconstructed volumes [208]. The map of blood oxygen saturation SO_2 was subsequently calculated on a per voxel basis via $SO_2 = HbO/(HbO+HbR)$. CBV was estimated as the number of voxels for which the total hemoglobin ($HbT = HbO+HbR$) concentration is higher than a give threshold. HbT is taken from images reconstructed at 797 nanometer (isosbestic point of hemoglobin, Figure IV.8B) and the threshold is established as a heuristically-determined factor times the standard deviation of the background. Specifically, the CBV was estimated as the number of voxels whose signal exceed the standard deviation of the background noise by a factor of at least 8.5.

IV.3.1.2 Results

A similar version of the following paragraph (subsubsection IV.3.1.2) was originally published in [101]. OA signals were acquired at two different head positions using two different mice while a series of 750 unmixed frames were recorded during each experiment. In Figure IV.8D-E, visualizations of the reconstructed OA signals of the cerebral vasculature are displayed. Major cerebral veins can be clearly identified. For better orientation, a labeled postmortem image of a mouse brain is shown in Figure IV.8. A movie visualizing the concentration changes of HbO and HbR in the whole brain over time can be found in the online supplementary of the journal (Supplementary Video 2) where there resarch was originally published [94]. As a next step, the temporal changes in concentration of HbO and HbR in specific VOIs during oxygenation stress was analyzed. In Figure IV.8E, the time traces of blood oxygenation levels, averaged over the corresponding VOIs, located in the SSS and in the LHV are plotted. The observed percentile changes were in good accordance with reported values from in MRI measurements for major cerebral veins under hyperoxia [209]. In addition, the temporal dynamic of changes in HbO and HbR, calculated from VOIs that were placed outside major vasculature in the cortex also followed the breathing gas stimulation cycle (Figure IV.9A). The suggested threshold criteria served well in separating vessel (hemoglobin) voxels from background noise and further allowed to generate three-dimensional masks from positively identified voxels corresponding to the CBV, which is exploited to analyse changes in vessel SO_2 (Figure IV.9B). This capacity is also

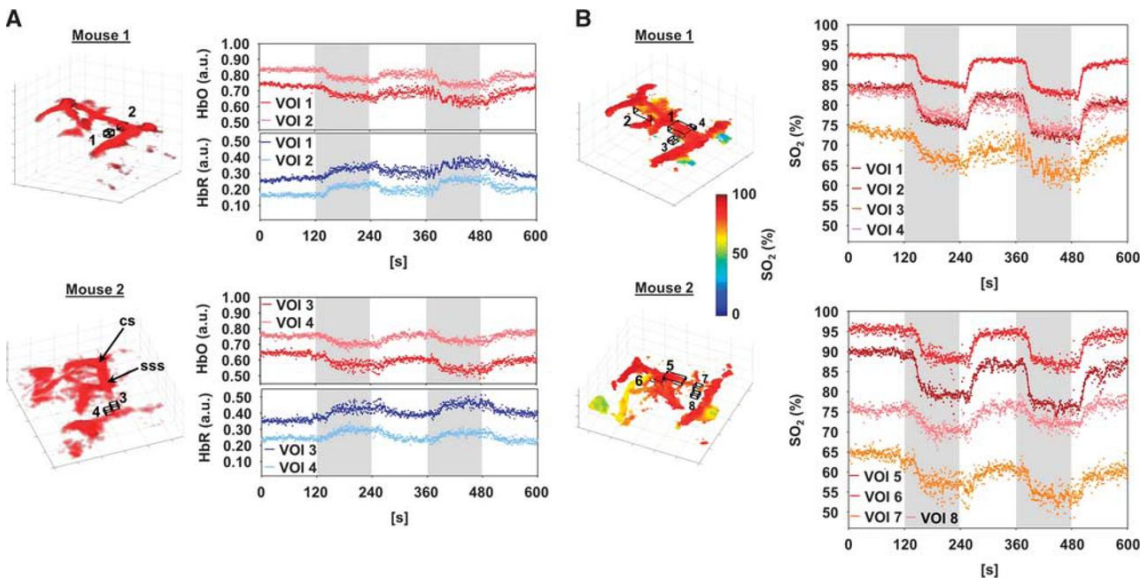

Figure IV.9: Analysis of mouse brain hemodynamics. **(A)** VOI 1, 2 and VOI 3, 4 for mouse 1 and 2, were placed outside the major vessels and inside the cortex. The temporal profile of the average signal value of HbO and HbR inside these voxels are plotted (for abbreviations, see Figure IV.8E). **(B)** 3D plots of the calculated SO_2 levels in the two mouse brains. Segmentation of the vasculature was achieved by using the thresholded reconstructed volumetric dataset acquired at 797 nanometer as a projection mask and the same VOIs as in Figure IV.8E were used. SO_2 changes could be monitored in the SSS (mouse 1: VOI 1; mouse 2: 5) and in the LHV (mouse 1: VOI 2; mouse 2: VOI 6). For visualization, only voxels exceeding the threshold were considered. In addition, SO_2 changes were analyzed in the VOIs shown in Figure IV.9A (mouse 1: VOI 3, 4; mouse 2: VOI 7, 8) with no threshold applied to the VOIs. From [94].

visualized in a video (Video 3) in the online supplement of the original publication [94]. The proposed imaging approach further allowed to directly measure the SO_2 level for any VOI using the spectrally-unmixed data [203]. Figure IV.9B shows the analysis of SO_2 changes in the VOIs placed inside the cortex but outside major vessels.

IV.3.1.3 Discussion

A similar version of the following paragraph (subsubsection IV.3.1.3) was originally published in [101]. The truly three-dimensional nature of the acquired data as well as the high spatial resolution across a large field of view of $\approx 1\,\mathrm{cm}^3$, covering the entire mouse brain [28], enabled optical contrast based visualization of deep brain structures, e.g. by resolving the LHV and its branching at depths between 3 and 4 millimeter without degradation of spatial resolution (see Supplementary Videos 2 and 3 of the original publication [94] and the HbR signal inside VOI 2 in Figure IV.8E). Furthermore, all of the presented data was acquired completely non-invasively, as compared to other optical studies with comparable spatial resolution that required skin removal and skull thinning [210]. Also, the compact system design further allowed to freely move the mouse head during data acquisition (see Supplementary Video 1 of the original publication [94]). Furthermore, the feasibility of the approach to serve as a functional neuroimaging technique was demonstrated by analyzing hemodynamic changes the mouse brain. Indeed, two situations have to be distinguished considering the resolution of the SMTA employed in this study ($200\,\mu$m): (1) The reconstructed voxel fully lies inside a blood vessel. Therefore, the reconstructed value

of the voxel directly reflects hemodynamic changes in that vessel. (2) The voxel only partially comprises vasculature, i.e. a certain percentage of the voxel are blood vessels smaller than the resolution of the systems. These two cases are not specific to the proposed approach but occur in all imaging modalities, whose spatial resolution is not sufficient to resolve microvasculature, e.g. MRI. However, it was demonstrated here that with the proposed system it is equally possible to resolve hemodynamic changes under partial volume assumptions as the measured changes of $\approx 10\%$ in venous SO_2 well match previously reported values [209] (Figure IV.9B). In fact, OA signals are generated by light absorption in blood, which is distributed everywhere due to the highly scattering nature of tissue. Thus, it may be argued that any hemodynamic change would impose alternations on the OA signal, even though the imaging system does not have the resolution to resolve all the microvascular structures responsible for these changes. However, several issues must be addressed in the future. As it was discussed in Subsection II.1.2, strong light absorption in superficial structures of the brain can have a crucial impact on the local photon distribution in deeper parts. Thus, the amplitude of OA signals originating from deeper structures in the brain cannot be reconstructed accurately, which may lead to false implications about the underlying neural activity pattern. Also, not all wavelengths experience the same light attenuation with depth, which additionally corrupts the acquired OA signals, particularly from deeper situated sources. It is obvious that the model that was implemented in this study, i.e. the exponential correction factor that was applied to the reconstructed OA volumes along the depth direction, to correct for such effects is very simplistic and more sophisticated models of light distribution must be developed to further improve data quantification. Finally, the spatial resolution of the current system is not sufficient to resolve cerebral microvasculature and thus must be improved in future system designs.

IV.3.2 Optoacoustic Tomography Identifies Thalamo-Cortical Activity during Epileptic Seizures

A similar version of the following introduction (Subsection IV.3.2) was originally published in [101]. Epilepsy is a neurological disorder that afflicts more than 1% of the today's world population at least once in a lifetime. It is caused by abnormal neural synchronization that causes recurring seizures which spread across both the cortical and subcortical regions of the brain. Since bilateral Spike–Wave Discharges (SWD) at 3-4 Hz usually accompany epileptic seizures on Electroencephalogram (EEG) recordings, these discharges can be regarded as clear indications of this disorder. While a clear understanding of the neural mechanisms responsible for epileptic seizures still remains elusive, it is well recognized, however, that SWDs are caused by synchronized activity in the thalamo-cortical loop as neither the neocortex nor different nuclei of the thalamus can sustain SWD [211]. Therefore, the advancement of efficient therapies strongly hinges on the ability to accurately characterize the saptio-temporal dynamic of epileptic seizures.

In order to further progress the understanding of abnormal epileptic activity in pre-clinical models and subsequent clinical studies, imaging techniques assume a crucial part [212, 213]. However, the current state of the art suffers from crucial insufficiencies. While non-invasive imaging modalities such as MRI [213] or diffuse optical tomography [214] have shown the ability to visualize the functional activity of the whole brain, they remain insufficient due to lack of spatial and/or temporal resolution needed for accurate characterization of seizure dynamics. Other optical methodologies, though utilized to successfully localize cerebral cortex activity in vivo [215], still remain out of contention for visualizing subcortical brain structures. Recently developed miniature endoscopic probes offer a solution to the problem of imaging deep brain

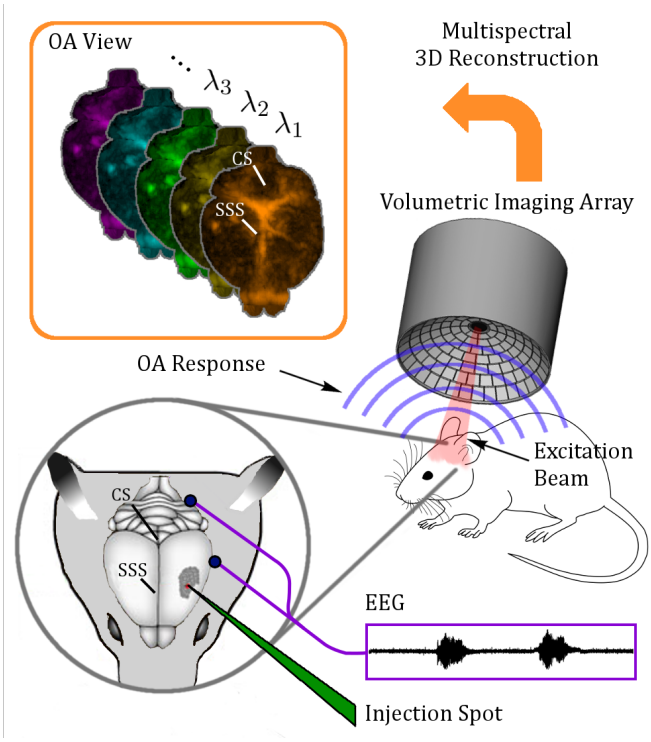

Figure IV.10: Cartoon of the experimental design. Epileptic seizures were induced by transcranial injection of 4-AP into the neocortex of the mouse brain (green solid arrow). EEG signals were recorded via screw-type electrodes implanted into the skull (black circles) and recordings were synchronized with the initiation of OA data acquisition. Pressure signals were excited using a pulsed laser source and detected via a SMTA. MS volumetric datasets are generated for each laser pulse at different wavelengths. The outline of the mouse brain as well as major vasculature features are indicated. From [101].

areas which are not accessible by intravital microscopy [216]. Yet, these are inherently invasive techniques that may cause undesired alterations to brain activity and additionally limit the simultaneously acquired recordings to very limited brain areas. A viable alternative for high resolution deep brain observations is offered by the vastly growing OA imaging techniques that have been successfully utilized for monitoring hemodynamic responses of the brain caused by electrical stimulation [50, 207] and epileptic activity [215, 217, 218]. However, even with state-of-the-art OA imaging techniques, insufficient volumetric spatio-temporal resolution and lack of whole brain imaging capacity make the efficient visualization of epileptic brain activity an intricate task.

The current study, it is demonstrated that OA tomography is capable of accurate transcranial monitoring of epileptic seizures in whole mouse brains. Specifically, after inducing epileptic seizures by intracortically injecting 4-Aminopyridine (4-AP) into the neocortex of living mice, the thalamo-cortical activity is visualized in real-time via this approach.

IV.3.2.1 Mouse Preparation & Epilepsy Model

A similar version of the following paragraph (subsubsection IV.3.2.1) was originally published in [101].

For this study, eight to twelve week old Female athymic nude-Foxn1nu mice (Harlan Laborat-

ories LTD, Itingen, Switzerland) were used. Each procedure was performed in full compliance with the institutional guidelines of the Institute for Biological and Medical Imaging and with approval from the Government District of Upper Bavaria. During surgery, mice were anesthetized with isoflurane (2.5% v/v) in 100% O_2 and their position was fixed via a stereotactic mouse head holder (Narishige International Limited, UK) to suppress head motion. The mice were then placed into a robot stereotactic drill and injection system (Neurostar, Germany), where skin and underlying tissue over the skull were removed. Next, two small holes were drilled into the skull, one posterior and one laterally, by using a handheld surgical drill (Ideal Micro-Drill, Harvard Apparatus, USA) and two stainless steel screw electrodes were implanted into these holes to record EEG signals (see Figure IV.10). Another smaller hole for intracranial injection of substances was drilled laterally to the SSS and on the same side where the EEG screw was located.

The potassium channel blocker 4-AP model of epileptic seizures has been shown to allow for reproducible studies of the onset, maintenance and propagation of abnormal neural synchronization using different electrophysiological and imaging methods [219, 220]. 4-AP inhibits the $K+$ outward current, which, in turn, causes prolongation of action potentials and abnormal neural synchronization [219]. This model can generate focal seizures lasting up to hundreds of seconds with interictal periods of minutes for a duration of several hours [217]. In the present study, 0.6 μL of 25 mM 4-AP dissolved in Artificial Cerebrospinal Fluid (ACSF) were injected intracortically by a robot injection system (Neurostar, Germany) using a $15-25\,\mu$m diameter glass microcapillary. Injections were made ≈ 0.5 mm below the dura mater surface into the neocortex.

After surgical preparation concluded, the mice were positioned in the OA imaging setup and isoflurane anesthesia was continued with $1.0-1.5\%$ v/v in 100% O_2 with a flow rate of ≈ 0.7 L/min. The SMTA was mounted on top of the mouse skull while acoustic coupling between the transducer elements and the mouse skull was ensured via an inserted agar pad (1.3 g/100ml in deionized water). The EEG was recorded by means of an AC/DC differential amplifier (Model 1700, A-M Systems, Sequim, USA) and digitized at 1000 Hz (ATS9351, Alazar Technologies Inc., Canada). EEG recording was synchronized to OA acquisition, thus allowing to temporally coregister neuronal activity with both methods. The physiological parameters, including blood oxygenation, heart rate, and body temperature were continuously monitored (PhysioSuite, Kent Scientific, USA). The body temperature of the mouse was kept constant using a heating pad (PhysioSuite, Kent Scientific, USA), which was regulated via a rectal thermometer.

IV.3.2.2 Data Acquisition & Processing Pipeline

A similar version of the following paragraph (subsubsection IV.3.2.2) was originally published in [101]. The experimental system used for real-time acquisition of MS volumetric OA image data is described in detail in Section III.1. For this study, the laser was set to operate at 10 Hz and a total of five wavelengths (700, 730, 750, 800 and 850 nanometers) were used. Thus, an entire OA volumetric dataset was acquired within 0.5 second. The data processing pipeline is summarized in Figure IV.11 and it follows the outline commonly implemented in MRI experiments [221]. Signal preprocessing, image reconstruction and spectral unmixing followed the procedure described in Subsection II.3.4 and Section III.1. Intensity variations due to fluctuations in the laser energy were compensated by normalizing every reconstructed frame with the average OA signal intensity emitted from a small India ink rod that was placed in the illumination beam between the fiber outlet and the mouse head.

Motion artifacts in the reconstructed OA images due to breathing and spastic motion of

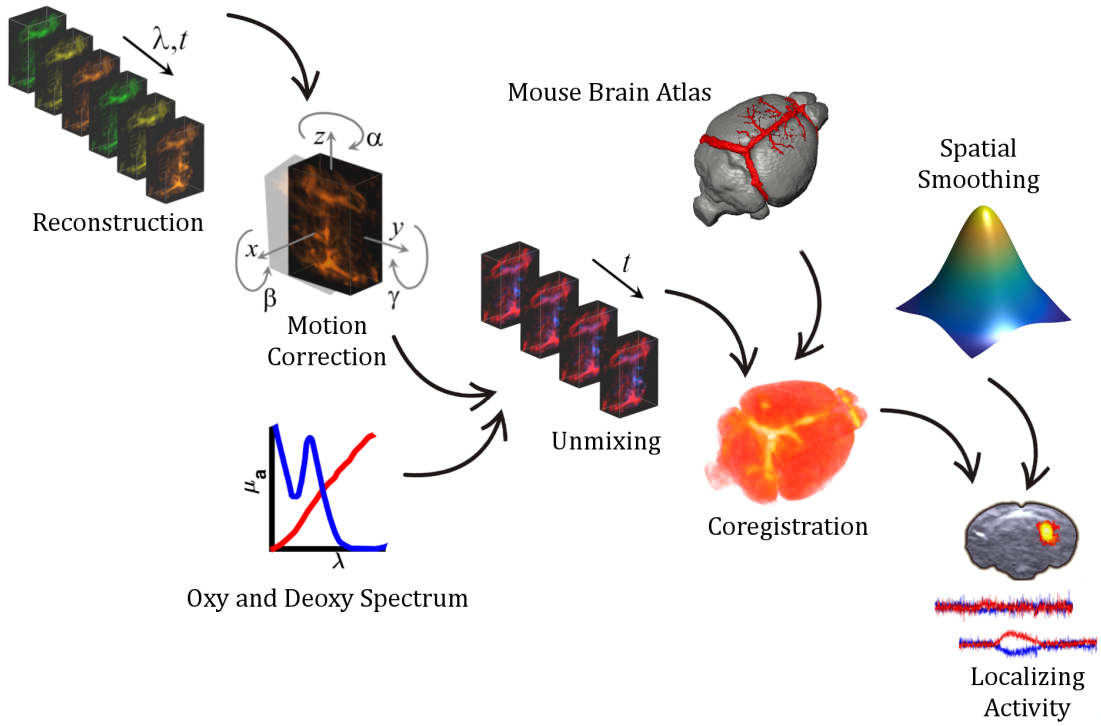

Figure IV.11: Overview of the data processing pipeline. First, OA data is separately reconstructed for each wavelength and time-point. In the next step, affine translational and rotational affine transformations are utilized to compensate for breathing and spastic motion for each reconstructed frame. Then, spectral unmixing is performed using the known absorption spectra of HbR and HbO. As result, volumetric maps representing their spatial distribution are generated. These maps are then coregistered to standardized brain atlases representing the average vascular morphology of the mouse brain as well as the spatial sectioning of known brain regions. After applying a Gaussian filter for spatial smoothing of the maps, hemodynamic changes representing neural activity can be localized by fitting an Optoacoustic Hemodynamic Response Function (OHRF) to the time trace of each voxel. The performed coregistration allows then to identify active regions of the brain. Image and caption from [101].

the mouse can corrupt the result of the unmixing algorithm. Therefore, a motion correction procedure was implemented for this study to minimize the influence of mouse motion. Specifically, a time reference frame was chosen using the reconstructed volume at 800 nanometer and the remaining wavelengths of the same time instant were transformed to match its position using three-dimensional affine transformations. The transformed frames of each wavelength were then used as position references for all other time instances of the same wavelengths. Frame coregistration was implemented in MATLAB® 2013 using the available three-dimensional affine transformation package, where the search space was limited to linear translations and rotations only. As a result, motion-artifact free volumetric maps representing the spatial distribution of HbO and HbR were calculated for every time instance using the motion corrected reconstruction of every set of wavelengths as it is described in Subsection II.1.4.

The unmixed HbO and HbR maps were then coregistered with standardized brain atlases[1] representing the average vascular morphology in a mouse brain [222] as well as the spatial

1 Available at www.mouseimaging.ca/technologies/mouse_atlas

sectioning of known brain regions [223, 224]. First, fiducial markers were estimated manually for a single frame using known well-resolved structures of the brain atlas as well as dominant vasculature features that are visible in the reconstructed OA volumes, such as the SSS, the CS and the TS. The estimated coregistration parameters for isotropic scaling, rotation and translation were then used to automatically coregister all remaining frames in the time series.

Eventually, active voxels were identified in the coregistered oxygenation maps by modeling of an OHRF for both the HbO and HbR channels. Similar to hemodynamic response functions that are used for the analysis of functional MRI data [225], an OHRF was defined from empirical findings of the current study for voxels where hemodynamic changes associated with neuronal activation were identified (see Figure A.1). Assuming that the temporal response of every voxel can be modeled with independent characteristic onset and offset time constants for neuronal activity, it was expressed as

$$T(\tau) = \alpha \left(\Theta(t-\tau)\, e^{-\left(\frac{t-\tau}{\delta}\right)^2} + \Theta(\tau-t)\, e^{-\left(\frac{t-\tau}{\gamma}\right)^2} \right) + \text{Offset} \tag{3.1}$$

where Θ is the Heaviside step-function. From the measured data, it was empirically concluded that the shape of the OHRF in both the HbO and the HbR channel can be modeled by Equation 3.1, where τ corresponds to the termination time of the neuronal activity related to the seizure and with independent characteristic time parameters δ and γ for the rise and fall parts. Like in MRI studies, the model was fitted to the time trace of each voxel independently and active voxels were separated from noise voxels by constraining τ and δ to a range around the termination time and the duration of the seizure as measured in the EEG, respectively. In addition, the seizure amplitude α as well as the root mean square error ϵ of the fit was used to further suppress noise voxels. Before fitting the data, the three-dimensional maps representing the spatial distribution of HbO and HbR at every individual time-step were smoothened by applying a Gaussian filter with a sigma of 2 voxels.

IV.3.2.3 Results

A similar version of the following paragraph (subsubsection IV.3.2.2) was originally published in [101]. In total, five different mice were imaged under anaesthesia and the acquired OA and EEG signals were used to investigate the 4-AP acute model of focal epilepsy. The changes in HbO and HbR were individually analyzed in several voxels within the brain. A representative dataset is shown Figure IV.12. Specifically, MIPs of the spectrally-unmixed HbO concentration of the mouse brain is shown along the transveral and coronal direction. Voxels in and around the injection site of 4-AP, i.e. the location of the main epileptic focus, show clear increases and decreases in HbO and HbR respectively, together with increased brain activity as visible in the EEG (Figure IV.12d, traces 1 and 2). Also, it was found that these hemodynamic changes persist longer than the neuronal activity that has been previously observed with optical methods [219]. Significant increases in HbT accompanied the hemodynamic changes in the seizure focus (Figure IV.12e, traces 1 and 2), which most likely is attributed to an increased blood flow in the activated brain regions. The analysis of voxels in the contralateral (cl) brain hemisphere at similar depths (Figure IV.12d, traces 3 and 4) showed did not show changes in HbO or HbR. Notably, similar HbO and HbR traces as in the activated area were also seen in the SSS (Figure IV.12d, traces 6 and 7). One explanation for delayed onset of these changes in voxel 6, when also considering the absence of signal alterantions in voxels 5 and 12 (located in the CS and the LHV, respectively), is a bidirectional blood flow in the SSS, as it was previously reported [226]. Analysis of deeper regions at anterior locations to the 4-AP injection

site (Figure IV.12d, traces 8 and 9) permits estimation of the extent of the activated area, as no measurable changes were observed in the time traces corresponding to these voxels. Analysis of voxels located inside the Thalamus (TA) demonstrated the depth-resolving capability of the presented approach. While comparatively weaker hemodynamic changes occurred in this region, they can still be detected in the time traces (Figure IV.12d, trace 10). It is important to notice the delayed onset of activity inside the TA as compared to the seizure-onset in traces 1 and 2 (Figure IV.12d), while this activity was not resolved by the EEG. On the other hand, much like for the cortical regions, no hemodynamic changes inside the cl side of the TA were detected (Figure IV.12d, trace 11).

Hemodynamic changes inside the TA were also observed in an independent experiment (Figure A.2, traces 1 and 2), which however occurred in a unrelated fashion to the strong activity measured in the EEG. In general, analysis of the mouse experiments always showed a high correlation between the hemodynamic OA response and changes in the EEG amplitude. The results of another experiment are shown in Figure A.2. Again, robust hemodynamic responses in HbO and HbR were observed around the injection spot of the 4-AP accompanied by changes in the EEG signal (Figure A.2d-e, traces 1 and 2). Notably, a delayed onset of activity in the TA as compared to the cortical regions was determined again, but only in the HbO signal (Figure A.2d, trace 10). However, also in this case, the hemodynamic changes persisted longer than activity in EEG was recognized. Furthermore, no hemodynamic responses were observed in the cl brain hemisphere or at locations anterior to the 4-AP injection spot (Figure A.2d-e, traces 3, 4, 11 and 8, 9). In addition, a control experiment was performed, where only ACSF was injected. The analysis of the OA and EEG data for the control mouse is shown in Figure A.3. In summary, no EEG activity or hemodynamic changes could be detected for the duration of the experiment.

Figure IV.13a-c shows the calculated seizure-related activity map overlayed on top of a single-wavelength OA image. Seizure-related hemodynamic changes can be clearly identified around the injection spot of 4-AP in the left hemisphere of the Parietal-Temporal Cortex (PC) and further neuronal activation is seen in the left Frontal Lobe (FL). The activity pattern reaches its global maximum close to the surface of the brain in the PC but also reaches out to deeper situated structures in the PC and the FL. Hemodynamic changes further spread into the SSS. Finally, a time to peak analysis (Figure IV.13d) using the fitted amplitude values α revealed that the epileptic seizure originated in the cortex and subsequently generated a delayed activity inside the TA about 4.5 mm inside the brain.

IV.3.2.4 Discussion

The combination of the proposed functional OA neuro-tomography methodology together with the developed data processing pipeline has proven its significance for studying a mouse model of epilepsy. It allows for highly spatially and temporally resolved transcranial volumetric in vivo mapping of brain activity associated with epileptic seizures. Particularly the ability for deep brain imaging allows the mapping of brain activity, in regions that cannot be accessed with high-resolution optical methods with very high temporal resolution. This is especially of importance as the accurate localization of epileptic seizures plays a crucial role in advancing the understanding of the underlying mechanisms, hence aiding the development of anti-epileptic therapies. This, however, is severely complicated by the fact that the underlying pathologies for focal epilepsy are distributed throughout different areas of the brain, where seizures frequently originate from thalamo-cortical interactions. In healthy brains, millions of neurons inside the thalamic nuclei and different areas of the sensory cortex [227] build up the thalamo-cortical

system. They are responsible for regulating the flow of information between the thalamus and cortical brain regions [228]. They do this by adapting their inherent oscillatory properties in response to different thalamo-cortical sensory and feedback inputs [211] with oscillations usually having frequencies of a few Hertz. Pathological synchronizations caused by epileptic seizures, however, change the frequencies of these oscillations [229]. The results presented here complement electrophysiology studies of these oscillations by providing volumetric imaging data of hemodynamic changes in the whole mouse brain.

Important observations from other studies were reproduced in the results of the presented experiments. Specifically, it was shown that the intracortical injection of 4-AP causes focal seizures that originate at the injection spot [219] and it was further reported that epileptic seizures induce changes in oxygenation and cerebral blood flow at the epileptic focus [230]. Both of these finding were confirmed here, which further demonstrates the validity of the suggested approach. However, the exact role of neurovascular coupling in the seizure-mechanisms still remains unknown. The decrease in HbR around the main epileptic focus reflects a high oxygen consumption attributed to an increased neuronal activity associated with the seizures [220]. At the same time, the measured changes in HbT concentration probably reflect an increase in blood flow [220], which is consistent with the supply of a higher amount of HbO to the seizure-area.

In summary, by using high frame-rate MS volumetric OA tomography, completely non-invasive real-time visualization of synchronized epileptic foci in the whole mouse brain was demonstrated for the first time. Moreover, the presented system can also be applied to investigate the neuronal response to different somatosensory stimulations (e.g. paw or whisker stimulations).

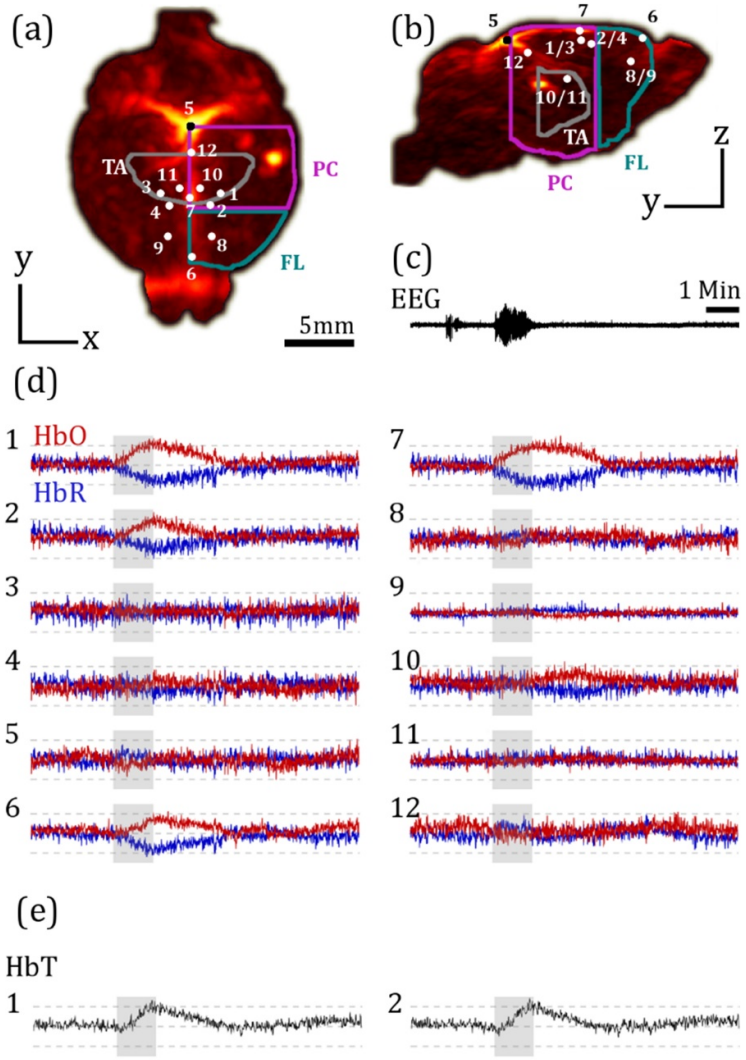

Figure IV.12: Analysis of hemodynamic changes during epileptic seizures. **(a)** Transversal MIP of the HbO distribution in the mouse brain. Analyzed voxels are indicated and the corresponding time traces are plotted in **(c)**. Colored outlines define the location of brain regions (grey: Thalamus (TA); purple: Parietal-Temporal Cortex (PC); green: Frontal Lobe (FL)). **(b)** Coronal MIP view of **(a)**. **(c)** EEG and time traces of HbO (red) and HbR (blue) are plotted of the voxels shown in **(a)** and **(b)**. Grey boxes indicate the length of the neural activity during seizure as measured by the EEG. Dotted grey lines indicate baseline and ±50% relative changes for each curve. HbT was calculated as the sum of HbO and HbR and curves were only plotted for voxels with changes bigger than the background noise. The analyzed regions encompass the side of the brain where 4-AP was injected and respective voxels in the contralateral (cl) side of the brain and inside major draining veins: Injection site (1, 2) and (cl: 3, 4); SSS (6, 7); CS (5); LHV (12); voxels anterior to the injection site (8, cl: 9); TA (10, cl: 11). From [101].

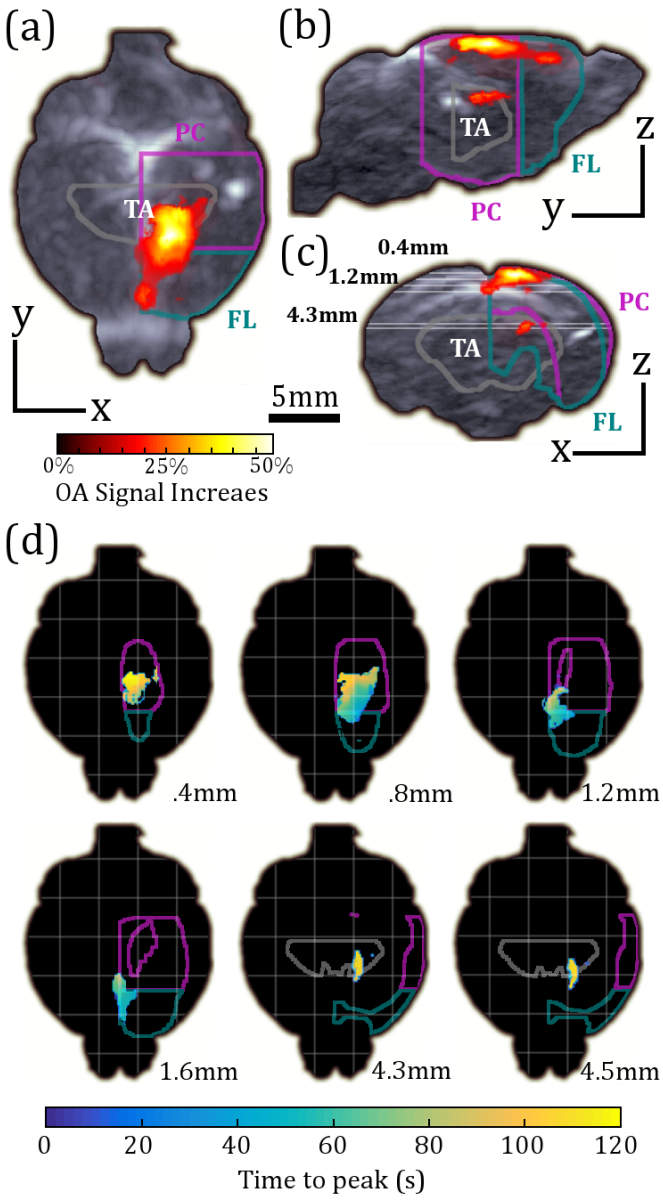

Figure IV.13: Plots of the activity map showing hemodynamic changes as identified by fitting the OHRF. Shown are MIP views along the transversal **(a)**, sagittal **(b)** and coronal **(c)** directions of the brain of the corresponding OA reconstruction at 800 nm . Superimposed is the neuronal activity pattern, i.e. the α-value, as it was calculated from fitting the OHRF. The spatial dimensions of the TA (grey), the FL (green) as well as the PC (purple) are outlined. The parameters for the OHRF were: $3\,\text{min} < \tau < 4\,\text{min}$, $\epsilon = 0.05$, $\alpha/\text{Offset} \geq .15$. **(d)** Time-to-peak analysis of activated areas in the brain shown in horizontal slices as indicated in **(c)**. Activity arises first in the injection site of 4-AP in the boundary between PC and FL (slices 0.8, 1.2 and 1.6 mm) and progresses further into the PC (slices 0.4 and 0.8 mm). Activity inside the TA clearly occurs past the activity in the cortical regions and can be detected in depths up to ≈ 4.5 mm (slices 4.3 and 4.5 mm). From [101].

IV.4 Visualization of Multi-Scale Dynamics in Mice using Optoacoustic Tomography

In this study, the newly developed OA scanner introduced in Section III.2 was utilized to investigate multiple dynamic biological processes in mice ranging from beat-to-beat visualization of a mouse heart at 100 Hz volumetric frame rate to slower contrast agent kinetics in selected areas at the entire renal system level to whole-body longitudinal studies of tumor growth. The research was originally published in [177].

IV.4.1 Introduction

A similar version of the following introduction (Subsection IV.4.1) was originally published in [177]. Almost all advancement in life sciences is based on the capability to observe dynamic functional events non-invasively without interfering with the environment of the organism while gathering data [231]. However, in vivo imaging over multiple temporal scales is typically seen in connection with tough compromises, which span a triangle between the achievable field of view, spatial resolution as well as image quality. Functional MRI, for instance, can image whole mammal organisms at a high spatial resolution. Its spatio-temporal resolution, however, is limited and real-time imaging is limited to single two-dimensional slices over a small field of view [232]. Optical imaging modalities, on the other hand, are often limited due to light scattering, thus offering only poor spatial resolution at very limited depth when applied to whole organisms [233]. Traditionally, multi-modality methods were employed to gather data at multiple timescales, for example by hybridization of US for fast imaging of highly confined areas with data of extended areas from whole-body imaging techniques, such as MRI or CT [234, 235]. Nevertheless, the entirely different sensitivity, contrast mechanisms and other imaging characteristics that are linked with dissimilar modalities, frequently limit efficient aggregation of information gathered at multiple scales of time and space [236]. However, as it was discussed earlier in Subsection II.1.2 and Section III.2, OA is ideally poised to meet these challenging requirements due to its unique capability to deliver high resolution images on microscopic and macroscopic length scales with the same contrast [35, 237]. In contrast to most optical imaging modalities, OA does not suffer from the severe resolution degradation with increasing depth due to light scattering [29]. Light is converted into acoustic energy deep inside the tissue due to the OA effect and therefore the spatial resolution in OA imaging is mainly determined by US diffraction [55]. It was shown that OA not only provides excellent optical absorption contrast stemming from endogenous chromophores such as hemoglobin [238] and melanin [239, 240], but also from targeted and activatable probes [27, 241] as well as from genetic labels [112, 242, 243]. So far, a great variety of different OA tomography systems have showcased two-dimensional and three-dimensional imaging capabilities with temporal resolution in the range of tens of milliseconds [38, 131, 173, 174]. However, efficient visualization of multi-scale dynamics is still challenging with all current system designs due to very long acquisition times as well as insufficient sizes of the effective field of view. Even though, it was demonstrated that the previously introduced systems can render three-dimensional OA images from whole mice or organs with sub-millimeter resolution [71, 86, 87], none of the proposed solutions were capable of delivering real-time data from a living organism. In contrast, the newly developed OA scanner from Section III.2, offers the unique capability to visualize dynamic processes at multiple scales. In this study, various multi-scale dynamic imaging capabilities, ranging from volumetric millisecond-scale visualization at the whole organ level, via tracking contrast agent kinetics in dedicated areas, to whole body longitudinal studies with unprecedented image

quality are demonstrated.

IV.4.2 Materials & Methods

A similar version of the following paragraph (Subsection IV.4.2) including all sub-paragraphs was originally published in [177]. The OA imaging system was described in detail in Section III.2 and the same data acquisition procedure and reconstruction parameters were also used in the following experiments. Here, a total of three in-vivo mouse studies were performed. All animal experiments were performed in full compliance with the institutional guidelines of the Institute for Biological and Medical Imaging and with approval from the Government District of Upper Bavaria. All in vivo experiments were performed under isoflurane anesthesia (2-3% v/v) in 100% O_2 and the temperature of the water bath was set to 34°, controlled by an electric heating stick. The contrast agents used in this study were diluted in Phosphate-buffered Saline (PBS) and injected intravenously through a tail-vein catheter.

First, the heart region of an 6 month old female athymic nude-Fox1nu mouse (Harlan Laboratories LTD, Switzerland) was imaged using an excitation wavelength of 800 nanometer and a PRF of 100 Hz. After data recording concluded, the experiment was repeated using the same acquisition parameters but this time 100 nanomol of ICG, dissolved in 100 μl of PBS were injected before signal acquisition was initiated. In addition, an anatomical whole-body image was acquired using an illumination wavelength of 800 nanometer and a PRF of 100 Hz, where signals were averaged 50 times for every position. For the second study, an eight-week-old Female athymic nude-Fox1nu mouse (Harlan Laboratories LTD, Switzerland) was used for tumor inoculation. The athymic nude-Fox1nu mutant nude mice strain is a suitable allograft host since defects in the immune system enable an effective and reproducible tumor growth. Specifically, an orthotopic tumor was grown by subcutaneous injection of 5×10^5 4T1 murine breast cancer cells into the thoracic mammary fat pad and whole-body imaging experiments were performed at days 6, 8 and 11 post injection at 800 nanometer excitation wavelength and a PRF of 100 Hz, where signals were averaged 50 times at each position. On day 11, an additional OA real-time dataset of the tumor region using five different wavelengths (730, 760, 800, 850, 900 nanometer) and a PRF of 100 Hz was acquired after 100 nanomol of ICG dissolved in 200 μl of PBS were injected into the tail vein of the mouse. In the last study, 10 nanomol of AF750 dissolved in 200 μl of PBS were injected into the tail vein of another 6 weeks old female athymic nude-Fox1nu mouse (Harlan Laboratories LTD, Switzerland) and the entire kidney region was repeatedly imaged for 35 minutes using seven different wavelengths (710, 730, 745, 765, 800, 850 and 900 nanometer) and a PRF of 50 Hz, where each individual scan of the whole kidney region required approximately 5 minutes. MS signal unmixing was performed using the linear model described in Subsection II.3.4.

IV.4.3 Results

A similar version of the following paragraph (Subsection IV.4.3) including all sub-paragraphs was originally published in [177].

IV.4.3.1 High-Frame-Rate Volumetric Imaging at the Whole Organ Level

Figure IV.14 shows MIP images of reconstructed OA signals acquired from the mouse heart of consecutive time points. The reconstructions are superimposed to the anatomical whole-body image. The MIP view was slightly rotated to the left for a better visualization of the heart chambers. The image series nicely demonstrates the imaging power of the proposed

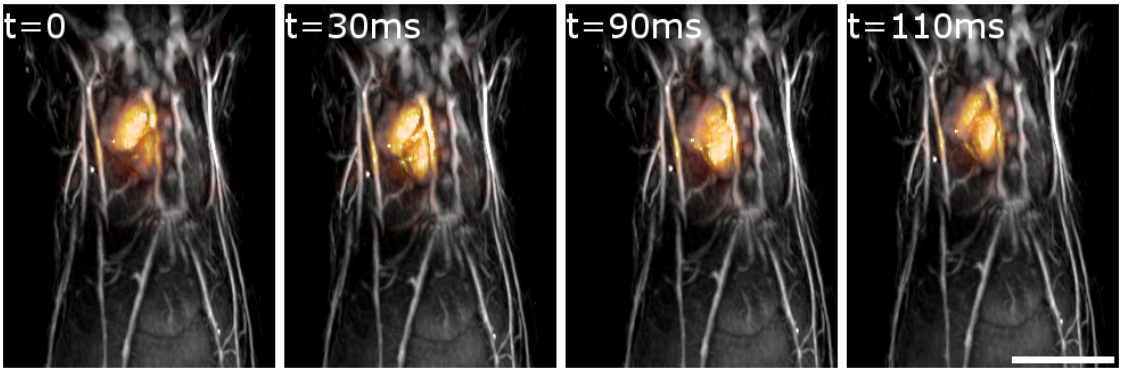

Figure IV.14: Real-time data of different states and phases of the mouse cardiac cycle superimposed on a full body anatomical image. $t = 0$ ms: ventricular systole, $t = 30$ ms: ventricular filling, $t = 90$ ms: ventricular diastole, $t = 110$ ms: ventricular ejection. Scale bar corresponds to 1**cm**. From [157].

system. Different states in the heart cycle can be time resolved and clearly identified. A video containing the full image sequence can be found in the online supplementary of the journal, where the research was originally published (Movie 5 in [157]). The physiology of the mouse heart was further investigated by injecting ICG into the tail-vein before another fast temporal sequence of three-dimensional images was acquired. A series of MIP images from the time sequence are displayed in Figure IV.15A. Specifically, the spatio-temporal distribution of the contrast agent was investigated, by plotting the time trace of the OA intensity of four voxels (dimmed lines) corresponding to designated morphological structures in heart region (blue: right ventricle, red: left ventricle, green: thoracic vessel, yellow: coronary artery), together with their low-lass-filtered equivalents (bold lines). The location of the voxels are color marked in Figure IV.15A, while the corresponding traces are plotted in Figure IV.15B using the same color. In addition, Fourier analysis was performed on the unfiltered signals using different time windows (green and yellow box). The windowed time signals and the corresponding Fourier spectra are plotted in Figure IV.15C. The analysis allows to deduce the cardiac (7.1 Hz) and respiratory (1.4 Hz) rates, which are both in the normal physiological range. The low-pass filtered time traces can further be exploited to segment out the heart chambers in the volumetric dataset, based on the timing of the ICG bolus appearance. Specifically, the time-to-peak value for each image voxel is determined. The result is shown in Figure IV.15D. The shape of the heart chambers can be clearly identified. Moreover, by considering the time difference between peak values for the voxels located in the right versus the left ventricle, it is possible to estimate the pulmonary transit time, whose value was determined to be $\Delta t_p = 1.24$ seconds. As expected, this value lies within the normal physiological range since a healthy mouse was used for this experiment. However, the proposed method may potentially serve as a useful indicator of ventricular dysfunction. Note that this type of analysis, based on resolving fast contrast agent perfusion three-dimensionally on a 10 millisecond temporal scale is not possible with other cardiac imaging modalities, such as MRI or CT, which commonly rely on gated data acquisition for high-frame-rate visualization of the beating heart. Eventually, the blood flow velocity was estimated by calculating the time delay between the ICG bolus appearance at the thoracic artery and a coronary artery (see Section A.2 for further details). The determined value for the delay was $\Delta t_{ca} = 300$ milliseconds, which translates into 10 millimeter per second flow velocity in the coronary artery.

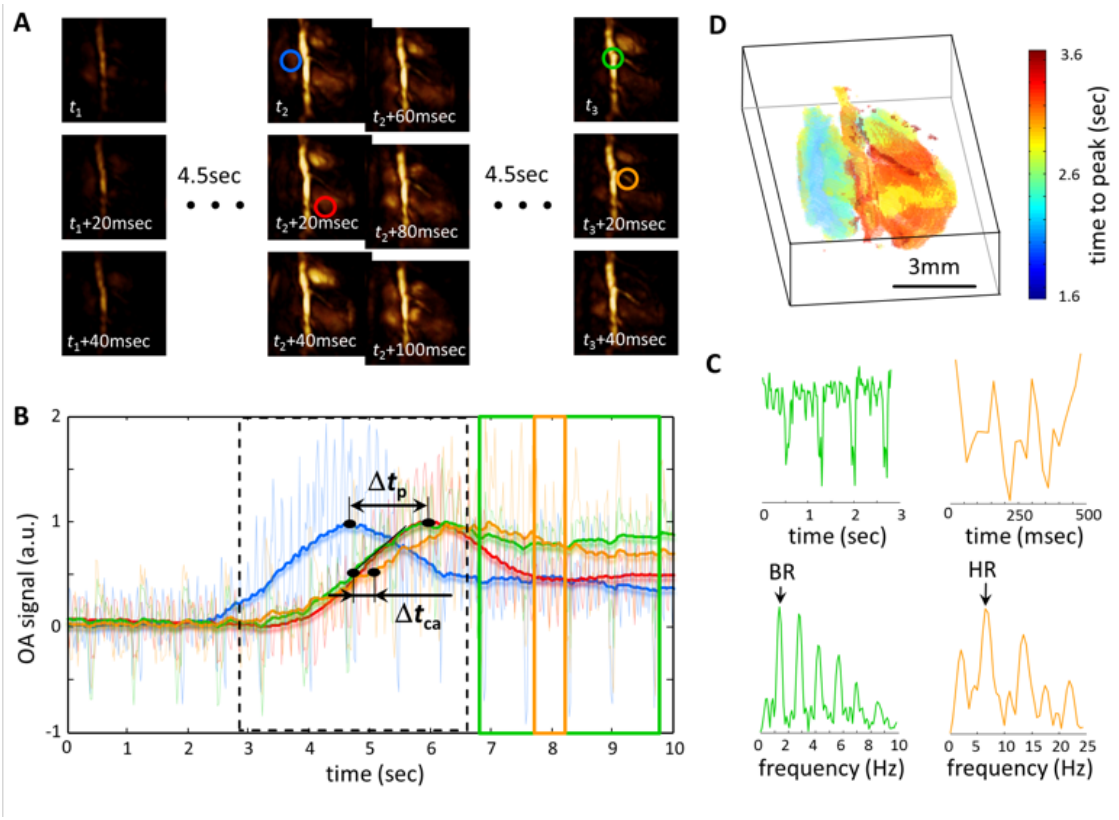

Figure IV.15: High-frame-rate three-dimensional imaging at the whole organ level. **(A)** MIP of the volumetric OA images acquired from a living mouse heart after tail-vein injection of 100 nanomol of ICG at $t_1 = 0$ seconds. **(B)** OA signal traces (dimmed lines) and their low-pass-filtered equivalents (bold lines) for the respective areas as it is indicated in **(A)**. The pulmonary transit time Δt_p and the delay Δt_{ca} between the ICG appearance at a coronary artery versus the thoracic artery are indicated. **(C)** Zoom into the signal traces marked with equivalent color in panel **(B)** along with their respective Fourier transforms. The two distinctive peaks correspond to the breathing rate (BR) and heart rate (HR). **(D)** Segmentation of the mouse heart chambers based on the time-to-peak analysis of the injected ICG. From [177].

IV.4.3.2 Contrast Agent Kinetics

Figure IV.16A displays three representative anatomical whole-body images of the tumor-bearing mouse superimposed with the spectrally-unmixed OA MIP images indicating the spatial distribution of the ICG contrast agent in the tumor region at different time instances during the real-time acquisition. At day 11, the diameter of the tumor was approximately 8 mm. A video showing the whole time series can be found in the online supplementary of the journal, in which the results were originally published (Video 4) [177]. The real-time data was exploited to further investigate the differential kinetic profiles of ICG in selected voxels (colored circles in Figure IV.16A) by analysing the corresponding signal intensity time traces (Figure IV.16B). Specifically, the decay and increase rates associated with the concentration of the injected ICG were determined for the different regions by fitting a mono-compartment pharmacokinetic model (first order kinetics) to the time signals [244] (see Section A.1 for more detailed information). First, the throughput capacity of the tumor neovasculature was estimated using the time-resolved amplitude signal of the contrast agent in the tumor area

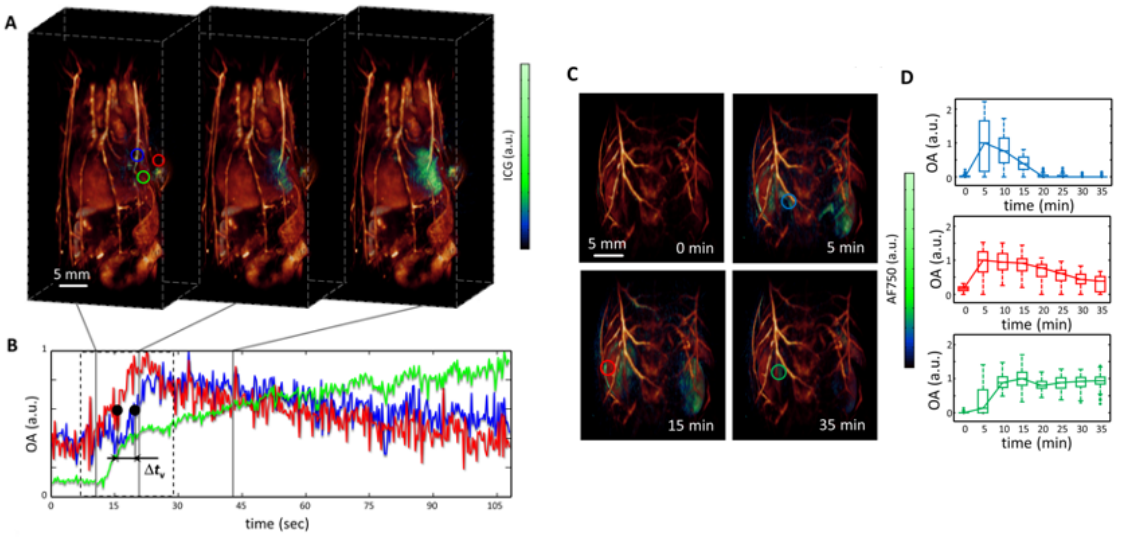

Figure IV.16: Contrast agent kinetics in larger regions. **(A)** MIP images of the spectrally-unmixed distribution of ICG (green) for three representative instants after injecting 100 nanomol of the agent into the tail-vein at 0 seconds. The kinetic images were superimposed onto the whole-body OA anatomical reference MIP image (acquired at 800 nm wavelength). **(B)** OA signal intensity traces from the positions indicated by circles in **(A)**. Note the indicated delay Δt_v between the ICG appearance in a lateral vein versus the tumor area. **(C)** MIP images of the unmixed distribution of AF750 (green) superimposed onto an anatomical OA reference image of the entire kidney region at 850 nanometer. 10 nanomol was of the agent was injected into the tail-vein at 0 seconds. **(D)** Box plots showing the OA signal values over time in the corresponding volumes of interest labeled in **(C)**. From [177].

(Figure IV.16B, red curve). The analysis yielded an average decay rate of 0.55 per minute. In a second calculation, the corresponding signal increase rate in a region of interest located in the liver area (Figure IV.16B, green curve) was determined to equal 0.31 per minute. This value may serve as an additional reference for the liver clearance rate and hepatic function [245]. Furthermore, the delay of $\Delta t_v = 1.26$ seconds in contrast agent appearance in a major lateral vein (Figure IV.16B, blue curve) versus the tumor area, most likely is an indication of vein obstruction caused by the tumor. Finally, an OA MIP image series representing the longitudinal tumor development over 11 days post inoculation superimposed to a whole-body anatomical image is shown in (Figure IV.17). This data may be utilized to make substantial contributions in understanding the anatomical transformations at the different stages of tumor progression, including blockage of the lateral vein, which has probably caused the measured changes in the ICG kinetics.

IV.4.3.3 Longitudinal Dynamics at the Whole Organ Level

Finally, the ability of the proposed approach, to resolve slower pharmacokinetics and longitudinal dynamics at the whole organ level is demonstrated. Technically, the time series of the reconstructed volumes of the spectrally unmixed pressure signals acquired from the kidney region (see Figure IV.16C-D and Figure IV.18) represent a time-average of the spatial distribution of the contrast agent due to the non-neglectable scanning time. Nevertheless, renal clearing of small-molecule occurs on timescales of minutes, which is of the same order of magnitude of the acquisition time. Thus, it is possible to derive meaningful clearance profiles in the kidneys by

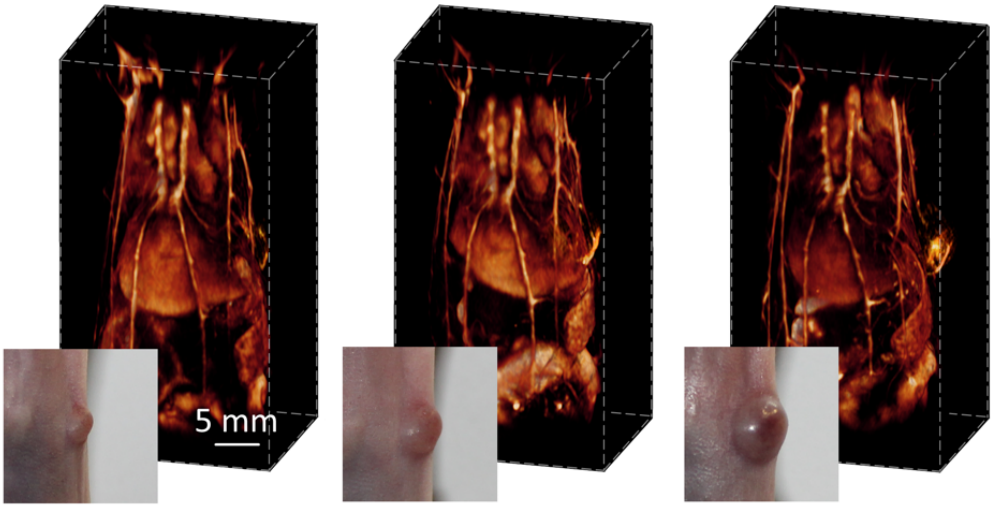

Figure IV.17: Volumetric OA MIP views of the whole-body anatomical images for 800 nanometer excitation wavelength acquired 6, 8 and 11 days after injection of 5×10^5 4T1 murine breast cancer cells into the thoracic mammary fat pad. Photographs of the tumor taken after the imaging experiments are also shown. From [177].

considering the unmixed distribution of AF750, obtained from the OA signal measurements of the larger kidney region. Specifically, three regions, which are color-marked in Figure IV.16C, were further investigated by box-plotting (see Figure IV.16D) their average signal intensity at the available time instances. Analysis of the signal profiles using the same mono-compartment pharmacokinetic model as before (see Section A.1) reveals that the amount of contrast agent in the renal artery (Figure IV.16D, plotted in blue) rapidly increases to a maximum value within 5 minutes post injection, before rapidly decaying at a rate of 0.094 per minute (see Appendix A), whereas the corresponding clearance in the kidney cortex area (Figure IV.16D, plotted in red) was much slower (0.026 per minute). The third region corresponds to the renal pelvis (Figure IV.16D, plotted in green) and AF750 is eliminated towards the ureter. Here, the signal only increases 5 minutes post-injection before reaching a plateau. The observed clearing dynamic is consistent with the normal clearance behavior of the renal system, which includes infiltration of small molecules through the renal artery, filtration in the cortex and subsequent excretion towards the ureter.

IV.4.4 Conclusion

A similar version of the following paragraph (Subsection IV.4.2) was originally published in [177]. In summary, it was shown that the proposed system is capable of delivering high-resolution imaging performance in living mice across multiple spatio-temporal scales. Other commonly adopted imaging modalities, in contrast, demand the integration of data acquired from different systems or alternatively exploit a complementary modality with a different contrast to enable imaging at multiple spatio-temporal scales. For example, in cardiac imaging, the high temporal resolution achieved by modern US scanners can partially complement the advantage in spatial resolution and whole-body imaging capability achieved by high-field MRI scanners [246]. Nevertheless, those hybrid approaches are often associated with limiting trade-offs such as image acquisition time and effective field of view achieved with each of the individual systems [236]. In conclusion, the performed experiments have demonstrated a wide range of

multi-scale imaging capabilities, ranging from volumetric visualization of a beating mouse heart at 100 Hz frame rate to contrast agent kinetics in confined regions at the entire renal system level to whole-body longitudinal studies of tumor growth with unprecedented image quality.

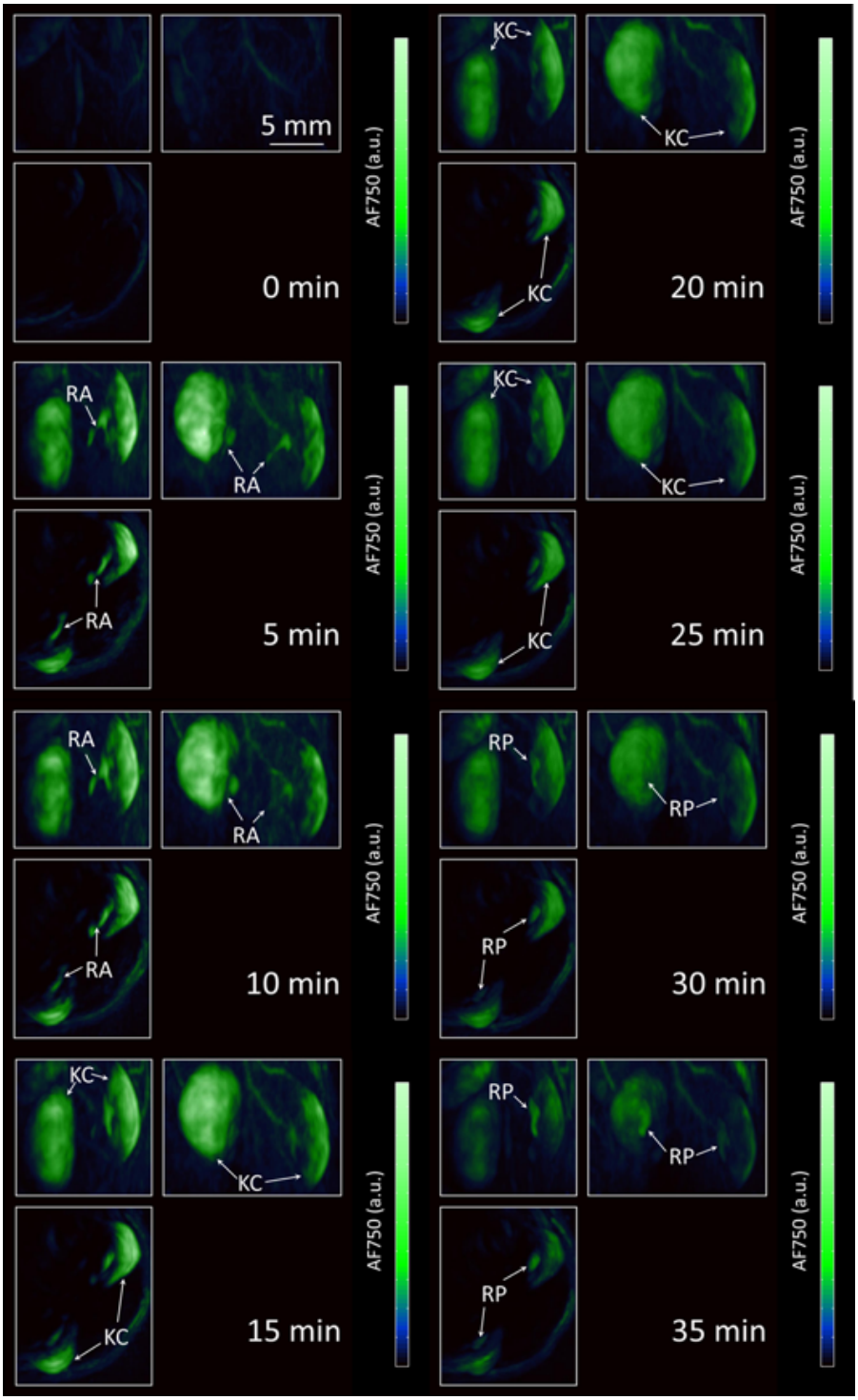

Figure IV.18: OA MIP images along the x, y and z-direction of the multispectrally-unmixed distribution of AF750 after tail-vein injection of 10 nanomol at $t = 0$ seconds. RA: Renal artery, KC: Kidney cortex, RP: Renal pelvis. From [177].

V Summary & Conclusion

V.1 Summary

Chapter II commenced with a description of the circumstances that led to the initial discovery of the OA effect by Bell and subsequently laid out the historical development of OA imaging, beginning with its initial application to the spectral characterization of materials until its modern application as biomedical imaging modality. The rapid development of acoustic detection and laser technology as well as GPUs now allows for real-time MS OA imaging of biological structures ranging from a couple of microns to small animal whole-body imaging. The section continued with an introduction to the three common OA imaging configurations i.e. Optoacoustic Microscopy, Optoacoustic Endoscopy and Optoacoustic Tomography, followed by a discussion of their application in biomedical research. Further, the concept of MS OA imaging was explained and the most important intrinsic chromophores for biomedical imaging, hemoglobin and melanin were introduced, followed by a discussion of the concept of contrast agent-based imaging. Section II.1 of Chapter II concluded with a discussion of the fluence problem in MS OA imaging and its impact on quantitative imaging. The chapter continued with a detailed motivation of the conducted research in Section II.2. The presentation commenced with an elaborate discussion of two main trends in volumetric OT imaging i.e. the accelerated transitioning of OA imaging into the clinic through hybridization with US as well as the development of small animal OA imaging systems. Subsequently, the limitations of the current state of the art technology were identified and their consequences were discussed. The section continued with the definition of the thesis objectives i.e. the development of two novel volumetric OT systems for imaging of multi-scale dynamics. The last section of Chapter II was dedicated to the mathematical background of OA. The OA equation was motivated, its solution was derived, reconstruction strategies were discussed and the concept of spectral unmixing was introduced.

In Chapter III, two novel multi-scale US & OA imaging methods were developed. In Section III.1, the hybrid US and OA hand-held imaging device based on passive element optical excitation was introduced. The presentation included a detailed discussion of the employed method, the image reconstruction algorithm as well as multiple phantom experiments to characterize the imaging performance of the system. Section III.2 was concerned with the development of a new generation of in-vivo whole-body OA scanner with real-time capacity. The system design was introduced, algorithms for motion-corrected image reconstruction were elaborated and the imaging performance of the system was characterized through phantom experiments. Eventually, a full-body scans of mice were shown.

Chapter IV was dedicated to the application of OA tomography configuration to image multi-

scale dynamics. In Section IV.1, the proposed hybrid imaging method from Section III.1 was successfully utilized to resolve a newly developed dual-modality contrast agents in phantoms and in-vivo mouse experiments as well as to image a human finger thus validating its applicability in biomedical research and clinical diagnosis. Eventually, the developed hybrid system was utilized for accurate positioning of a laser catheter and lesion progression monitoring in a ELT study (Section IV.2). In Section IV.3 of Chapter IV, a MS volumetric OA tomography approach was utilized to resolve hemodynamic changes in the whole mouse brain with high spatio-temporal resolution. In a first step, it was shown, for the first time, that the proposed approach enables to determine Blood Oxygenation, Total Hemoglobin, Cerebral Blood Volume as well as Oxygenized Hemoglobin and Deoxygenized Hemoglobin non-invasively and in real-time. In a second set of experiments, the developed method was then applied to map the onset, spread, and termination of epileptic seizures in a mouse brain. Specifically, it was demonstrated that the proposed system allows to resolve thalamo-cortical activity synchronized to concurrent electrophysiological recordings during chemically-induced seizures. Finally, the imaging performance of the newly developed small animal scanner, introduced in Section IV.4, was demonstrated by visualizing multi-scale dynamics in mice in-vivo. The real-time imaging capacity was exploited to resolve the cardiac cycle in a mouse heart at 100 volumetric frames per second. The unprecedented temporal resolution combined with the injection of an external contrast agent further allowed to segment the heart chambers based on the distribution dynamic of the agent. In addition, the capacity of the proposed system to resolve contrast agent kinetics was demonstrated by determination of clearance rates of such in a organ as well as in a tumor. Finally, the capacity of the system to image longitudinal dynamics at the whole organ system level is showcased by determining the clearance profile of an external contrast agent in a mouse kidney.

V.2 Conclusion

OA imaging is characterized by its operational simplicity, its comparatively low hardware complexity and its ability to deliver volumetric real-time images at high spatio-temporal resolution. OA has been applied in many fields of fundamental research and it is now translated into the clinical routine with more and more medical applications emerging. Future research will be dedicated to continue miniaturization of laser and data acquisition hardware, thus making OA imaging even more portable. However, important problems such as the influence of wavelength-dependent light fluence remain subject to ongoing research and need to be addressed before OA is able to deliver quantitative imaging data.

The methods that were developed in this thesis carry great potential for the advancement of OA imaging. For the first time, a hybrid US and OA imaging system capable of delivering volumetric real-time images was showcased in this thesis. The demonstrated volumetric imaging speed, the hand-held capacity and the synergetic combination of OA and US will lead to powerful new applications in biomedical and clinical research. Future efforts will be directed to the development of a compact system design, where the passive element is integrated into the OA imaging probe. Furthermore, the developed small-animal scanner offers significant advantages over existing imaging approaches. Due to the unique feasibility of rendering high-quality whole-body images combined with coregistered real-time sequences of specific regions will pave the way for unprecedented applications in small animal research, thus establishing OA as the imaging technology of choice in many important biological studies.

The experiments performed in this thesis clearly demonstrate the impact of the developed methods. The volumetric imaging capacity of the real-time hybrid US and OA imaging system

was validated in multiple imaging scenarios. It was demonstrated that the proposed approach is capable of delivering hybrid three-dimensional images of phantoms as well as biological tissue such as a mouse heart or a human finger. It was further shown that the system carries great potential in allowing physicians to accurately position laser catheters and monitor lesion progression during ELT. Not only will this approach accelerate the integration of OA imaging into the treatment routine but it is also expected that the presented approach greatly improves clinical outcomes.

It was further demonstrated that MS real-time OA tomography can be effectively used for localization and characterization of epileptic foci in the neocortex and in subcortical structures such as the thalamus. Hence, the proposed approach can further be envisioned to characterize different sensory stimuli like somatosensory paw or whisker stimulations.

Finally, it was shown that the newly developed small animal scanner is capable to deliver high resolution images at the whole-body scale combined with the capability to image smaller regions ultra-fast and in 3D, thus making the proposed system unique among the existing pre-clinical imaging modalities. Moreover, the system offers the powerful contrast advantages of optical imaging, including the ability to visualize functional and molecular information such as blood oxygenation as well as targeted delivery of contrast agents [104].

The presented research contributes substantially to the advancement of OA imaging and it is anticipated that the methods developed in this thesis will accelerate the transition of OA imaging into the clinical routine. Furthermore, it is predicted that the presented results will have a major impact on the evolution of pre-clinical research utilizing small-animal models.

A Appendix

A.1 Estimation of Clearance Constants

The decay and increase rates associated with the concentration of injected contrast agents were estimated by employing a mono-compartment pharmacokinetic model (first order kinetics) [244]. Specifically, the elimination rate of the contrast agent from the blood stream was assumed to be proportional to its concentration in the corresponding vascular structure. Further, was assumed that the temporal profile of the concentration of the contrast agent was proportional to the difference between the time-dependent OA signal and its background level before injection. Thus, the time dynamic of the OA signal intensity at a given location $OA_v(t)$ can be expressed as:

$$OA_v(t) = OA_v(0) + k \left(e^{-t/\tau_1} - e^{-t/\tau_2} \right) \tag{1.1}$$

The term e^{-t/τ_2} was included to account for the fact that time is required for the contrast agent to uniformly distribute in the blood stream. The decay rate of the concentration of the contrast agent at a given location is then given by the time parameter τ_1. The decay rates of AF750 in the renal artery and the kidney cortex as well as the decay rate of ICG in the tumor area were estimated by fitting the time traces of the OA intensity signals to Equation 1.1. Different values for τ_1 in different regions indicate that elimination of the contrast agent from the blood stream is basded on a different physiological process. For example, AF750 is eliminated from the renal pelvis to the kidney cortex and from the kidney cortex capillaries to the renal pelvis. In contrast, the decay rate in the tumor region results from a combination of various effects such as ICG leakage into the extracellular matrix due to enhanced permeability and retention (EPR) effect [247] as well as its clearance from the blood circulation through other organs.

The accumulation rate of ICG in the liver was estimated with the same model. Assuming that ICG is eliminated from the blood stream according to Equation 1.1, the OA signal intensity in the liver $OA_l(t)$ due to accumulation of the contrast agent can be calculated by integrating Equation 1.1. Assuming that $\tau_1 \gg \tau_2$ then yields:

$$OA_l(t) = OA_l(0) + k\,\tau_1 \left(1 - e^{-t/\tau_1} \right) \tag{1.2}$$

The time parameter τ_1 is yielded by fitting the time profile of the OA signal to Equation 1.2 and can be interpreted as the rate of ICG increase in the liver.

A.2 Blood Flow Velocity Estimation

The blood flow velocity can be estimated from the difference in the onset of ICG signal intensity in the bolus. Clearly, this demands that the flow velocity is significantly slower than the acquisition rate of OA signals. The delay was estimated by first applying an 80-point moving average filter to the time trace signals, which were subsequently normalized to their maximum and minimum values. In the next step, the normalized signals were fitted to a 5^{th} order polynomial, whereas only the time intervals inside the dashed rectangles in Figure IV.15b and Figure IV.16b were considered. The individual delays marked in Figure IV.15b and Figure IV.16b are determined, when the value of the fitted polynomials equal 0.5. The delay Δt_{ca} between the ICG bolus appearance at the thoracic artery and the coronary artery was further used to estimate the blood flow velocity in the coronary artery. Considering that the selected point in the coronary artery is located at a distance $d = 3$ mm from the aortic branch, the flow velocity v was approximated via $v = d/\Delta t_{ca}$.

A.3 Supplementary Figures

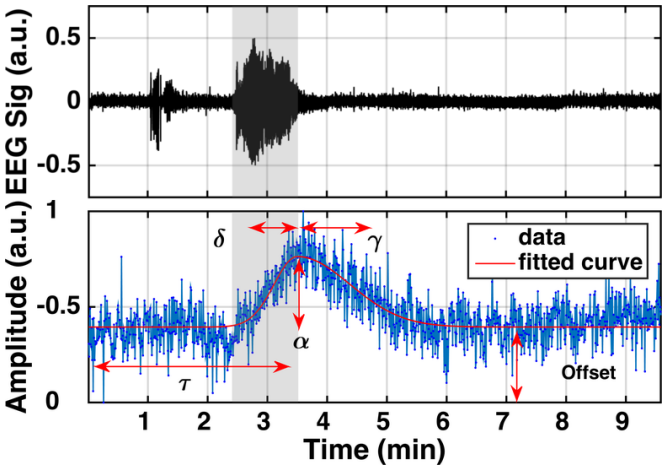

Figure A.1: Model employed to identify active voxels. Top: EEG as it was measured during one of the experiments. Periods of epileptic seizures can clearly be identified (grey area) over background signals. Bottom: Explanation of the parameters used to model the OHRF. From [101].

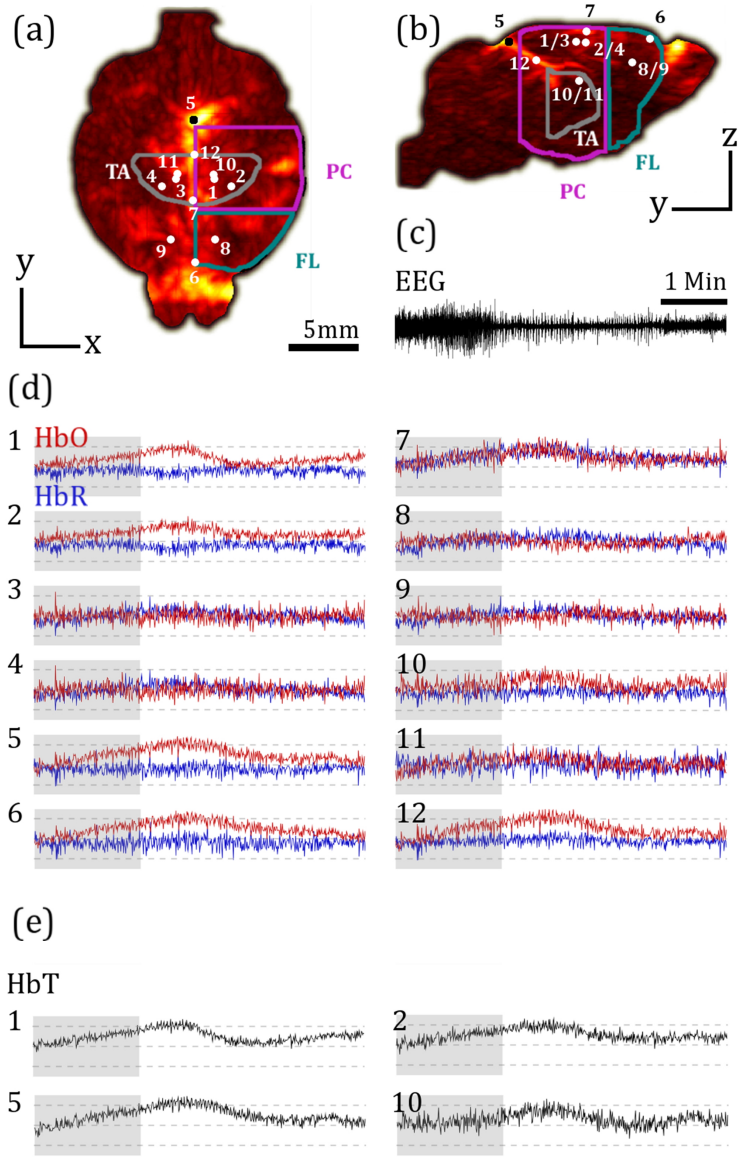

Figure A.2: Analysis of hemodynamic changes during epileptic seizures in an independent experiment. **(a)** Transversal MIP image of the HbO distribution in the mouse brain. Analyzed voxels are indicated and correspond to plotted time traces in **(d)**. Colored outlines specify the location of brain regions (grey: TA; purple: PC; green: FL). **(b)** Coronal MIP view of **(a)**. **(c)** Plot of the time trace of the EEG. **(d)** Time traces of HbO (in red) and HbR (in blue) in the voxels shown in **(a)** and **(b)** are plotted. Grey boxes indicate the length of the seizure-associated neural activity as seen in the EEG. Dotted grey lines indicate averaged baseline and +/-50% relative changes for each curve. (e) The HbT was calculated from the signal intensities as the sum of HbO and HbR. HbT curves are only plotted for voxels with changes bigger than the background noise. The analyzed regions encompass the side of the brain where 4-AP was injected and respective voxels in the cl side of the brain and inside major draining veins: Injection site (1, 2) and (cl: 3, 4); SSS (6, 7); CS (5); LHV (12); voxels anterior to the injection site (8, cl: 9); TA (10, cl: 11). From [101].

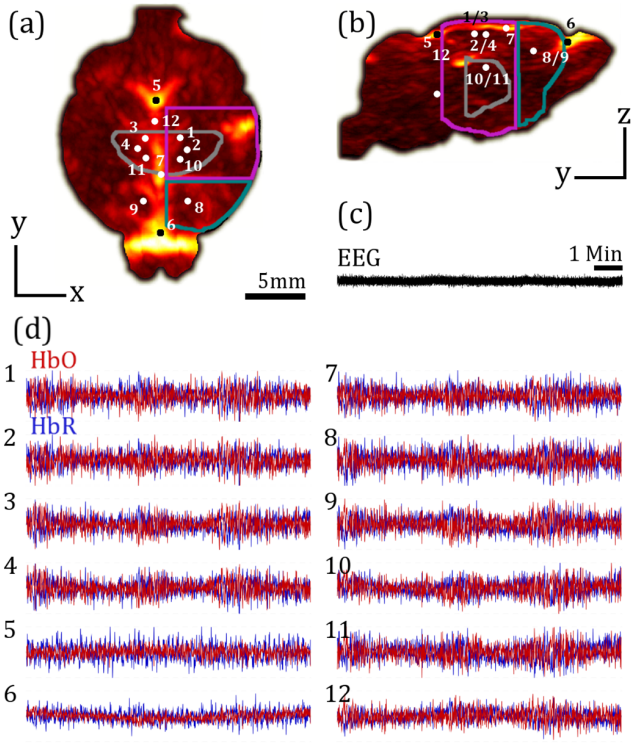

Figure A.3: Voxel analysis of hemodynamic changes during typical background neural activity without epileptic seizures. **(a)** MIP along the transversal direction of HbO distribution in the mouse brain. Analyzed voxels are indicated and correspond to curves plotted in **(c)**. Colored outlines specify the location of brain regions (grey: TA; purple: PC; green: FL). **(b)** Coronal MIP view similar to **(a)**. **(c)** Plot of the EEG time trace. **(d)** Time traces of HbO (in red) and HbR (in blue) in the voxels shown in **(a)** and **(b)** are plotted. For a detailed description of the voxel positions see Figure A.2. From [101].

Bibliography

[1] A. G. Bell, 'On the production and reproduction of sound by light', *American Journal of Science* (1880), 305–324.

[2] A. G. Bell, 'Production of Sound by Radiant Energy', *The Manufacturer and Builder* **13** (1881), 156–158.

[3] J. Tyndall, 'Action of an intermittent beam of radiant heat upon gaseous matter', *Proceedings of the Royal Society of London* **31** (1880), 307–317.

[4] W. C. Röntgen, 'On tones produced by the intermittent irradiation of a gas', *Philosophical Magazine Series 5* **11** (1881), 308–311.

[5] M. Viengerov, 'New method of gas analysis based on tyndall-roentgen optoacoustic effect', *Doklady Akademii Nauk SSSR* **19** (1938), 8.

[6] A. Mandelis, ed., *Progress in Photothermal & Photoacoustic Science & Technology*, Elsevier Science Ltd, 1992.

[7] A. Rosencwaig, *Photoacoustics and photoacoustic spectroscopy*, Wiley, 1980.

[8] V. E. Gusev, *Laser optoacoustics*, Amer Inst of Physics, 1993.

[9] J. McClelland, R. Jones, S. Bajic, J. Chalmers and P. Griffiths, *Handbook of vibrational spectroscopy*, John Wiley & Sons, Ltd, 2002.

[10] K. Dussik, 'On the possibility of using ultrasound waves as a diagnostic aid', *Neurol Psychiat* **174** (1942), 153–168.

[11] S. L and T. H, *Masers and maser communications system*, US Patent 2,929,922, 1960.

[12] T. Bowen, 'Radiation-induced thermoacoustic soft tissue imaging', *1981 Ultrasonics Symposium* (1981), 817–822.

[13] R. A. Kruger, P. Liu, C. R. Appledorn et al., 'Photoacoustic ultrasound (PAUS)—reconstruction tomography', *Medical physics* **22** (1995), 1605–1609.

[14] A. A. Oraevsky, 'Opto-acoustic tomography of deeply embedded tumors and early subsurface lesions', *Biomedical Topical Meeting*, Optical Society of America, 1999, AMD1.

[15] X. Wang, Y. Pang, G. Ku, X. Xie, G. Stoica and L. V. Wang, 'Noninvasive laser-induced photoacoustic tomography for structural and functional in vivo imaging of the brain', *Nature biotechnology* **21** (2003), 803–806.

[16] C. Patel and A. Tam, 'Pulsed optoacoustic spectroscopy of condensed matter', *Reviews of Modern Physics* **53** (1981), 517.

[17] G. A. West, J. J. Barrett, D. R. Siebert and K. V. Reddy, 'Photoacoustic spectroscopy', *Review of Scientific Instruments* **54** (1983), 797–817.

[18] D. Hutchins, A. C. Tam et al., 'Pulsed photoacoustic materials characterization', *Ultrasonics, Ferroelectrics, and Frequency Control, IEEE Transactions on* **33** (1986), 429–449.

[19] M. W. Sigrist, 'Laser generation of acoustic waves in liquids and gases', *Journal of applied physics* **60** (1986), R83–R122.

[20] K. Maslov and L. V. Wang, 'Photoacoustic imaging of biological tissue with intensity-modulated continuous-wave laser', *Journal of biomedical optics* **13** (2008), 024006–024006.

[21] A. M. Smith, M. C. Mancini and S. Nie, 'Bioimaging: second window for in vivo imaging', *Nature nanotechnology* **4** (2009), 710–711.

[22] G. M. Hale and M. R. Querry, 'Optical constants of water in the 200-nm to 200-μm wavelength region', *Applied optics* **12** (1973), 555–563.

[23] L. V. Wang and S. Hu, 'Photoacoustic tomography: in vivo imaging from organelles to organs', *Science* **335** (2012), 1458–1462.

[24] G. Ku, X. Wang, G. Stoica and L. V. Wang, 'Multiple-bandwidth photoacoustic tomography', *Physics in medicine and biology* **49** (2004), 1329.

[25] L. V. Wang, 'Tutorial on photoacoustic microscopy and computed tomography', *Selected Topics in Quantum Electronics, IEEE Journal of* **14** (2008), 171–179.

[26] M. Xu and L. V. Wang, 'Photoacoustic imaging in biomedicine', *Review of scientific instruments* **77** (2006), 041101.

[27] D. Razansky, M. Distel, C. Vinegoni, R. Ma, N. Perrimon, R. W. Köster and V. Ntziachristos, 'Multispectral opto-acoustic tomography of deep-seated fluorescent proteins in vivo', *Nature Photonics* **3** (2009), 412–417.

[28] X. L. Deán-Ben and D. Razansky, 'Adding fifth dimension to optoacoustic imaging: volumetric time-resolved spectrally enriched tomography', *Light: Science & Applications* **3** (2014), e137.

[29] V. Ntziachristos, 'Going deeper than microscopy: the optical imaging frontier in biology', *Nature methods* **7** (2010), 603–614.

[30] L. V. Wang and H.-i. Wu, *Biomedical optics: principles and imaging*, John Wiley & Sons, 2012.

[31] V. Ntziachristos and D. Razansky, 'Molecular imaging by means of multispectral optoacoustic tomography (MSOT)', *Chemical reviews* **110** (2010), 2783–2794.

[32] L. E. Larsen and J. H. Jacobi, *Medical applications of microwave imaging*, tech. rep., DTIC Document, 1985.

[33] X. L. Deán-Ben, D. Razansky and V. Ntziachristos, 'The effects of acoustic attenuation in optoacoustic signals', *Physics in medicine and biology* **56** (2011), 6129.

[34] B. Cox, J. G. Laufer, S. R. Arridge and P. C. Beard, 'Quantitative spectroscopic photoacoustic imaging: a review', *Journal of biomedical optics* **17** (2012), 0612021–06120222.

[35] L. V. Wang, *Photoacoustic imaging and spectroscopy*, CRC press, 2009.

[36] L. V. Wang, 'Multiscale photoacoustic microscopy and computed tomography', *Nature photonics* **3** (2009), 503–509.

[37] R. Weissleder and V. Ntziachristos, 'Shedding light onto live molecular targets', *Nature medicine* **9** (2003), 123–128.

[38] A. Taruttis and V. Ntziachristos, 'Advances in real-time multispectral optoacoustic imaging and its applications', *Nature Photonics* **9** (2015), 219–227.

[39] L. V. Wang, X. Zhao, H. Sun and G. Ku, 'Microwave-induced acoustic imaging of biological tissues', *Review of Scientific Instruments* **70** (1999), 3744–3748.

[40] H. F. Zhang, K. Maslov, G. Stoica and L. V. Wang, 'Functional photoacoustic microscopy for high-resolution and noninvasive in vivo imaging', *Nature biotechnology* **24** (2006), 848–851.

[41] H. Estrada, J. Turner, M. Kneipp and D. Razansky, 'Real-time optoacoustic brain microscopy with hybrid optical and acoustic resolution', *Laser Physics Letters* **11** (2014), 045601.

[42] K. Maslov, H. F. Zhang, S. Hu and L. V. Wang, 'Optical-resolution photoacoustic microscopy for in vivo imaging of single capillaries', *Optics letters* **33** (2008), 929–931.

[43] C. P. Favazza, O. Jassim, L. A. Cornelius and L. V. Wang, 'In vivo photoacoustic microscopy of human cutaneous microvasculature and a nevus', *Journal of biomedical optics* **16** (2011), 016015–016015.

[44] S. Oladipupo, S. Hu, J. Kovalski, J. Yao, A. Santeford, R. E. Sohn, R. Shohet, K. Maslov, L. V. Wang and J. M. Arbeit, 'VEGF is essential for hypoxia-inducible factor-mediated neovascularization but dispensable for endothelial sprouting', *Proceedings of the National Academy of Sciences* **108** (2011), 13264–13269.

[45] S. S. Oladipupo, S. Hu, A. C. Santeford, J. Yao, J. R. Kovalski, R. V. Shohet, K. Maslov, L. V. Wang and J. M. Arbeit, 'Conditional HIF-1 induction produces multistage neovascularization with stage-specific sensitivity to VEGFR inhibitors and myeloid cell independence', *Blood* **117** (2011), 4142–4153.

[46] M.-L. Li, J.-T. Oh, X. Xie, G. Ku, W. Wang, C. Li, G. Lungu, G. Stoica and L. V. Wang, 'Simultaneous molecular and hypoxia imaging of brain tumors in vivo using spectroscopic photoacoustic tomography', *Proceedings of the IEEE* **96** (2008), 481–489.

[47] S.-L. Chen, T. Ling, S.-W. Huang, H. Won Baac and L. J. Guo, 'Photoacoustic correlation spectroscopy and its application to low-speed flow measurement', *Optics letters* **35** (2010), 1200–1202.

[48] X. Wang, G. Ku, M. A. Wegiel, D. J. Bornhop, G. Stoica and L. V. Wang, 'Noninvasive photoacoustic angiography of animal brains in vivo with near-infrared light and an optical contrast agent', *Optics letters* **29** (2004), 730–732.

[49] S. Hu, K. Maslov, V. Tsytsarev and L. V. Wang, 'Functional transcranial brain imaging by optical-resolution photoacoustic microscopy', *Journal of biomedical optics* **14** (2009), 040503–040503.

[50] V. Tsytsarev, S. Hu, J. Yao, K. Maslov, D. L. Barbour and L. V. Wang, 'Photoacoustic microscopy of microvascular responses to cortical electrical stimulation', *Journal of biomedical optics* **16** (2011), 076002–076002.

[51] A. Taruttis, E. Herzog, D. Razansky and V. Ntziachristos, 'Real-time imaging of cardiovascular dynamics and circulating gold nanorods with multispectral optoacoustic tomography', *Optics express* **18** (2010), 19592–19602.

[52] C. Zhang, K. Maslov and L. V. Wang, 'Subwavelength-resolution label-free photoacoustic microscopy of optical absorption in vivo', *Optics letters* **35** (2010), 3195–3197.

[53] R. J. Zemp, L. Song, R. Bitton, K. K. Shung and L. V. Wang, 'Realtime photoacoustic microscopy in vivo with a 30-MHz ultrasound array transducer', *Optics express* **16** (2008), 7915–7928.

[54] J. Yao and L. V. Wang, 'Photoacoustic microscopy', *Laser & photonics reviews* **7** (2013), 758–778.

[55] P. Beard, 'Biomedical photoacoustic imaging', *Interface focus* (2011), rsfs20110028.

[56] C. Kim, C. Favazza and L. V. Wang, 'In vivo photoacoustic tomography of chemicals: high-resolution functional and molecular optical imaging at new depths', *Chemical reviews* **110** (2010), 2756–2782.

[57] B. Wang, E. Yantsen, T. Larson, A. B. Karpiouk, S. Sethuraman, J. L. Su, K. Sokolov and S. Y. Emelianov, 'Plasmonic intravascular photoacoustic imaging for detection of macrophages in atherosclerotic plaques', *Nano Letters* **9** (2008), 2212–2217.

[58] J.-M. Yang, C. Favazza, R. Chen, J. Yao, X. Cai, K. Maslov, Q. Zhou, K. K. Shung and L. V. Wang, 'Toward dual-wavelength functional photoacoustic endoscopy: laser and peripheral optical systems development', *SPIE BiOS*, International Society for Optics and Photonics, 2012, pp. 822316–822316.

[59] J.-M. Yang, K. Maslov, H.-C. Yang, Q. Zhou, K. K. Shung and L. V. Wang, 'Photoacoustic endoscopy', *Optics letters* **34** (2009), 1591–1593.

[60] T.-J. Yoon and Y.-S. Cho, 'Recent advances in photoacoustic endoscopy', *World journal of gastrointestinal endoscopy* **5** (2013), 534.

[61] C. Li, J.-M. Yang, R. Chen, Y. Zhang, Y. Xia, Q. Zhou, K. K. Shung and L. V. Wang, 'Photoacoustic endoscopic imaging study of melanoma tumor growth in a rat colorectum in vivo', *SPIE BiOS*, International Society for Optics and Photonics, 2013, pp. 85810D–85810D.

[62] J.-M. Yang, C. Favazza, R. Chen, J. Yao, X. Cai, K. Maslov, Q. Zhou, K. K. Shung and L. V. Wang, 'Simultaneous functional photoacoustic and ultrasonic endoscopy of internal organs in vivo', *Nature Medicine* **18** (2012), 1297–1302.

[63] J. M. Yang, C. Favazza, J. Yao, R. Chen, Q. Zhou, K. K. Shung and L. V. Wang, 'Three-dimensional photoacoustic endoscopic imaging of the rabbit esophagus', *PLoS ONE* **10** (2015) .

[64] J.-M. Yang, R. Chen, C. Favazza, J. Yao, C. Li, Z. Hu, Q. Zhou, K. K. Shung and L. V. Wang, 'A 2.5-mm diameter probe for photoacoustic and ultrasonic endoscopy', *Optics express* **20** (2012), 23944–23953.

[65] X. Wang, X. Xie, G. Ku, L. V. Wang and G. Stoica, 'Noninvasive imaging of hemoglobin concentration and oxygenation in the rat brain using high-resolution photoacoustic tomography', *Journal of biomedical optics* **11** (2006), 024015–024015.

[66] R. A. Kruger, W. L. Kiser Jr, D. R. Reinecke and G. A. Kruger, 'Thermoacoustic computed tomography using a conventional linear transducer array', *Medical physics* **30** (2003), 856–860.

[67] E. Zhang, J. Laufer, R. Pedley and P. Beard, 'In vivo high-resolution 3D photoacoustic imaging of superficial vascular anatomy', *Physics in medicine and biology* **54** (2009), 1035.

[68] R. A. Kruger, W. L. Kiser, D. R. Reinecke, G. A. Kruger and K. D. Miller, 'Thermoacoustic molecular imaging of small animals', *Molecular Imaging* **2** (2003), 113–123.

[69] R. Ma, A. Taruttis, V. Ntziachristos and D. Razansky, 'Multispectral optoacoustic tomography (MSOT) scanner for whole-body small animal imaging', *Optics express* **17** (2009), 21414–21426.

[70] X. L. Deán-Ben and D. Razansky, 'Portable spherical array probe for volumetric real-time optoacoustic imaging at centimeter-scale depths', *Optics express* **21** (2013), 28062–28071.

[71] R. A. Kruger, R. B. Lam, D. R. Reinecke, S. P. Del Rio and R. P. Doyle, 'Photoacoustic angiography of the breast', *Medical physics* **37** (2010), 6096–6100.

[72] M. Xu and L. V. Wang, 'Universal back-projection algorithm for photoacoustic computed tomography', *Biomedical Optics 2005*, International Society for Optics and Photonics, 2005, pp. 251–254.

[73] X. L. Dean-Ben, A. Ozbek and D. Razansky, 'Volumetric real-time tracking of peripheral human vasculature with GPU-accelerated three-dimensional optoacoustic tomography', *Medical Imaging, IEEE Transactions on* **32** (2013), 2050–2055.

[74] X. L. Deán-Ben and D. Razansky, 'Functional optoacoustic human angiography with handheld video rate three dimensional scanner', *Photoacoustics* **1** (2013), 68–73.

[75] A. Buehler, M. Kacprowicz, A. Taruttis and V. Ntziachristos, 'Real-time handheld multispectral optoacoustic imaging', *Optics letters* **38** (2013), 1404–1406.

[76] M. Schwarz, A. Buehler, J. Aguirre and V. Ntziachristos, 'Three-dimensional multispectral optoacoustic mesoscopy reveals melanin and blood oxygenation in human skin in vivo', *Journal of biophotonics* (2015) .

[77] Y. Zhou, G. Li, L. Zhu, C. Li, L. A. Cornelius and L. V. Wang, 'Handheld photoacoustic probe to detect both melanoma depth and volume at high speed in vivo', *Journal of biophotonics* **9999** (2015) .

[78] C. Kim, T. N. Erpelding, K. Maslov, L. Jankovic, W. J. Akers, L. Song, S. Achilefu, J. A. Margenthaler, M. D. Pashley and L. V. Wang, 'Handheld array-based photoacoustic probe for guiding needle biopsy of sentinel lymph nodes', *Journal of biomedical optics* **15** (2010), 046010–046010.

[79] X. L. Deán-Ben, T. F. Fehm, M. Gostic and D. Razansky, 'Volumetric hand-held optoacoustic angiography as a tool for real-time screening of dense breast', *Journal of biophotonics* (2015) .

[80] X. Deán-Ben, T. F. Fehm and D. Razansky, 'Universal hand-held three-dimensional optoacoustic imaging probe for deep tissue human angiography and functional preclinical studies in real time', *JoVE (Journal of Visualized Experiments)* (2014), e51864–e51864.

[81] R. Nuster, N. Schmitner, G. Wurzinger, S. Gratt, W. Salvenmoser, D. Meyer and G. Paltauf, 'Hybrid photoacoustic and ultrasound section imaging with optical ultrasound detection', *J Biophotonics* **6** (2013), 549–559.

[82] E. Merčep, G. Jeng, S. Morscher, P.-C. Li and D. Razansky, 'Hybrid optoacoustic tomography and pulse-echo ultrasonography using concave arrays', *Ultrasonics, Ferroelectrics, and Frequency Control, IEEE Transactions on* **62** (2015), 1651–1661.

[83] J. J. Niederhauser, M. Jaeger, R. Lemor, P. Weber and M. Frenz, 'Combined ultrasound and optoacoustic system for real-time high-contrast vascular imaging in vivo', *Medical Imaging, IEEE Transactions on* **24** (2005), 436–440.

[84] H. Yang, L. Xi, S. Samuelson, H. Xie, L. Yang and H. Jiang, 'Handheld miniature probe integrating diffuse optical tomography with photoacoustic imaging through a MEMS scanning mirror', *Biomedical optics express* **4** (2013), 427–432.

[85] J. Xia, M. R. Chatni, K. Maslov, Z. Guo, K. Wang, M. Anastasio and L. V. Wang, 'Whole-body ring-shaped confocal photoacoustic computed tomography of small animals in vivo', *Journal of biomedical optics* **17** (2012), 0505061–0505063.

[86] H.-P. Brecht, R. Su, M. Fronheiser, S. A. Ermilov, A. Conjusteau and A. A. Oraevsky, 'Whole-body three-dimensional optoacoustic tomography system for small animals', *Journal of biomedical optics* **14** (2009), 064007–064007.

[87] J. Gateau, M. Á. A. Caballero, A. Dima and V. Ntziachristos, 'Three-dimensional optoacoustic tomography using a conventional ultrasound linear detector array: whole-body tomographic system for small animals', *Medical physics* **40** (2013), 013302.

[88] A. A. Oraevsky, A. A. Karabutov, S. V. Solomatin, E. V. Savateeva, V. A. Andreev, Z. Gatalica, H. Singh and R. D. Fleming, 'Laser optoacoustic imaging of breast cancer in vivo', *BiOS 2001 The International Symposium on Biomedical Optics*, International Society for Optics and Photonics, 2001, pp. 6–15.

[89] S. Manohar, S. E. Vaartjes, J. C. van Hespen, J. M. Klaase, F. M. van den Engh, W. Steenbergen and T. G. Van Leeuwen, 'Initial results of in vivo non-invasive cancer imaging in the human breast using near-infrared photoacoustics', *Optics express* **15** (2007), 12277–12285.

[90] A. Taruttis, G. M. van Dam and V. Ntziachristos, 'Mesoscopic and Macroscopic Optoacoustic Imaging of Cancer', *Cancer research* **75** (2015), 1548–1559.

[91] M. Mehrmohammadi, S. J. Yoon, D. Yeager and S. Y. Emelianov, 'Photoacoustic imaging for cancer detection and staging', *Current molecular imaging* **2** (2013), 89.

[92] A. Taruttis, M. Wildgruber, K. Kosanke, N. Beziere, K. Licha, R. Haag, M. Aichler, A. Walch, E. Rummeny and V. Ntziachristos, 'Multispectral optoacoustic tomography of myocardial infarction', *Photoacoustics* **1** (2013), 3–8.

[93] A. Berlis, H. Lutsep, S. Barnwell, A. Norbash, L. Wechsler, C. A. Jungreis, A. Woolfenden, G. Redekop, M. Hartmann and M. Schumacher, 'Mechanical thrombolysis in acute ischemic stroke with endovascular photoacoustic recanalization', *Stroke* **35** (2004), 1112–1116.

[94] S. Gottschalk, T. F. Fehm, X. L. Deán-Ben and D. Razansky, 'Noninvasive real-time visualization of multiple cerebral hemodynamic parameters in whole mouse brains using five-dimensional optoacoustic tomography', *Journal of Cerebral Blood Flow & Metabolism* (2015) .

[95] J. Yao, J. Xia, K. I. Maslov, M. Nasiriavanaki, V. Tsytsarev, A. V. Demchenko and L. V. Wang, 'Noninvasive photoacoustic computed tomography of mouse brain metabolism in vivo', *Neuroimage* **64** (2013), 257–266.

[96] M. Nasiriavanaki, J. Xia, H. Wan, A. Q. Bauer, J. P. Culver and L. V. Wang, 'High-resolution photoacoustic tomography of resting-state functional connectivity in the mouse brain', *Proceedings of the National Academy of Sciences* **111** (2014), 21–26.

[97] I. Stoffels, S. Morscher, I. Helfrich, U. Hillen, J. Lehy, N. C. Burton, T. C. Sardella, J. Claussen, T. D. Poeppel, H. S. Bachmann et al., 'Metastatic status of sentinel lymph nodes in melanoma determined noninvasively with multispectral optoacoustic imaging', *Science Translational Medicine* **7** (2015), 317ra199–317ra199.

[98] C. Lee, J. Kim, Y. Zhang, M. Jeon, C. Liu, L. Song, J. F. Lovell and C. Kim, 'Dual-color photoacoustic lymph node imaging using nanoformulated naphthalocyanines', *Biomaterials* **73** (2015), 142–148.

[99] X. Wang, D. L. Chamberland and D. A. Jamadar, 'Noninvasive photoacoustic tomography of human peripheral joints toward diagnosis of inflammatory arthritis', *Optics letters* **32** (2007), 3002–3004.

[100] J. R. Rajian, X. Shao, D. L. Chamberland and X. Wang, 'Characterization and treatment monitoring of inflammatory arthritis by photoacoustic imaging: a study on adjuvant-induced arthritis rat model', *Biomedical optics express* **4** (2013), 900–908.

[101] S. Gottschalk, T. F. Fehm, X. L. Deán-Ben, V. Tsytsarev and D. Razansky, 'Correlation between volumetric oxygenation responses and electrophysiology identifies deep thalamocortical activity during epileptic seizures', *Neurophotonics* **4** (2017), 011007–011007.

[102] E. Herzog, A. Taruttis, N. Beziere, A. A. Lutich, D. Razansky and V. Ntziachristos, 'Optical imaging of cancer heterogeneity with multispectral optoacoustic tomography', *Radiology* **263** (2012), 461–468.

[103] J.-T. Oh, M.-L. Li, H. F. Zhang, K. Maslov, G. Stoica and L. V. Wang, 'Three-dimensional imaging of skin melanoma in vivo by dual-wavelength photoacoustic microscopy', *Journal of biomedical optics* **11** (2006), 034032–034032.

[104] L. Nie and X. Chen, 'Structural and functional photoacoustic molecular tomography aided by emerging contrast agents', *Chemical Society Reviews* **43** (2014), 7132–7170.

[105] Y.-S. Chen, W. Frey, S. Kim, P. Kruizinga, K. Homan and S. Emelianov, 'Silica-coated gold nanorods as photoacoustic signal nanoamplifiers', *Nano letters* **11** (2011), 348–354.

[106] D. Razansky, A. Buehler and V. Ntziachristos, 'Volumetric real-time multispectral optoacoustic tomography of biomarkers', *Nature protocols* **6** (2011), 1121–1129.

[107] V. Ermolayev, X. L. Dean-Ben, S. Mandal, V. Ntziachristos and D. Razansky, 'Simultaneous visualization of tumour oxygenation, neovascularization and contrast agent perfusion by real-time three-dimensional optoacoustic tomography', *European radiology* (2015), 1–9.

[108] D. Pan, B. Kim, L. V. Wang and G. M. Lanza, 'A brief account of nanoparticle contrast agents for photoacoustic imaging', *Wiley Interdisciplinary Reviews: Nanomedicine and Nanobiotechnology* **5** (2013), 517–543.

[109] A. Agarwal, S. Huang, M. O'Donnell, K. Day, M. Day, N. Kotov and S. Ashkenazi, 'Targeted gold nanorod contrast agent for prostate cancer detection by photoacoustic imaging', *Journal of applied physics* **102** (2007), 064701.

[110] W. Lu, Q. Huang, G. Ku, X. Wen, M. Zhou, D. Guzatov, P. Brecht, R. Su, A. Oraevsky, L. V. Wang et al., 'Photoacoustic imaging of living mouse brain vasculature using hollow gold nanospheres', *Biomaterials* **31** (2010), 2617–2626.

[111] A. De La Zerda, C. Zavaleta, S. Keren, S. Vaithilingam, S. Bodapati, Z. Liu, J. Levi, B. R. Smith, T.-J. Ma, O. Oralkan et al., 'Carbon nanotubes as photoacoustic molecular imaging agents in living mice', *Nature nanotechnology* **3** (2008), 557–562.

[112] A. Krumholz, D. M. Shcherbakova, J. Xia, L. V. Wang and V. V. Verkhusha, 'Multicontrast photoacoustic in vivo imaging using near-infrared fluorescent proteins', *Scientific reports* **4** (2014) .

[113] G. S. Filonov, A. Krumholz, J. Xia, J. Yao, L. V. Wang and V. V. Verkhusha, 'Deep-Tissue Photoacoustic Tomography of a Genetically Encoded Near-Infrared Fluorescent Probe', *Angewandte Chemie* **124** (2012), 1477–1480.

[114] F. Martelli, S. Del Bianco, A. Ismaelli and G. Zaccanti, *Light Propagation Through Biological Tissue and Other Diffusive Media: Theory, Solutions, and Software*, SPIE Publications, 2009.

[115] K. Maslov, H. F. Zhang and L. V. Wang, 'Effects of wavelength-dependent fluence attenuation on the noninvasive photoacoustic imaging of hemoglobin oxygen saturation in subcutaneous vasculature in vivo', *Inverse Problems* **23** (2007), S113.

[116] S. Tzoumas, N. Deliolanis, S. Morscher and V. Ntziachristos, 'Unmixing molecular agents from absorbing tissue in multispectral optoacoustic tomography', *Medical Imaging, IEEE Transactions on* **33** (2014), 48–60.

[117] B. Cox, J. Laufer and P. Beard, 'Quantitative photoacoustic image reconstruction using fluence dependent chromophores', *Biomedical optics express* **1** (2010), 201–208.

[118] S. Tzoumas, A. Nunes, N. C. Deliolanis and V. Ntziachristos, 'Effects of multispectral excitation on the sensitivity of molecular optoacoustic imaging', *Journal of biophotonics* **9999** (2014) .

[119] G. P. Luke, D. Yeager and S. Y. Emelianov, 'Biomedical applications of photoacoustic imaging with exogenous contrast agents', *Annals of biomedical engineering* **40** (2012), 422–437.

[120] R. G. Kolkman, P. J. Brands, W. Steenbergen and T. G. van Leeuwen, 'Real-time in vivo photoacoustic and ultrasound imaging', *Journal of biomedical optics* **13** (2008), 050510–050510.

[121] T. Harrison, J. C. Ranasinghesagara, H. Lu, K. Mathewson, A. Walsh and R. J. Zemp, 'Combined photoacoustic and ultrasound biomicroscopy', *Optics Express* **17** (2009), 22041–22046.

[122] E. Macé, G. Montaldo, I. Cohen, M. Baulac, M. Fink and M. Tanter, 'Functional ultrasound imaging of the brain', *Nature methods* **8** (2011), 662–664.

[123] Y. Zeng, D. Xing, Y. Wang, B. Yin and Q. Chen, 'Photoacoustic and ultrasonic coimage with a linear transducer array', *Optics letters* **29** (2004), 1760–1762.

[124] X. L. Deán-Ben, V. Ntziachristos and D. Razansky, 'Statistical optoacoustic image reconstruction using a-priori knowledge on the location of acoustic distortions', *Applied Physics Letters* **98** (2011), 171110.

[125] J. Jose, R. G. Willemink, S. Resink, D. Piras, J. Van Hespen, C. H. Slump, W. Steenbergen, T. G. van Leeuwen and S. Manohar, 'Passive element enriched photoacoustic computed tomography (PER PACT) for simultaneous imaging of acoustic propagation properties and light absorption', *Optics express* **19** (2011), 2093–2104.

[126] R. G. Willemink, S. Manohar, Y. Purwar, C. H. Slump, F. van der Heijden and T. G. van Leeuwen, 'Imaging of acoustic attenuation and speed of sound maps using photoacoustic measurements', *Medical imaging*, International Society for Optics and Photonics, 2008, pp. 692013–692013.

[127] F. Kiessling and B. J. Pichler, *Small animal imaging*, Springer, 2011.

[128] D. H. Turnbull and S. Mori, 'MRI in mouse developmental biology', *NMR in Biomedicine* **20** (2007), 265–274.

[129] D. Cavanaugh, E. Johnson, R. E. Price, J. Kurie, E. L. Travis and D. D. Cody, 'In vivo respiratory-gated micro-CT imaging in small-animal oncology models', *Molecular imaging* **3** (2004), 55–62.

[130] H. R. Herschman, 'Micro-PET imaging and small animal models of disease', *Current opinion in immunology* **15** (2003), 378–384.

[131] L. Xiang, B. Wang, L. Ji and H. Jiang, '4-D photoacoustic tomography', *Scientific reports* **3** (2013) .

[132] G. Wurzinger, R. Nuster, N. Schmitner, S. Gratt, D. Meyer and G. Paltauf, 'Simultaneous three-dimensional photoacoustic and laser-ultrasound tomography', *Biomedical optics express* **4** (2013), 1380–1389.

[133] G. Diebold and P. Westervelt, 'The photoacoustic effect generated by a spherical droplet in a fluid', *The Journal of the Acoustical Society of America* **84** (1988), 2245–2251.

[134] P. J. Westervelt and R. S. Larson, 'Laser-excited broadside array', *The Journal of the Acoustical Society of America* **54** (1973), 121–122.

[135] G. B. Arfken and H. J. Weber, *Mathematical Methods For Physicists International Student Edition*, Academic press, 2005.

[136] A. Rosenthal, V. Ntziachristos and D. Razansky, 'Acoustic inversion in optoacoustic tomography: A review', *Current medical imaging reviews* **9** (2013), 318.

[137] P. Burgholzer, G. J. Matt, M. Haltmeier and G. Paltauf, 'Exact and approximative imaging methods for photoacoustic tomography using an arbitrary detection surface', *Physical Review E* **75** (2007), 046706.

[138] M. Xu and L. V. Wang, 'Analytic explanation of spatial resolution related to bandwidth and detector aperture size in thermoacoustic or photoacoustic reconstruction', *Physical Review E* **67** (2003), 056605.

[139] M. Haltmeier and G. Zangerl, 'Spatial resolution in photoacoustic tomography: effects of detector size and detector bandwidth', *Inverse Problems* **26** (2010), 125002.

[140] Y. Han, V. Ntziachristos and A. Rosenthal, 'A system analysis and image reconstruction tool for optoacoustic imaging with finite-aperture detectors', *European Conferences on Biomedical Optics*, International Society for Optics and Photonics, 2015, pp. 953915–953915.

[141] D. Queirós, X. L. Déan-Ben, A. Buehler, D. Razansky, A. Rosenthal and V. Ntziachristos, 'Modeling the shape of cylindrically focused transducers in three-dimensional optoacoustic tomography', *Journal of biomedical optics* **18** (2013), 076014–076014.

[142] M.-L. Li, Y.-C. Tseng and C.-C. Cheng, 'Model-based correction of finite aperture effect in photoacoustic tomography', *Optics express* **18** (2010), 26285–26292.

[143] Y. Xu, L. V. Wang, G. Ambartsoumian and P. Kuchment, 'Reconstructions in limited-view thermoacoustic tomography', *Medical physics* **31** (2004), 724–733.

[144] G. Paltauf, R. Nuster, M. Haltmeier and P. Burgholzer, 'Experimental evaluation of reconstruction algorithms for limited view photoacoustic tomography with line detectors', *Inverse Problems* **23** (2007), S81.

[145] M. A. Anastasio, K. Wang, J. Zhang, G. A. Kruger, D. Reinecke and R. A. Kruger, 'Improving limited-view reconstruction in photoacoustic tomography by incorporating a priori boundary information', *Biomedical Optics (BiOS) 2008*, International Society for Optics and Photonics, 2008, 68561B–68561B.

[146] X. L. Dean-Ben, A. Buehler, V. Ntziachristos and D. Razansky, 'Accurate model-based reconstruction algorithm for three-dimensional optoacoustic tomography', *Medical Imaging, IEEE Transactions on* **31** (2012), 1922–1928.

[147] Y. Han, S. Tzoumas, A. Nunes, V. Ntziachristos and A. Rosenthal, 'Sparsity-based acoustic inversion in cross-sectional multiscale optoacoustic imaging', *Medical physics* **42** (2015), 5444–5452.

[148] S. Osher, M. Burger, D. Goldfarb, J. Xu and W. Yin, 'An iterative regularization method for total variation-based image restoration', *Multiscale Modeling & Simulation* **4** (2005), 460–489.

[149] P. Mohajerani, S. Kellnberger and V. Ntziachristos, 'Frequency domain optoacoustic tomography using amplitude and phase', *Photoacoustics* **2** (2014), 111–118.

[150] L. Ding, X. L. Deán-Ben, C. Lutzweiler, D. Razansky and V. Ntziachristos, 'Efficient non-negative constrained model-based inversion in optoacoustic tomography', *Physics in medicine and biology* **60** (2015), 6733.

[151] S. Bu, Z. Liu, T. Shiina, K. Kondo, M. Yamakawa, K. Fukutani, Y. Someda and Y. Asao, 'Model-based reconstruction integrated with fluence compensation for photoacoustic tomography', *Biomedical Engineering, IEEE Transactions on* **59** (2012), 1354–1363.

[152] J. Laufer, B. Cox, E. Zhang and P. Beard, 'Quantitative determination of chromophore concentrations from 2D photoacoustic images using a nonlinear model-based inversion scheme', *Applied optics* **49** (2010), 1219–1233.

[153] Z. Yuan and H. Jiang, 'Quantitative photoacoustic tomography: Recovery of optical absorption coefficient maps of heterogeneous media', *Applied physics letters* **88** (2006), 231101.

[154] J. Glatz, N. C. Deliolanis, A. Buehler, D. Razansky and V. Ntziachristos, 'Blind source unmixing in multi-spectral optoacoustic tomography', *Optics Express* **19** (2011), 3175–3184.

[155] X. L. Deán-Ben, N. C. Deliolanis, V. Ntziachristos and D. Razansky, 'Fast unmixing of multispectral optoacoustic data with vertex component analysis', *Optics and Lasers in Engineering* **58** (2014), 119–125.

[156] T. F. Fehm, X. L. Deán-Ben and D. Razansky, 'Four dimensional hybrid ultrasound and optoacoustic imaging via passive element optical excitation in a hand-held probe', *Applied Physics Letters* **105** (2014), 173505.

[157] T. F. Fehm, X. L. Deán-Ben, S. J. Ford and D. Razansky, 'In vivo whole-body optoacoustic scanner with real-time volumetric imaging capacity', *Optica* **3** (2016), 1153–1159.

[158] P. W. Callen, *Ultrasonography in obstetrics and gynecology*, Elsevier Health Sciences, 2011.

[159] E. I. Bluth, *Ultrasonography in vascular diseases: a practical approach to clinical problems*, Thieme, 2008.

[160] M. A. Hayat, *Methods of Cancer Diagnosis, Therapy and Prognosis*, Springer, 2008.

[161] G. Schmidt, 'Differential Diagnosis Ultrasound-A teaching atlas', (2006).

[162] J. Jose, R. G. Willemink, W. Steenbergen, C. H. Slump, T. G. van Leeuwen and S. Manohar, 'Speed-of-sound compensated photoacoustic tomography for accurate imaging', *Medical physics* **39** (2012), 7262–7271.

[163] C. Kim, T. N. Erpelding, L. Jankovic, M. D. Pashley and L. V. Wang, 'Deeply penetrating in vivo photoacoustic imaging using a clinical ultrasound array system', *Biomedical optics express* **1** (2010), 278–284.

[164] X. L. Deán-Ben, V. Ntziachristos and D. Razansky, 'Artefact reduction in optoacoustic tomographic imaging by estimating the distribution of acoustic scatterers', *Journal of biomedical optics* **17** (2012), 110504–110504.

[165] M. Khan and G. Diebold, 'The photoacoustic effect generated by an isotropic solid sphere', *Ultrasonics* **33** (1995), 265–269.

[166] P. Uslenghi, T. B. Senior, J. Bowman and J. Asvestas, *Electromagnetic and Acoustic Scattering by Simple Shapes. Ed. by JJ Bowman, TBA Senior (and) PLE Uslenghi. Authors-JS Asvestas (et Al.)*. North-Holland, 1969.

[167] K. E. Thomenius, 'Evolution of ultrasound beamformers', *Ultrasonics Symposium, 1996. Proceedings., 1996 IEEE*, vol. 2, IEEE, 1996, pp. 1615–1622.

[168] K. K. Shung and G. A. Thieme, *Ultrasonic scattering in biological tissues*, CRC Press, 1992.

[169] R. Ma, M. Distel, X. L. Deán-Ben, V. Ntziachristos and D. Razansky, 'Non-invasive whole-body imaging of adult zebrafish with optoacoustic tomography', *Physics in Medicine and Biology* **57** (2012), 7227.

[170] A. Buehler, E. Herzog, D. Razansky and V. Ntziachristos, 'Video rate optoacoustic tomography of mouse kidney perfusion', *Optics letters* **35** (2010), 2475–2477.

[171] J. Gamelin, A. Maurudis, A. Aguirre, F. Huang, P. Guo, L. V. Wang and Q. Zhu, 'A real-time photoacoustic tomography system for small animals', *Optics express* **17** (2009), 10489–10498.

[172] J. Turner, H. Estrada, M. Kneipp and D. Razansky, 'Improved optoacoustic microscopy through three-dimensional spatial impulse response synthetic aperture focusing technique', *Optics letters* **39** (2014), 3390–3393.

[173] A. Buehler, X. L. Dean-Ben, D. Razansky and V. Ntziachristos, 'Volumetric optoacoustic imaging with multi-bandwidth deconvolution', *Medical Imaging, IEEE Transactions on* **33** (2014), 814–821.

[174] X. L. Deán-Ben, S. J. Ford and D. Razansky, 'High-frame rate four dimensional optoacoustic tomography enables visualization of cardiovascular dynamics and mouse heart perfusion', *Scientific reports* **5** (2015) .

[175] X. L. Deán-Ben, R. Ma, A. Rosenthal, V. Ntziachristos and D. Razansky, 'Weighted model-based optoacoustic reconstruction in acoustic scattering media', *Physics in medicine and biology* **58** (2013), 5555.

[176] T. F. Fehm, X. L. Deán-Ben, P. Schaur, R. Sroka and D. Razansky, 'Volumetric optoacoustic imaging feedback during endovenous laser therapy–an ex vivo investigation', *Journal of biophotonics* (2015) .

[177] X. L. Deán-Ben, T. F. Fehm, S. J. Ford, S. Gottschalk and D. Razansky, 'Spiral volumetric optoacoustic tomography visualizes multi-scale dynamics in mice', *TBD* (2016) .

[178] J. Hainfeld, D. Slatkin, T. Focella and H. Smilowitz, 'Gold nanoparticles: a new X-ray contrast agent', *The British journal of radiology* (2014) .

[179] P. Caravan, J. J. Ellison, T. J. McMurry and R. B. Lauffer, 'Gadolinium (III) chelates as MRI contrast agents: structure, dynamics, and applications', *Chemical reviews* **99** (1999), 2293–2352.

[180] E. Stride and N. Saffari, 'Microbubble ultrasound contrast agents: a review', *Proceedings of the Institution of Mechanical Engineers, Part H: Journal of Engineering in Medicine* **217** (2003), 429–447.

[181] J. D. Dove, T. W. Murray and M. A. Borden, 'Enhanced photoacoustic response with plasmonic nanoparticle-templated microbubbles', *Soft Matter* **9** (2013), 7743–7750.

[182] J. M. Warram, A. G. Sorace, R. Saini, H. R. Umphrey, K. R. Zinn and K. Hoyt, 'A triple-targeted ultrasound contrast agent provides improved localization to tumor vasculature', *Journal of Ultrasound in Medicine* **30** (2011), 921–931.

[183] M. Jeon, W. Song, E. Huynh, J. Kim, J. Kim, B. L. Helfield, B. Y. Leung, D. E. Goertz, G. Zheng, J. Oh et al., 'Methylene blue microbubbles as a model dual-modality contrast agent for ultrasound and activatable photoacoustic imaging', *Journal of biomedical optics* **19** (2014), 016005–016005.

[184] C. Bone, 'Varicies endoluminal treatment of the laser diode, preliminary study', *Rev Patol Vasc* **5** (1999), 35–46.

[185] L. Navarro, R. J. Min and C. Bone, 'Endovenous laser: a new minimally invasive method of treatment for varicose veins—preliminary observations using an 810 nm diode laser', *Dermatologic surgery* **27** (2001), 117–122.

[186] R. Van den Bos, M. Kockaert, H. Neumann and T. Nijsten, 'Technical review of endovenous laser therapy for varicose veins', *European Journal of Vascular and Endovascular Surgery* **35** (2008), 88–95.

[187] S. Doganci and U. Demirkilic, 'Comparison of 980 nm laser and bare-tip fibre with 1470 nm laser and radial fibre in the treatment of great saphenous vein varicosities: a prospective randomised clinical trial', *European Journal of Vascular and Endovascular Surgery* **40** (2010), 254–259.

[188] M. Vuylsteke, S. Thomis, P. Mahieu, S. Mordon and I. Fourneau, 'Endovenous laser ablation of the great saphenous vein using a bare fibre versus a tulip fibre: a randomised clinical trial', *European journal of vascular and endovascular surgery* **44** (2012), 587–592.

[189] T. M. Proebstle, F. Krummenauer, D. Gül and J. Knop, 'Nonocclusion and early reopening of the great saphenous vein after endovenous laser treatment is fluence dependent', *Dermatologic surgery* **30** (2004), 174–178.

[190] P. E. Timperman, M. Sichlau and R. K. Ryu, 'Greater energy delivery improves treatment success of endovenous laser treatment of incompetent saphenous veins', *Journal of Vascular and Interventional Radiology* **15** (2004), 1061–1063.

[191] T. M. Proebstle, T. Moehler and S. Herdemann, 'Reduced recanalization rates of the great saphenous vein after endovenous laser treatment with increased energy dosing: definition of a threshold for the endovenous fluence equivalent', *Journal of vascular surgery* **44** (2006), 834–839.

[192] H. S. Kim, I. J. Nwankwo, K. Hong and P. S. McElgunn, 'Lower energy endovenous laser ablation of the great saphenous vein with 980 nm diode laser in continuous mode', *Cardiovascular and interventional radiology* **29** (2006), 64–69.

[193] C.-J. Chang and J.-J. Chua, 'Endovenous laser photocoagulation (EVLP) for varicose veins', *Lasers in surgery and medicine* **31** (2002), 257–262.

[194] C.-G. Schmedt, R. Sroka, S. Steckmeier, O. Meissner, G. Babaryka, K. Hunger, V. Ruppert, M. Sadeghi-Azandaryani and B. Steckmeier, 'Investigation on radiofrequency and laser (980nm) effects after endoluminal treatment of saphenous vein insufficiency in an ex-vivo model', *European journal of vascular and endovascular surgery* **32** (2006), 318–325.

[195] T. M. Proebstle, T. Moehler, D. Gül and S. Herdemann, 'Endovenous treatment of the great saphenous vein using a 1,320 nm Nd: YAG laser causes fewer side effects than using a 940 nm diode laser', *Dermatologic Surgery* **31** (2005), 1678–1684.

[196] X. Jia, G. Mowatt, J. Burr, K. Cassar, J. Cook and C. Fraser, 'Systematic review of foam sclerotherapy for varicose veins', *British journal of surgery* **94** (2007), 925–936.

[197] L. S. Kabnick, 'Outcome of different endovenous laser wavelengths for great saphenous vein ablation', *Journal of vascular surgery* **43** (2006), 88–88.

[198] M. Pramanik and L. V. Wang, 'Thermoacoustic and photoacoustic sensing of temperature', *Journal of biomedical optics* **14** (2009), 054024–054024.

[199] E. Petrova, S. Ermilov, R. Su, V. Nadvoretskiy, A. Conjusteau and A. Oraevsky, 'Using optoacoustic imaging for measuring the temperature dependence of Grüneisen parameter in optically absorbing solutions', *Optics express* **21** (2013), 25077–25090.

[200] R. Sroka, C.-G. Schmedt, S. Steckmeier, O. A. Meissner, W. Beyer, G. Babaryka and B. Steckmeier, 'Ex-vivo investigation of endoluminal vein treatment by means of radiofrequency and laser irradiation', *Medical Laser Application* **21** (2006), 15–22.

[201] A. Buehler, A. Rosenthal, T. Jetzfellner, A. Dima, D. Razansky and V. Ntziachristos, 'Model-based optoacoustic inversions with incomplete projection data', *Medical physics* **38** (2011), 1694–1704.

[202] T. J. Beck, C. Burgmeier, R. Blagova, B. Steckmeier, V. Hecht, C.-G. Schmedt and R. Sroka, 'Thermal-induced effects on vein tissue–A basic ex-vivo investigation for EVLT', *Medical laser application* **22** (2008), 238–241.

[203] N. P. Blockley, V. E. Griffeth, A. B. Simon and R. B. Buxton, 'A review of calibrated blood oxygenation level-dependent (BOLD) methods for the measurement of task-induced changes in brain oxygen metabolism', *NMR in Biomedicine* **26** (2013), 987–1003.

[204] R. B. Buxton, 'Interpreting oxygenation-based neuroimaging signals: the importance and the challenge of understanding brain oxygen metabolism', *Front Neuroenergetics* **2** (2010) .

[205] A. Devor, S. Sakadžić, V. J. Srinivasan, M. A. Yaseen, K. Nizar, P. A. Saisan, P. Tian, A. M. Dale, S. A. Vinogradov, M. A. Franceschini et al., 'Frontiers in optical imaging of cerebral blood flow and metabolism', *Journal of Cerebral Blood Flow & Metabolism* **32** (2012), 1259–1276.

[206] Z. B. Rodgers, V. Jain, E. K. Englund, M. C. Langham and F. W. Wehrli, 'High temporal resolution MRI quantification of global cerebral metabolic rate of oxygen consumption in response to apneic challenge', *Journal of Cerebral Blood Flow & Metabolism* **33** (2013), 1514–1522.

[207] L.-D. Liao, C.-T. Lin, Y.-Y. I. Shih, T. Q. Duong, H.-Y. Lai, P.-H. Wang, R. Wu, S. Tsang, J.-Y. Chang, M.-L. Li et al., 'Transcranial imaging of functional cerebral hemodynamic changes in single blood vessels using in vivo photoacoustic microscopy', *Journal of Cerebral Blood Flow & Metabolism* **32** (2012), 938–951.

[208] J. Laufer, E. Zhang, G. Raivich and P. Beard, 'Three-dimensional noninvasive imaging of the vasculature in the mouse brain using a high resolution photoacoustic scanner', *Applied optics* **48** (2009), D299–D306.

[209] D. Bulte, P. Chiarelli, R. Wise and P. Jezzard, 'Measurement of cerebral blood volume in humans using hyperoxic MRI contrast', *Journal of Magnetic Resonance Imaging* **26** (2007), 894–899.

[210] E. M. Hillman, A. Devor, M. B. Bouchard, A. K. Dunn, G. Krauss, J. Skoch, B. J. Bacskai, A. M. Dale and D. A. Boas, 'Depth-resolved optical imaging and microscopy of vascular compartment dynamics during somatosensory stimulation', *Neuroimage* **35** (2007), 89–104.

[211] M. Avoli, 'A brief history on the oscillating roles of thalamus and cortex in absence seizures', *Epilepsia* **53** (2012), 779–789.

[212] D. N. Lenkov, A. B. Volnova, A. R. Pope and V. Tsytsarev, 'Advantages and limitations of brain imaging methods in the research of absence epilepsy in humans and animal models', *Journal of neuroscience methods* **212** (2013), 195–202.

[213] Z. L. Yang and L. J. Zhang, 'PET/MRI of central nervous system: current status and future perspective', *European radiology* (2016), 1–8.

[214] H. Yang, T. Zhang, J. Zhou, P. R. Carney and H. Jiang, 'In vivo imaging of epileptic foci in rats using a miniature probe integrating diffuse optical tomography and electroencephalographic source localization', *Epilepsia* **56** (2015), 94–100.

[215] V. Tsytsarev, C. Bernardelli and K. I. Maslov, 'Living brain optical imaging: technology, methods and applications', *Journal of Neuroscience and Neuroengineering* **1** (2012), 180–192.

[216] Q. Tang, V. Tsytsarev, C.-P. Liang, F. Akkentli, R. S. Erzurumlu and Y. Chen, 'In Vivo Voltage-Sensitive Dye Imaging of Subcortical Brain Function', *Scientific reports* **5** (2015) .

[217] V. Tsytsarev, B. Rao, K. I. Maslov, L. Li and L. V. Wang, 'Photoacoustic and optical coherence tomography of epilepsy with high temporal and spatial resolution and dual optical contrasts', *Journal of neuroscience methods* **216** (2013), 142–145.

[218] J. Tang, L. Xi, J. Zhou, H. Huang, T. Zhang, P. R. Carney and H. Jiang, 'Noninvasive high-speed photoacoustic tomography of cerebral hemodynamics in awake-moving rats', *Journal of Cerebral Blood Flow & Metabolism* **35** (2015), 1224–1232.

[219] S. Bahar, M. Suh, M. Zhao and T. H. Schwartz, 'Intrinsic optical signal imaging of neocortical seizures: the 'epileptic dip'', *Neuroreport* **17** (2006), 499–503.

[220] M. Zhao, H. Ma, M. Suh and T. H. Schwartz, 'Spatiotemporal dynamics of perfusion and oximetry during ictal discharges in the rat neocortex', *The Journal of Neuroscience* **29** (2009), 2814–2823.

[221] J. D. Van Horn, S. T. Grafton, D. Rockmore and M. S. Gazzaniga, 'Sharing neuroimaging studies of human cognition', *Nature neuroscience* **7** (2004), 473–481.

[222] A. Dorr, J. Sled and N. Kabani, 'Three-dimensional cerebral vasculature of the CBA mouse brain: a magnetic resonance imaging and micro computed tomography study', *Neuroimage* **35** (2007), 1409–1423.

[223] G. Paxinos and K. B. Franklin, *The mouse brain in stereotaxic coordinates*, Gulf Professional Publishing, 2004.

[224] A. Dorr, J. P. Lerch, S. Spring, N. Kabani and R. M. Henkelman, 'High resolution three-dimensional brain atlas using an average magnetic resonance image of 40 adult C57Bl/6J mice', *Neuroimage* **42** (2008), 60–69.

[225] R. B. Buxton, 'Dynamic models of BOLD contrast', *Neuroimage* **62** (2012), 953–961.

[226] M. Mancini, A. Greco, E. Tedeschi, G. Palma, M. Ragucci, M. G. Bruzzone, A. R. D. Coda, E. Torino, A. Scotti, I. Zucca et al., 'Head and Neck Veins of the Mouse. A Magnetic Resonance, Micro Computed Tomography and High Frequency Color Doppler Ultrasound Study', *PloS one* **10** (2015), e0129912.

[227] F. B. Neubauer, A. Sederberg and J. N. MacLean, 'Local changes in neocortical circuit dynamics coincide with the spread of seizures to thalamus in a model of epilepsy', *Frontiers in neural circuits* **8** (2014), 101.

[228] M. Minlebaev, M. Colonnese, T. Tsintsadze, A. Sirota and R. Khazipov, 'Early gamma oscillations synchronize developing thalamus and cortex', *Science* **334** (2011), 226–229.

[229] P. S. Pearce, D. Friedman, J. J. LaFrancois, S. S. Iyengar, A. A. Fenton, N. J. MacLusky and H. E. Scharfman, 'Spike–wave discharges in adult Sprague–Dawley rats and their implications for animal models of temporal lobe epilepsy', *Epilepsy & Behavior* **32** (2014), 121–131.

[230] M. Zhao, J. Nguyen, H. Ma, N. Nishimura, C. B. Schaffer and T. H. Schwartz, 'Preictal and ictal neurovascular and metabolic coupling surrounding a seizure focus', *The Journal of Neuroscience* **31** (2011), 13292–13300.

[231] R. Weissleder and M. Nahrendorf, 'Advancing biomedical imaging', *Proceedings of the National Academy of Sciences* **112** (2015), 14424–14428.

[232] X. Yu, C. Qian, D.-y. Chen, S. J. Dodd and A. P. Koretsky, 'Deciphering laminar-specific neural inputs with line-scanning fMRI', *Nature methods* **11** (2014), 55–58.

[233] A. Ale, V. Ermolayev, E. Herzog, C. Cohrs, M. H. de Angelis and V. Ntziachristos, 'FMT-XCT: in vivo animal studies with hybrid fluorescence molecular tomography-X-ray computed tomography', *Nature methods* **9** (2012), 615–620.

[234] W. Wein, S. Brunke, A. Khamene, M. R. Callstrom and N. Navab, 'Automatic CT-ultrasound registration for diagnostic imaging and image-guided intervention', *Medical image analysis* **12** (2008), 577–585.

[235] Y. Hu, H. U. Ahmed, Z. Taylor, C. Allen, M. Emberton, D. Hawkes and D. Barratt, 'MR to ultrasound registration for image-guided prostate interventions', *Medical image analysis* **16** (2012), 687–703.

[236] S. R. Cherry, 'Multimodality in vivo imaging systems: twice the power or double the trouble?', *Annu. Rev. Biomed. Eng.* **8** (2006), 35–62.

[237] J. Yao, A. A. Kaberniuk, L. Li, D. M. Shcherbakova, R. Zhang, L. Wang, G. Li, V. V. Verkhusha and L. V. Wang, 'Multiscale photoacoustic tomography using reversibly switchable bacterial phytochrome as a near-infrared photochromic probe', *Nature methods* **13** (2016), 67–73.

[238] J. Yao, L. Wang, J.-M. Yang, K. I. Maslov, T. T. Wong, L. Li, C.-H. Huang, J. Zou and L. V. Wang, 'High-speed label-free functional photoacoustic microscopy of mouse brain in action', *Nature methods* **12** (2015), 407–410.

[239] L. Kirscher, X. L. Deán-Ben, M. Scadeng, A. Zaremba, Q. Zhang, C. Kober, T. F. Fehm, D. Razansky, V. Ntziachristos, J. Stritzker et al., 'Doxycycline inducible melanogenic vaccinia virus as theranostic anti-cancer agent', *Theranostics* **5** (2015), 1045.

[240] A. P. Jathoul, J. Laufer, O. Ogunlade, B. Treeby, B. Cox, E. Zhang, P. Johnson, A. R. Pizzey, B. Philip, T. Marafioti et al., 'Deep in vivo photoacoustic imaging of mammalian tissues using a tyrosinase-based genetic reporter', *Nature Photonics* (2015) .

[241] J. Li, F. Cheng, H. Huang, L. Li and J.-J. Zhu, 'Nanomaterial-based activatable imaging probes: from design to biological applications', *Chemical Society Reviews* **44** (2015), 7855–7880.

[242] N. C. Deliolanis, A. Ale, S. Morscher, N. C. Burton, K. Schaefer, K. Radrich, D. Razansky and V. Ntziachristos, 'Deep-tissue reporter-gene imaging with fluorescence and optoacoustic tomography: a performance overview', *Molecular Imaging and Biology* **16** (2014), 652–660.

[243] S. Gottschalk, H. Estrada, O. Degtyaruk, J. Rebling, O. Klymenko, M. Rosemann and D. Razansky, 'Short and long-term phototoxicity in cells expressing genetic reporters under nanosecond laser exposure', *Biomaterials* **69** (2015), 38–44.

[244] L. E. Gerlowski and R. K. Jain, 'Physiologically based pharmacokinetic modeling: principles and applications', *Journal of pharmaceutical sciences* **72** (1983), 1103–1127.

[245] S. G. Sakka, 'Assessing liver function', *Current opinion in critical care* **13** (2007), 207–214.

[246] C. M. Kramer, A. J. Sinusas, D. E. Sosnovik, B. A. French and F. M. Bengel, 'Multimodality imaging of myocardial injury and remodeling', *Journal of Nuclear Medicine* **51** (2010), 107S–121S.

[247] N. Bertrand, J. Wu, X. Xu, N. Kamaly and O. C. Farokhzad, 'Cancer nanotechnology: the impact of passive and active targeting in the era of modern cancer biology', *Advanced drug delivery reviews* **66** (2014), 2–25.

Glossary

4-AP 4-Aminopyridine. 54, 55, 57–61, 77

ACSF Artificial Cerebrospinal Fluid. 55, 58

AF750 Alexa Fluor 750. 38, 64, 67, 68, 70, 75, 94

BOLD Blood-Oxygen-Level Dependent. 49

CBF Cerebral Blood Flow. 49

CBV Cerebral Blood Volume. 49, 51, 72

cl contralateral. 57, 58, 60, 77

CS Confluence of Sinuses. 50, 57, 60, 77

CT X-Ray Tomography. 37, 49, 63, 65

DAQ Data Acquisition System. 23, 29

EEG Electroencephalogram. 53–55, 57, 58, 60, 76–78

EFE Endovenous Fluence Equivalent. 41

ELT Endovenous Laser Therapy. 14, 41–47, 72, 73

FL Frontal Lobe. 58, 60, 61, 77, 78

FWHM Full-Width at Half Maximum. 23, 25, 26, 28, 29, 33

GPU Graphical Processing Unit. 8, 23, 32, 44, 71

HbO Oxygenized Hemoglobin. 10, 11, 49–52, 56–60, 72, 77, 78

HbR Deoxygenized Hemoglobin. 10, 11, 49–52, 56–60, 72, 77, 78

HbT Total Hemoglobin. 49–51, 57, 59, 60, 72, 77

ICG Indocyanine green. 6, 10, 64–67, 75, 76

LEED Linear Endovenous Energy Density. 41, 42

LHV Longitudinal Hippocampal Vein. 50–52, 57, 60, 77

MIP Maximum Intensity Projection. 25, 31–35, 39, 44–47, 50, 57, 60, 61, 64–68, 70, 77, 78, 93

MRI Magnetic Resonance Imaging. 37, 49, 51, 53, 55, 57, 63, 65, 68

MS Multispectral. 5, 9–11, 13, 14, 19, 22, 49–51, 54, 55, 59, 64, 71–73, 93

MSOT Multispectral Optoacoustic Tomography. 10

OA optoacoustic. 3–24, 26–29, 32, 35, 37–47, 49–51, 53–59, 61, 63–68, 70–73, 75, 76, 93

OE Optoacoustic Endoscopy. 6, 7, 71

OHRF Optoacoustic Hemodynamic Response Function. 56, 57, 61, 76, 94

OM Optoacoustic Microscopy. 6, 7, 71

OT Optoacoustic Tomography. 6–9, 11–14, 28, 34, 35, 71, 93

PBS Phosphate-buffered Saline. 64

PC Parietal-Temporal Cortex. 58, 60, 61, 77, 78

PE Passive Element. 22–25, 27

PET Positron Emission Tomography. 49

PRF Pulse Repetition Frequency. 9, 22, 24, 27, 28, 31, 35, 38, 43, 51, 64

RRV Rostral Rhinal Vein. 50

SMTA Spherical Matrix Transducer Array. 9, 10, 12–14, 17, 22–25, 27–32, 34, 38, 43, 45, 47, 49–52, 54, 55, 93

sO_2 Blood Oxygenation. 49, 51–53, 72

SSS Superior Sagittal Sinus. 50–52, 55, 57, 58, 60, 77

SWD Spike–Wave Discharges. 53

TA Thalamus. 58, 60, 61, 77, 78

TS Transverse Sinus. 50, 57

US Ultrasound. 8, 12, 13, 21–28, 35, 37, 39–44, 46, 49, 63, 68, 71, 72, 93

VOI Voxel of Interest. 50–52

VOT Volumetric Optoacoustic Tomography. 9–12

List of Figures

Acknowledgment

This thesis would have not been possible without the academic, financial and emotional support of countless people and I would like to take this chance to thank them for everything they have done for me.

Foremost, I would like to express my deepest gratitude to my doctoral advisor, Prof. Dr. Daniel Razansky, for his academic guidance, his absolute support, his patience and his generosity throughout the past years.

I also would like to deeply thank Dr. Xosé Luis Deán Ben for his dedication and his inexhaustible patience in supporting my doctoral studies with his time and knowledge.

Many thanks go to all the people at the Institute of Biological and Medical Imaging of the Helmholtz Center Munich who made the past years a memorable experience.

In particular, I would like to express my appreciation to the Deutsche Telekom Stiftung for their generous scholarship and the support it has offered me during my doctoral studies. Specifically, I would like to thank Ms. Frense-Heck and Ms. Timm for their kind and supporting attitude.

Furthermore, I would like to deeply thank Prof. Dr. Claudio Vinegoni for giving me the opportunity to temporarily join his group as a visiting researcher as well as his warm welcome in Boston. It was a great experience that I will never forget.

Last, but not least, I want to express my deepest gratitude to my friends and my family - I am endlessly thankful for everything you did for me.